

Ancient Martian aeolian processes and palaeomorphology reconstructed from the Stimson formation on the lower slope of Aeolis Mons, Gale crater, Mars

STEVEN G. BANHAM* , SANJEEV GUPTA*, DAVID M. RUBIN†, JESSICA A. WATKINS‡, DAWN Y. SUMNER§ , KENNETH S. EDGETT¶ , JOHN P. GROTZINGER‡ , KEVIN W. LEWIS** , LAUREN A. EDGAR†† , KATHRYN M. STACK-MORGAN‡‡, ROBERT BARNES* , JAMES F. BELL III§§ , MACKENZIE D. DAY¶¶ , RYAN C. EWING*** , MATHIEU G.A. LAPOTRE††† , NATHAN T. STEIN‡, FRANCES RIVERA-HERNANDEZ§ and ASHWIN R. VASAVADA‡‡ 

*Department of Earth Science and Engineering, Imperial College, London, SW7 2AZ, UK
(Email: s.banham@imperial.ac.uk)

†Department of Earth and Planetary Sciences, University of California, 1156 High Street, Santa Cruz, CA 95064, USA

‡Division of Geological and Planetary Sciences, California Institute of Technology, 1200 East California Boulevard, Pasadena, CA 91125, USA

§Earth and Planetary Sciences, University of California, Davis, CA 95616, USA

¶Malin Space Science Systems, P.O. Box 910148, San Diego, CA 92191-0148, USA

**Department of Earth and Planetary Sciences, Johns Hopkins University, 301 Olin Hall, 3400 N. Charles Street, Baltimore, MD 21218, USA

††U.S. Geological Survey, Astrogeology Science Center, 2255 N. Gemini Dr., Flagstaff, AZ 86001, USA

‡‡Jet Propulsion Laboratory, California Institute of Technology, 4800 Oak Grove Drive, Pasadena, CA 91109, USA

§§School of Earth and Space Exploration, Arizona State University, Tempe, AZ 85287, USA

¶¶Department of Earth & Space Sciences, University of Washington, Seattle, WA 98195, USA

***Department of Geology and Geophysics, Texas A&M University, College Station, TX 77843, USA

†††Department of Earth and Planetary Sciences, Harvard University, Cambridge, MA 02138, USA

ABSTRACT

Reconstruction of the palaeoenvironmental context of Martian sedimentary rocks is central to studies of ancient Martian habitability and regional palaeoclimate history. This paper reports the analysis of a distinct aeolian deposit preserved in Gale crater, Mars, and evaluates its palaeomorphology, the processes responsible for its deposition, and its implications for Gale crater geological history and regional palaeoclimate. Whilst exploring the sedimentary succession cropping out on the northern flank of Aeolis Mons, Gale crater, the Mars Science Laboratory rover *Curiosity* encountered a decametre-thick sandstone succession, named the Stimson formation, unconformably overlying lacustrine deposits of the Murray formation. The sandstone contains sand grains characterized by high roundness and sphericity, and cross-bedding on the order of 1 m in thickness, separated by sub-horizontal bounding surfaces traceable for tens of metres across outcrops. The cross-beds are composed of uniform thickness cross-laminations interpreted as wind-ripple strata. Cross-sets are separated by sub-horizontal bounding surfaces traceable for tens of metres across outcrops that are interpreted as dune migration surfaces. Grain characteristics and presence of wind-ripple strata indicate deposition of the Stimson formation by aeolian processes. The absence of features characteristic of damp or wet aeolian sediment accumulation indicate deposition in a dry aeolian system. Reconstruction of the palaeogeomorphology suggests that the Stimson dune field was

composed largely of simple sinuous crescentic dunes with a height of *ca* 10 m, and wavelengths of *ca* 150 m, with local development of complex dunes. Analysis of cross-strata dip azimuths indicates that the general dune migration direction and hence net sediment transport was towards the north-east. The juxtaposition of a dry aeolian system unconformably above the lacustrine Murray formation represents starkly contrasting palaeoenvironmental and palaeoclimatic conditions. Stratigraphic relationships indicate that this transition records a significant break in time, with the Stimson formation being deposited after the Murray formation and stratigraphically higher Mount Sharp group rocks had been buried, lithified and subsequently eroded.

Keywords Aeolian, *Curiosity* rover, dune field, Gale crater, Mars, Mars Science Laboratory, remote sensing, Stimson.

INTRODUCTION

One goal associated with most recent robotic missions to the surface of Mars is the exploration for rocks with potential to contain evidence of biosignatures. Central to this endeavour is the robust reconstruction of the palaeoenvironmental context of sedimentary rock strata investigated during rover traverses and identification of those rock successions that best record ancient habitable environments. Although aeolian strata are not considered to be the best geological materials in which to preserve records of ancient habitable environments (Summons *et al.*, 2011), understanding the processes responsible for generating extra-terrestrial aeolian stratigraphy is important for reconstructing the context of Martian sedimentary successions and for determining the regional palaeoclimate history. The current understanding of aeolian stratigraphic records on Earth is relatively advanced, such that analogues derived from Earth provide invaluable templates to reading Martian aeolian archives. Here an ancient aeolian sedimentary rock unit in Gale crater, Mars, is analysed based on observations derived from images acquired by the mobile platform (rover), *Curiosity*, in concert with images obtained by a high spatial resolution (*ca* 30 cm per pixel) orbiting camera system. This paper aims to evaluate how this rock unit places bounds on variations in palaeoenvironmental conditions in Gale crater.

Aeolian sedimentary systems have been documented on many planetary bodies besides Earth within the solar system: Venus (Greeley *et al.*, 1992); Mars (Bourke *et al.*, 2008); Titan (Radebaugh, 2013); Triton (Sagan & Chyba, 1990); Pluto (Telfer *et al.*, 2017); and comet 67P/

Churyumov–Gerasimenko (Jia *et al.*, 2017); however, aeolian strata – the preserved expression of ancient wind-blown sediments – have only been documented on Earth and Mars (Grotzinger *et al.*, 2005; Metz *et al.*, 2009; Hayes *et al.*, 2011; Edgar *et al.*, 2012; Milliken *et al.*, 2014). Present-day Mars has fundamentally different boundary conditions relative to Earth, with lower atmospheric density and gravity. These differences in boundary conditions are manifest in a number of ways, notably in sediment transport mechanics and bedform evolution. Sullivan & Kok (2017) observed that even though the fluid friction threshold speed (u_{*tf}) is much higher on Mars than on Earth, the impact threshold (u_{*ti}) is lower and that mobile grains form saltation clusters, allowing sediment transport with relatively low flux. The low density atmosphere gives rise to an intermediate class of bedform described by Lapotre *et al.* (2016) as ‘wind-drag ripples’ which are not observed on Earth. Additional complexities arise when considering present-day Mars as an analogue for past processes on Mars: Slipski & Jakosky (2016) show that two-thirds of the Martian atmosphere has been lost to space in the last 4.4 Ga, meaning that ancient aeolian processes would probably have occurred under different atmospheric conditions to those of modern processes.

However, despite the differences in boundary conditions and the additional bedforms which arise from this, Ewing *et al.* (2017) argue that the aeolian stratigraphic record is largely controlled by the evolution of bedform patterns, and that pattern evolution is similar on Earth and Mars, potentially suggesting that their stratigraphic records will be similar. Such hypotheses require testing against high-quality outcrop exposures of aeolian stratigraphy. This paper

addresses the following questions: what is the range of aeolian sedimentary structures preserved in Martian sedimentary rocks; what do these structures tell us about aeolian sedimentary processes on Mars; what does the sedimentary architecture of these aeolian rocks tell us about the spatial and temporal evolution of aeolian sedimentary environments and preservation of aeolian geomorphology; did the presence of water play a role in the accumulation of aeolian strata and generation of its sedimentary architecture; and what can the strata reveal about ancient sediment transport pathways?

Since 6 August 2012, the Mars Science Laboratory (MSL) science team has been using the *Curiosity* rover to explore the sedimentary archive preserved in the $ca\ 3.7 \pm 0.1$ Ga crater, 'Gale'. The team has documented a rich array of clastic sedimentary rocks in lower Aeolis Mons (a 5 km high mountain of stratified rock informally called Mount Sharp) and Aeolis Palus (the valley between the north wall of Gale and Aeolis Mons) (Williams *et al.*, 2013; Grotzinger *et al.*, 2014, 2015; Vasavada *et al.*, 2014). The overall aim of the MSL mission is to determine the origin of the accessible layered sedimentary rocks within the crater and the potential for ancient habitable environments. Through detailed sedimentary, stratigraphic and geochemical investigations using the rover's instruments, a robust model for the sedimentary evolution of potentially habitable environments in Gale at a time chrono-correlative with Earth's early Archean has been derived. Field observations enable reconstruction of a first-order stratigraphy for these Martian rocks and interpretation of various facies that range from alluvial fan deposits, cross-bedded fluvial sandstones, deltaic sandstones and lacustrine mudstones (Williams *et al.*, 2013; Grotzinger *et al.*, 2014, 2015; Vasavada *et al.*, 2014; Stack *et al.*, 2016; Edgar *et al.*, 2017; Hurowitz *et al.*, 2017; Rampe *et al.*, 2017; Rice *et al.*, 2017). This sedimentary record indicates a climate with sufficient warmth and humidity to sustain river systems and long-lived lakes in the crater. During the rover's traverse across the lacustrine Murray formation, which has represented a focus of the search for a habitable environment, the rover encountered a stratigraphic unit overlying the Murray formation mudstones. Analysis of rover-derived images indicates that this unit unconformably overlies the Murray formation and was informally designated the Stimson formation by the MSL team. The Stimson

potentially represents one of the younger stratigraphic units preserved in the crater.

The aim of this paper is to reconstruct the sedimentary processes and palaeomorphology of the Stimson depositional system using observations from the suite of cameras onboard *Curiosity*. The specific objectives are to: (i) characterize sedimentary structures, facies and architecture of the Stimson formation; (ii) describe the relationship of the Stimson to the sub-Stimson unconformity; (iii) reconstruct the dune-field morphology and the mechanism of deposition and sediment accumulation; (iv) determine palaeo-sediment transport patterns; and (v) discuss the broader palaeoclimatic significance of aeolian strata preserved in Gale crater. The overarching goal is to use the stratigraphy of the Stimson formation to constrain Martian sedimentary processes and palaeoenvironmental conditions, and to place first-order bounds on the ancient Martian climate at Gale crater.

GEOLOGICAL AND STRATIGRAPHIC CONTEXT

Gale crater

Gale crater is a 155 km diameter impact crater located $ca\ 5^\circ$ south of the Martian equator (5.4°S , 137.8°E) (Fig. 1). Gale occurs on the hemispherical topographic boundary between the cratered southern highlands and the much less-cratered northern lowland plains of Mars, known as the Martian crustal dichotomy. Crater counts suggest that Gale crater formed at $ca\ 3.8$ to 3.6 Ga (Thomson *et al.*, 2011; Le Deit *et al.*, 2013) – a time that is considered to be the transition between the Noachian and Hesperian epochs (Tanaka *et al.*, 2014) – and that the crater-filling strata were deposited over a 200 to 500 Myr period thereafter (Thomson *et al.*, 2011; Grant *et al.*, 2014; Palucis *et al.*, 2014; Grotzinger *et al.*, 2015). The central portion of the crater contains stratified rocks, interpreted to be sedimentary, that form the 5 km high mountain called Aeolis Mons (Malin & Edgett, 2000; Anderson & Bell, 2010; Thomson *et al.*, 2011).

The Stimson formation in its stratigraphic context

During the August 2012 to August 2017 period, the MSL team explored a portion of the

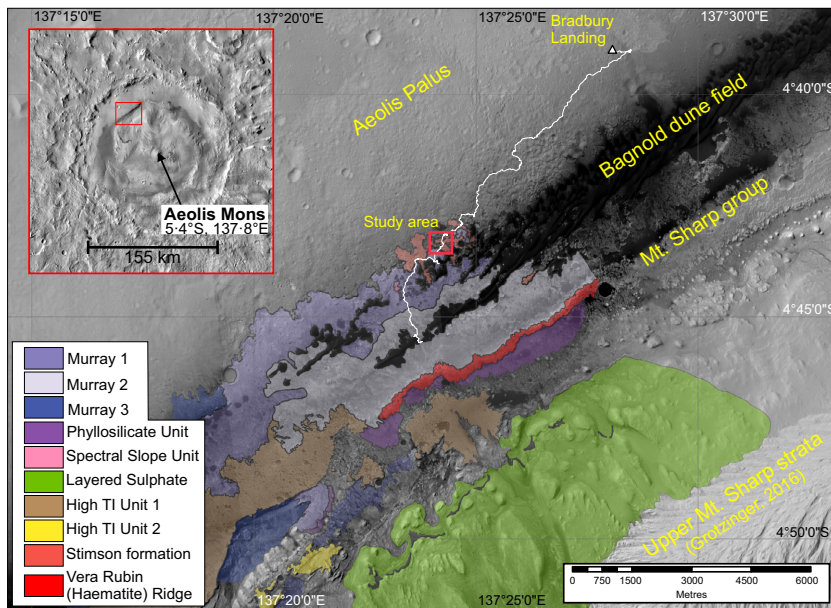


Fig. 1. High Resolution Imaging Science Experiment (HiRISE) satellite mosaic showing the region of the *Curiosity* rover traverse within Gale crater, and the relation of the traverse with major Mount Sharp units mapped from orbit (Fraeman *et al.*, 2016) on the northern flank of Aeolis Mons. The study area is focused on the area of the traverse between Marias Pass (Sol 992) to East Glacier (Sol 1154), where the Stimson formation was first observed. The inset map displays the position of the regional map within the context of Gale crater. Basemap, MSL Gale Merged Orthophoto Mosaic 25 m was generated by Calef & Parker, 2016. Image credit: NASA/JPL/University of Arizona.

lowermost exposed *ca* 300 m of the stratigraphy exposed on the lower north-facing slopes of Aeolis Mons (Fig. 1). The first *ca* 100 m of the succession (Bradbury group and lower Murray formation through to Pahrump Hills outcrop) are interpreted as interfingered fluvial, deltaic and lacustrine sedimentary rocks (conglomerates, sandstones and mudstones) with minor aeolian interbeds (Williams *et al.*, 2013; Grotzinger *et al.*, 2014, 2015; Stack *et al.*, 2016; Edgar *et al.*, 2017; Rice *et al.*, 2017; Schieber *et al.*, 2017). The rocks *ca* 200 m stratigraphically higher which comprise the Murray formation (Mount Sharp group) are predominantly laminated mudstones with minor interfingered sandstones and represent accumulation of lake-bed sediments (Grotzinger *et al.*, 2015). Both the Bradbury group and Murray formation were buried to a substantial depth (hundreds to thousands of metres) and then exhumed by aeolian deflation (Malin & Edgett, 2000; Day *et al.*, 2016). These rocks have been affected by burial diagenesis, including cementation, fracturing and vein mineralization (Frydenvang *et al.*, 2017; Yen *et al.*, 2017).

Mount Sharp group strata are truncated and overlain by a younger stratigraphic unit named the Siccar Point group (Fraeman *et al.*, 2016) which is inferred to have been deposited following an episode of erosion and exposure of the Mount Sharp group strata (Fig. 1). Along *ca* 500 m of the rover traverse described in this paper, the Murray formation strata are

unconformably overlain by the Stimson formation which is placed within the Siccar Point group (Figs 2 and 3). This stratal unit was first identified in orbital images and termed ‘draping strata’ or ‘washboard unit’ by Milliken *et al.* (2014) and Rubin *et al.* (2014). Fraeman *et al.* (2016) note that the Stimson formation is characterized by high thermal inertia in orbital data and link it to several other units higher up on the slope of Aeolis Mons (High Thermal Inertia Units 1 and 2) that appear to stratigraphically truncate Mount Sharp group rocks (Fig. 1). However, a correlation based on ground-based data between the Stimson and these other units characterized by high thermal is currently not possible because *Curiosity* has not traversed these strata.

When viewed in ‘Mastcam’ mosaics, the Stimson formation consists of distinctive metre-scale cross-bedded sandstone, which typically has a blocky grey-colour. The unconformity on which the Stimson formation accumulated has been mapped in detail along the traverse by Watkins *et al.* (2016). These authors show that the unconformity exhibits metre-scale palaeotopography across the area traversed by *Curiosity*. The unconformity dips generally towards the north indicating a northward palaeotopographic slope at the time of Stimson deposition (Fig. 2B).

Here, the sedimentology and stratigraphy of the Stimson formation in the area where the Stimson was first identified, between Logan Pass

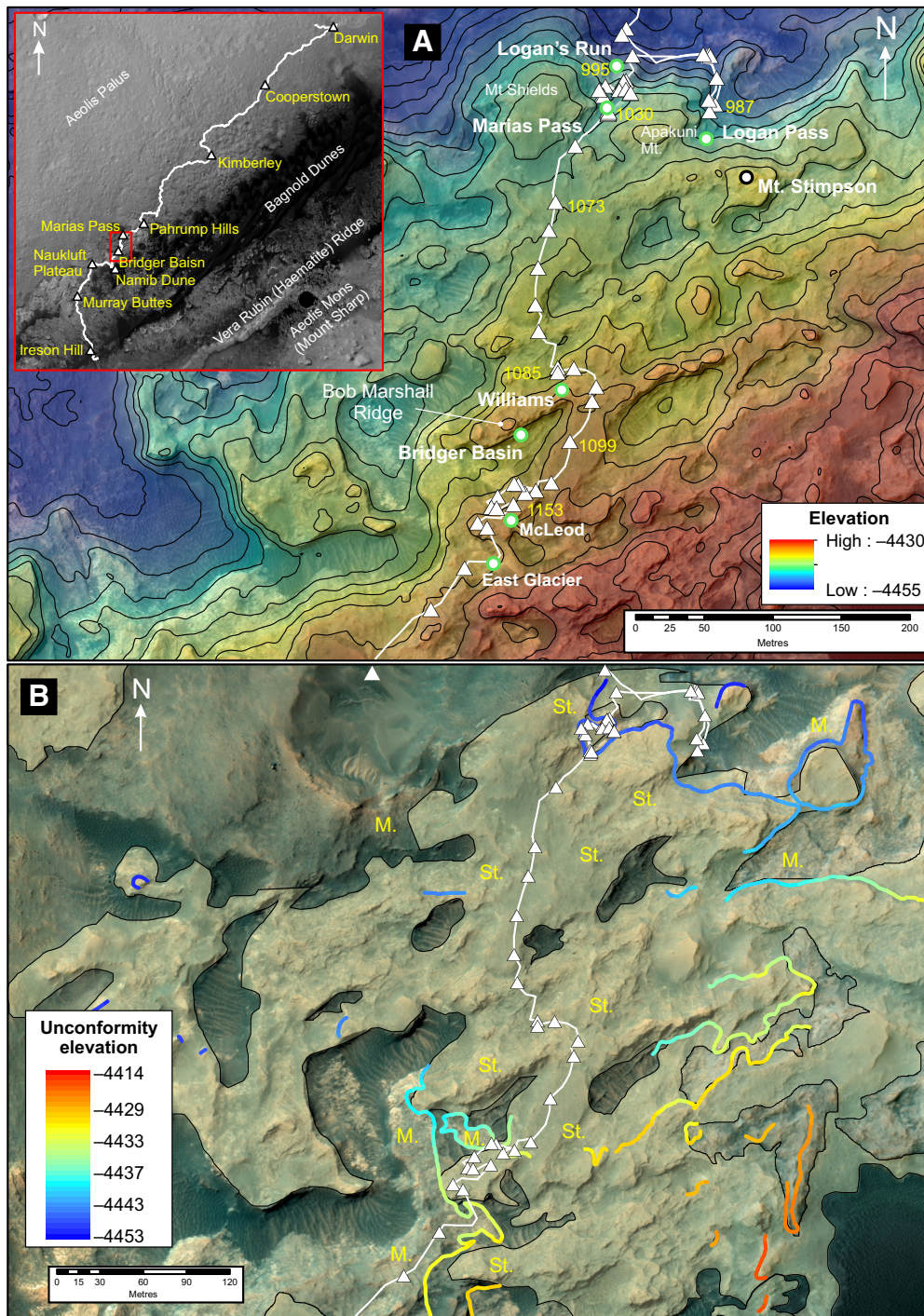


Fig. 2. Detailed maps of the Marias Pass to East Glacier region of the rover traverse depicting key locations and the distribution of Stimson formation outcrops. (A) Digital elevation model (1 m resolution) overlain on a colourized High Resolution Imaging Science Experiment (HiRISE) mosaic, depicting key locations (green circles), and their relationship to the rover traverse and end-of-Sol positions for the rover (white triangles). Note that elevation rises from the north-east towards the south-west, in the direction the rover traversed. Contours (black) represent 2 m increases in vertical elevation. The inset is a context map showing the location of the study area along *Curiosity*'s traverse to Aeolis Mons. (B) Geological map showing outcrop of Stimson formation superimposed on a colourized HiRISE mosaic (from Calef & Parker, 2016). Coloured line indicates sub-Stimson unconformity, which is coloured by elevation (Watkins *et al.*, 2016). The elevation of the unconformity increases to the south-east onto the flank of Aeolis Mons. Image credits: NASA/JPL/University of Arizona.

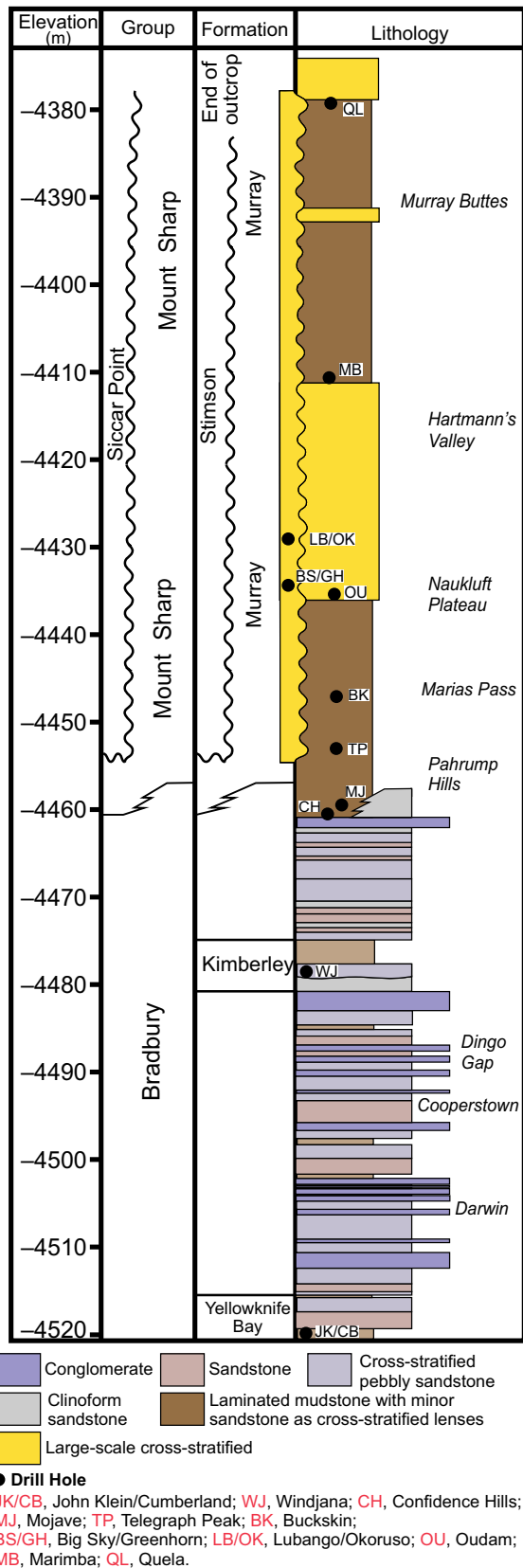


Fig. 3. Stratigraphic context of the Stimson formation. Stratigraphic column depicts key units encountered by the rover during the mission. The column shows units associated with the vertical elevation at which they were observed along the traverse and does not account for total stratigraphic thickness. The Stimson formation was the first observed unit within the Siccar Point group and unconformably overlies the Murray formation of the Mount Sharp group. For this study, the Stimson formation was studied between elevation -4455 m and -4437 m.

and the East Glacier location, is described and interpreted (Fig. 2A). The MSL team investigated these sites using the *Curiosity* rover between Sols 987 and 1055. The study area encompasses an elevation gain from -4455 m at Logan's Run to -4432 m at East Glacier.

DATA AND METHODS

For this study, images of Martian sedimentary rock outcrops were collected using three separate instrument suites on the MSL rover *Curiosity*, the Mast Cameras (Mastcams), Mars Hand Lens Imager (MAHLI) and Navigation cameras (Navcams). In addition, satellite images (with resolution down to 25 cm/pixel) obtained by the High Resolution Imaging Science Experiment (HiRISE) aboard the Mars Reconnaissance Orbiter (McEwen *et al.*, 2007), plus digital elevation model products derived from the HiRISE stereo pair and Mars Orbiter Laser Altimeter, were used as a base map for photogeological mapping, localization of the rover, and for strategic planning of the rover drives.

Supporting information

Data generated during this study is provided online as an additional resource on the *Sedimentology* website. A slide pack containing figures, supplementary data and supporting images is provided as a teaching resource (Data S0). A list of all Navcam, Mastcam and MAHLI data can be found (Data S1), along with GIS shapefiles (Data S2), detailed methodologies (Data S3), grain-size data (Data S4), lamination thickness measurements (Data S5), maps depicting the relative positions of mosaics used in this

study (Data S6), a list of supporting images and URLs (Data S7), measurements made using Pro3D software (Data S8) and a high resolution map of visually estimated palaeocurrents (Data S9).

Instrumentation

The Mastcam instrument suite consists of two focusable cameras with a charge-coupled device capable of acquiring full RGB colour images. The left Mastcam (Mastcam Left, or M34) has a fixed focal length of 34 mm and a 15° field of view; the right Mastcam (Mastcam Right, or M100) has a fixed focal length of 100 mm and field of view of 5° (Bell *et al.*, 2017; Malin *et al.*, 2017). The Mastcams are mounted on a pan-tilt mast *ca* 1.9 m above the surface (Maki *et al.*, 2012; Warner *et al.*, 2016). These cameras are the primary scientific cameras aboard *Curiosity*, and are typically used for targeted imaging of outcrops for identifying sedimentary structures, textures, stratal geometries and depositional architecture. Targets are identified during the rover traverse using the Navcams (described below). The spatial resolution provided by the M34 camera is 450 $\mu\text{m}/\text{pixel}$ at 2 m distance from the target to 22 cm/pixel at 1 km distance, whereas the M100 camera provides a resolution of 150 $\mu\text{m}/\text{pixel}$ at 2 m and 7.4 cm/pixel at 1 km from the target (Malin *et al.*, 2017). Providing sufficient grain–grain colour contrast, the M100 is capable of resolving medium sand grains (250 to 500 μm) at a distance of *ca* 3.5 m from the rover. Where grains share similar colours or are dust covered, the ability to resolve grains is diminished. Coverage obtained by the Mastcams limited by data volumes that can be stored onboard (8 Gb per camera) (Bell *et al.*, 2017) and bandwidth limitations associated with interplanetary communications. A full 360° azimuth \times 80° elevation mosaic captured by the M100 camera is *ca* 6.6 Gb of data, which is 14 times larger than the typical daily data downlink capabilities.

The MAHLI is a two-megapixel colour camera with a focusable macrolens attached to the instrument turret on *Curiosity's* robotic arm. At its highest spatial resolution, MAHLI can acquire images of up to 14 $\mu\text{m}/\text{pixel}$ at a 21 mm working distance (Edgett *et al.*, 2012). Typical imaging on Mars is performed in suites of nested images of 16 to 21 $\mu\text{m}/\text{pixel}$, 31 $\mu\text{m}/\text{pixel}$ and 100 $\mu\text{m}/\text{pixel}$ (Yingst *et al.*, 2016). The primary science application of this instrument is

for observation of sediments and sedimentary rock textures, and hand-lens scale sedimentary structures. Image coverage obtained by MAHLI is limited due to planning constraints associated with deployment of the arm, a process which typically takes 2 Sols to complete. Other constraints of deploying MAHLI are described by Yingst *et al.* (2016).

The most complete suite of images that cover the terrain investigated using *Curiosity* is provided by 12 monochrome engineering cameras that are used principally for navigation, hazard avoidance and science target planning (Maki *et al.*, 2012). In this study, data from the Navcams were used primarily, which are mounted on the pan-tilt mast adjacent to the Mastcam cameras. Navcams offer a field of view of 45° and a pixel scale of 0.82 mrad/pixel (Maki *et al.*, 2012). Mosaics produced by these images are used primarily for: navigation; production of three-dimensional terrain models to plan rover drives and robotic arm deployment, and for targeting observations using Mastcam and MAHLI cameras. The Navcams are capable of 360° azimuth panoramic and stereopair imaging (360° stereo mosaics composed of 45 frames are approximately 26 Mbits) out to 100 m from the rover. These mosaics and three-dimensional meshes are used for supplementing Mastcam observations where coverage is sparse and for taking scientific measurements of geological features.

Mastcam image analysis

Mastcam images of significant outcrops were processed to remove the effects of surface radiation and lens distortion, merged into a single mosaic, and adjusted to preserve geometric relationships within the projection. Stereopair mosaics taken by Navigation cameras are used to triangulate distances and generate a 3D mesh of the environment surrounding the rover (Alexander *et al.*, 2006). Points and distances between points observed in Navcam and Mastcam mosaics were measured in Navcam stereomesh to determine the dimensions of geological features, such as bedding thicknesses, lamination lengths and lateral extents of surfaces or architectural elements. The spatial resolution of the mesh permitted accurate measurements to the decimetre-scale, but the resolution was insufficient to measure at the millimetre-scale. Decimetre-scale cross-sets in close proximity to the rover were measurable; however, the

thicknesses of laminations or grains were not measurable. Mosaics were interpreted using vector graphic software to highlight facies, geometric relationships between depositional surfaces, unconformities and locations of measurements, such as bed thicknesses, lengths and the coordinates of dip-azimuth measurements.

Mars hand lens imager image analysis

The MAHLI images of targets of interest were used to determine the texture and grain size of facies within the Stimson formation. Working distance and pixel scale for images can be calculated using the focus motor position value (Edgett *et al.*, 2015), allowing measurement of features in the sensor plane. Once working distance and pixel scale were calculated, measurement of grain size was carried out using ESRI ArcGIS[®] software. To negate grain selection bias, a fishnet grid was created and superimposed on the image to randomize grain sampling. The long axis of the grain beneath a grid intersection was measured in pixels; this measurement was then multiplied by the calculated pixel scale to convert the grain length in micrometres. Grain length values were recorded in a shapefile and were exported to Microsoft Excel[®] for analysis using GRADISTAT software (Blott & Pye, 2001). Grain roundness was determined visually using the scale of Powers (1953). Additional details of these methods are given in Data S3.

Cross-bed dip analysis methods

Palaeotransport analysis was performed by visual estimates of cross-bedding foreset dip directions and azimuths of cross-set trough axes using stereo ranging and bearings of points selected on Navcam or Mastcam mosaics, plus the Cartesian coordinates of the point relative to the rover, allowing the point to be projected onto HiRISE images. Cross-set dip azimuths were estimated by identifying outcrop sections approximately perpendicular to the foreset dip direction and recording the bearing of this observation relative to the rover (Fig. 4). Depending on the orientation of the foreset dip direction, 90° is either added (sets dip to the right of the image) or subtracted (sets dip to the left of the image) from the observation bearing to obtain the foreset dip azimuth. Additional refinements to the dip azimuth were applied where set tops or the front of the sets are visible, allowing refinement of the azimuth value depending on whether the sets are dipping left and slightly away from (small addition) or left and slightly towards (small subtraction) the viewer, or right and slightly away from (small subtraction) or right and slightly towards (small addition). Where trough axis orientations were estimated, outcrop sections perpendicular to the trough dips were sought, and the bearing of the observation relative to the rover was recorded. Again, additional refinements to the azimuth value were estimated depending on whether troughs dip towards and left (add) or towards and right (subtract). Where sets in troughs dip away from the rover, the

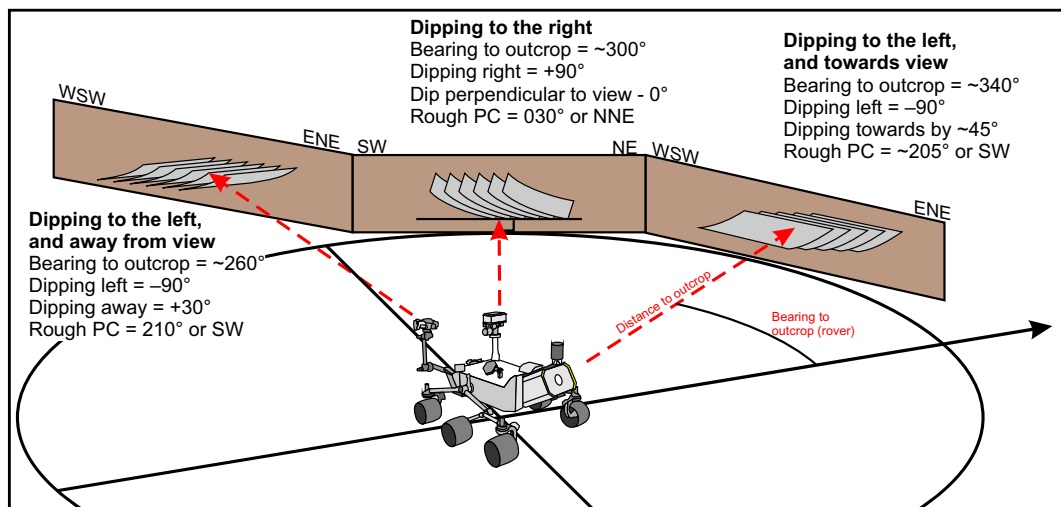


Fig. 4. Cartoon illustrating the method used to visually estimate the dip direction of cross-laminations to determine the dune palaeotransport direction. See text for a full explanation.

orientation of the axis was difficult to estimate, unless laminations were visible in the upper surface of the outcrop.

Attributes related to each cross-bed dip measurement were recorded in a database. These include rover position coordinates, measurement coordinates, bearing and azimuth of measurement, interpreted facies, mosaic examined, elevation, dip orientation relative to the observer, observation notes, estimated dip direction, and compass quadrant. From these data dip directions coordinates and direction were plotted on a HiRISE base map using ESRI ArcGIS®. Statistics related to dip-azimuth measurements such as vector mean and vector magnitude were calculated using methods described by Lindholm (1987) to determine the mean bearing of the palaeotransport direction, and the dispersion of the dip-azimuth values from the mean. All cited compass orientations are given in present day coordinates. The dip-azimuth data are provided as a GIS shapefile in Data S2.

Digital outcrop model analytical tool and methods

Planetary Robotics 3D viewer (PRo3D) (Paar & Consortium, 2016; Traxler *et al.*, 2018) was used to visualize stereo-images collected by the Navcam and Mastcam instruments. Ordered Point Clouds are generated from processed Navcam and Mastcam frames, which are viewed and analysed in PRo3D (Paar *et al.*, 2017). Using this software, dimensions and geometries of features in the landscape, such as set thickness or dip azimuths of cross-lamina can be measured, as described by (Barnes *et al.*, 2015). A more detailed description of this software is given in Data S3.

Nomenclature

Formally, the International Astronomical Union (IAU) determines formal nomenclature for features identified on Mars. In this paper, Earth, Mars, Gale, Aeolis Mons and Aeolis Palus are the only IAU designated features. All other locations, landmarks, landforms and targets of observation were informally named by the MSL Team during the course of surface operations. Internationally, Mars has no formally recognized stratigraphic code and all geological unit names (outcrop, member, formation or group) are thus informal and are not capitalized. The MSL Science team informally names geological units,

landforms, features and rock targets of interest that are investigated using a scheme described by Vasavada *et al.* (2014).

REGIONAL STRATIGRAPHIC RELATIONS OF THE STIMSON FORMATION

The Stimson formation is designated as a distinct sandstone unit that unconformably overlies the mudstone-dominated Murray formation. It forms a series of isolated erosion-resistant outcrops that are distributed along the break in slope between the Aeolis Palus plains and the foothills of Aeolis Mons, and are mostly confined between the –4460 m and –4290 m elevation relative to the Martian datum (Figs 1, 2 and 3). In areas where outcrops were encountered along the rover traverse, the upper boundary of the Stimson is a modern erosion surface and, consequently, the true stratigraphic thickness of the Stimson is currently unknown. Locally, some mesas show up to 4 m thickness of Stimson sandstone preserved above the unconformity. Geological mapping of the Stimson formation on HiRISE satellite images by the Gale Mapping Work Group (Calef *et al.*, 2013) shows the Stimson outcrops to cover a contiguous area of *ca* 1.4 km², with isolated outcrops distributed across an area of *ca* 17 km². The sub-Stimson unconformity was mapped along the traverse using rover-derived data, augmented by analysis of HiRISE images to extend mapping coverage beyond the areas traversed by the rover (Watkins *et al.*, 2016). Watkins *et al.* (2016) show that the unconformity forms an undulating palaeo-surface with relief of up to 20 m over a 275 m distance at Logan Pass. Regionally the unconformity shows a *ca* 140 m rise in elevation traced southward towards Aeolis Mons across a 2 km long north–south oriented profile, with the unconformity dipping north towards the crater rim (Fig. 3B). Traced southward, Stimson formation sandstones overlie Murray formation strata that occur at progressively higher elevations. Since within the Mount Sharp group strata elevation is a proxy for stratigraphic height, this means that Stimson strata overlie progressively younger Murray formation strata traced southward. Between the outcrops at Logan's Run (–4454 m) and East Glacier (–4429 m), the unconformity rises in elevation by *ca* 25 m (Figs 4 and 5). The absence of distinct marker beds or surfaces within the Stimson renders correlation of stratal packages within the formation impossible between adjacent

outcrops. Set boundaries, although common, are commonly truncated by overlying bounding surfaces, or obscured by regolith, preventing correlation between outcrops. Superbounding surfaces (as defined by Havholm & Kocurek, 1994) that could potentially be used for correlation purposes have not been identified. As a result, for this study, vertical elevation is used for relative positioning of the outcrops, with the sub-Stimson unconformity acting as an additional datum.

RECONSTRUCTING STIMSON DEPOSITIONAL PROCESSES AND PALAEOENVIRONMENTS

In order to establish the sedimentary processes by which the Stimson formation was deposited and to reconstruct its depositional setting, the sedimentology of distinctive lithofacies within the formation and stratal bounding surfaces were studied and are described in this section.

Sedimentary texture

The MAHLI instrument was used to investigate the sedimentary texture, which provides insight into sediment transport processes responsible for depositing the Stimson formation. Owing to the complexity of mission planning, positioning of the rover in a suitable and safe location to deploy the arm and outcrop quality, the sedimentary texture of the Stimson was best

resolved at the Williams outcrop (Fig. 2). Grain-size histograms and measurements of grain size can be found in Data S4.

Description

At the Williams outcrop (Fig. 6A), three targets, all within metre-scale cross-stratified sandstones (Facies 1) were imaged using MAHLI. These targets, Ivanhoe (Fig. 6B), Lebo (Fig. 6C) and Ledger (Fig. 6D), were documented on Sol 1092. These targets were associated with an alteration halo indicated by lightened tone of bedrock (Frydenvang *et al.*, 2017; Yen *et al.*, 2017). The Ivanhoe target was located in an area of intense alteration, Lebo is located 0.65 m away from Ivanhoe where alteration was less intense and Ledger was located largely outside of the area of alteration, 1.2 m from Lebo. Grain-size measurements are provided in Data S4A, along with a histogram of all grain-size measurements in Data S4B.

The Lebo target (Fig. 6C) is on a bedding-parallel face that is eroded through a number of lamination surfaces in a cross-bed foreset. Lebo is characterized by abundant randomly distributed very coarse-grained sand grains, which weather proud from the matrix. Grains in Lebo show a bimodal grain-size distribution (see Data S4C). Coarser grains are generally well-rounded, with some highly spherical grains observed. On closer inspection, some of these coarse sand grains exhibit surface pitting, or a surface rugosity. The matrix is characterized by medium-grained sand infilling the space between the larger grains.

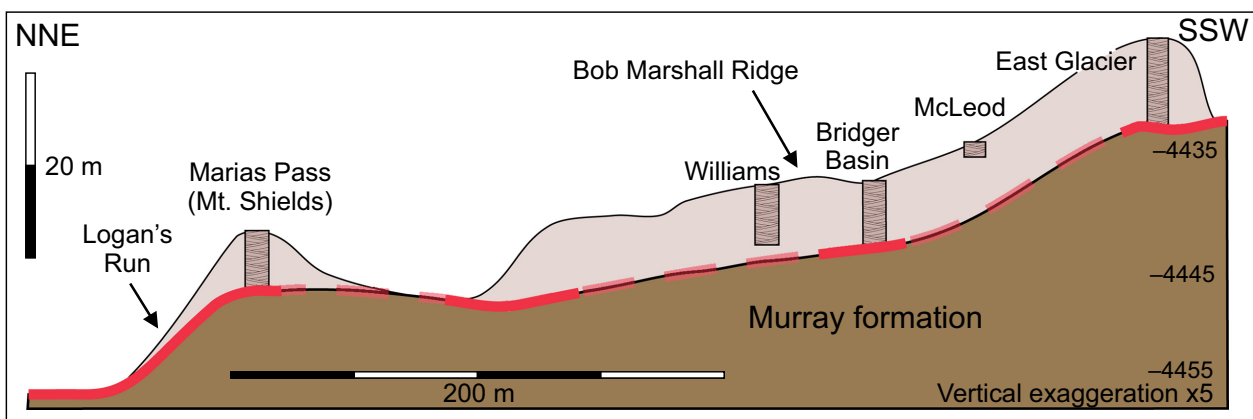


Fig. 5. Fence diagram depicting the stratigraphic relationship between the Stimson formation and the underlying Murray formation. The vertical thickness of the Stimson at each key location is depicted by sedimentary logs that are positioned according to distance along traverse and vertical elevation. Solid red lines indicate direct observations of the sub-Stimson unconformity; dashed lines indicate locations where the unconformity is inferred at depth. The fence diagram illustrates the likely onlap of the Stimson formation onto palaeotopography formed at the erosion surface cut into the Murray formation.

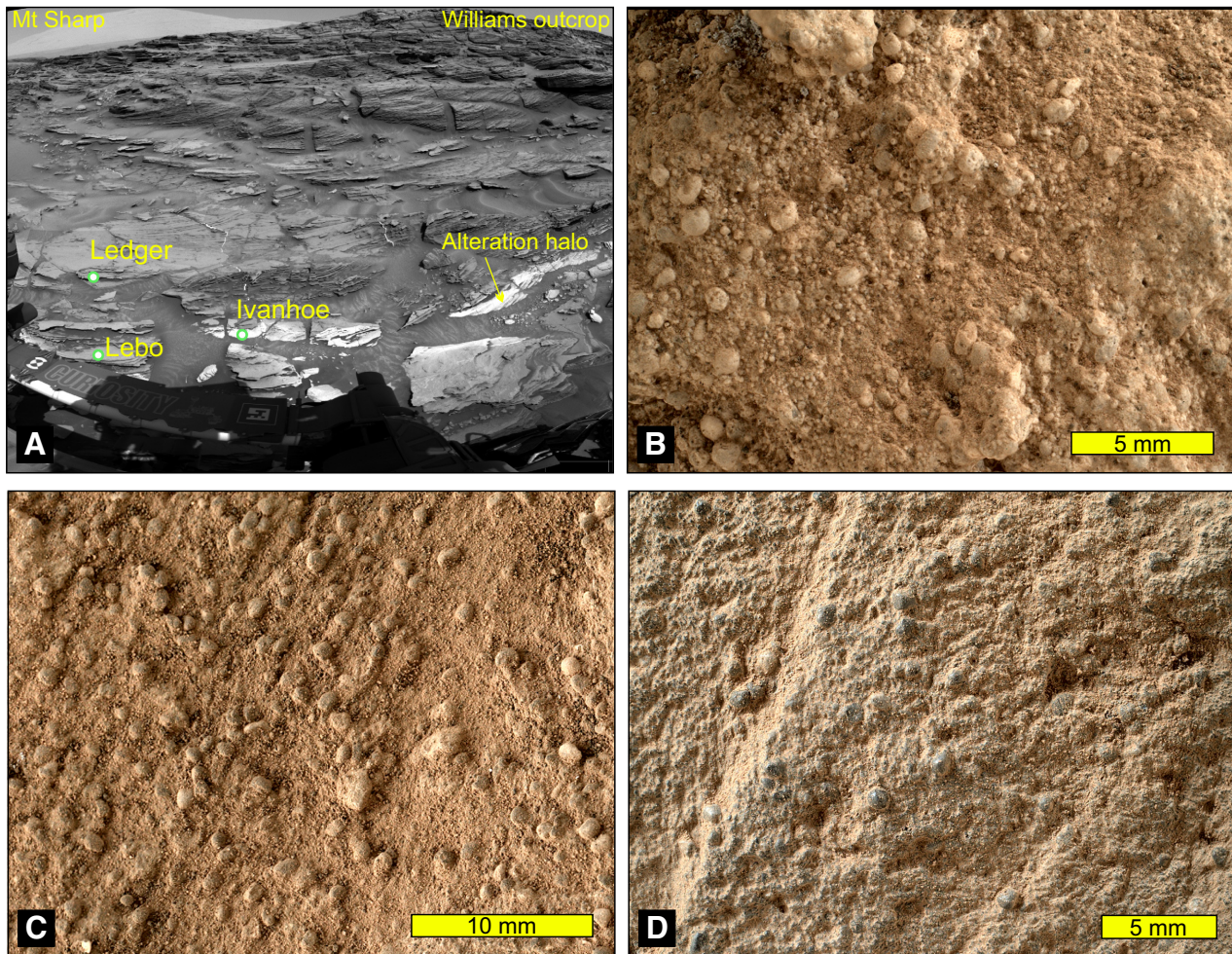


Fig. 6. Mars Hand Lens Imager images taken at the base of Williams outcrop on Sol 1092. (A) Overview Navcam mosaic depicting location of MAHLI targets (Sol 1087 end-of-drive position). Field of view is 2.5 m. (B) Ivanhoe Target, 2 cm stand-off. Target was located in alteration halo. Grain-surface texture and bimodal sorting can be observed. Note pitting on grain surfaces. (C) Lebo Target, 5 cm stand-off: MAHLI image recorded the top surface of a lamination, characterized by bimodally sorted rounded grains. Surface exhibits a light dust covering. (D) Ledger target, 2 cm stand-off: MAHLI imaged area cleared by dust removal tool, revealing bimodally-sorted, well-rounded, medium-grained sandstone. Grain surfaces are smooth and have a polished appearance. The MAHLI images are available on the NASA PDS website. Image credit: NASA/JPL-Caltech/MSSS.

Grain-size analysis of 236 grains yields a bimodal grain-size distribution characterized by two peaks, one at the 355 to 500 μm ($\phi 1.0$ to $\phi 1.5$) and the second at the 710 to 1400 μm ($\phi 0.5$ to $\phi -0.5$) range. The minimum grain size was 182 μm , a maximum of 2596 μm , and an average size of 691 μm was recorded. The colour of the coarse grains is varied, with white, tan and grey-coloured particles, suggesting varied mineralogy of the constituent grains.

The Ivanhoe target (Fig. 6B) is on a broken rock surface with no bedding surface visible. The Stimson here has undergone post-depositional alteration (Yen *et al.*, 2017) as indicated

by lighter toned colour by comparison to the Lebo target. Ivanhoe is also characterized by a bimodal grain distribution. Abundant coarse grains were observed and these are well-rounded and spherical in shape. On closer inspection, these coarse grains exhibit pronounced surface pitting compared to grains in Lebo. Grain-size measurements of 253 randomly selected grains indicates two peaks centred on the 180 to 250 μm ($\phi 2.5$ to $\phi 2.0$) and >710 to 1000 μm ($\phi 0.5$ to $\phi 0$) distributions (see Data S4C). The mean grain size for this sample is 406 μm , with a minimum of 85 μm and maximum of 1297 μm .

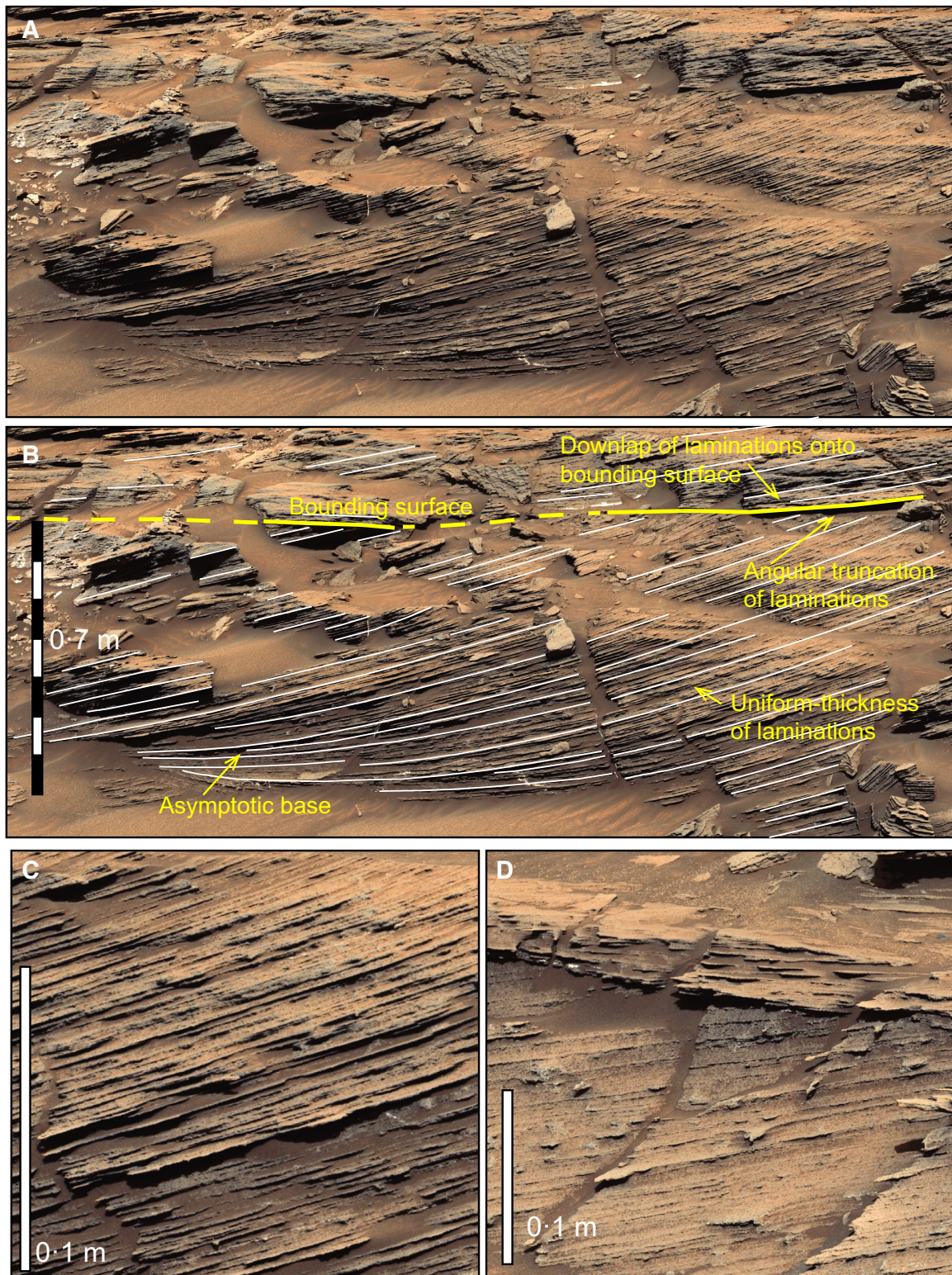


Fig. 7. Facies 1 – Metre-scale planar and trough cross-bedding, recorded at the Williams outcrop (M100 Mastcam mosaic acquired on Sol 1092, mcam04793, at the end-of-Sol 1087 rover position). (A) Uninterpreted example of a single cross-bed set (Coset 2, Figure 14). (B) Interpretation of same cross-bed set, showing geometries of key features of laminations and bounding surfaces. (C) Close up of cross-laminations within set observed in (A) and (B). Laminations are typically 2 to 4 mm in thickness, and show uniform thickness along their length. (D) Close-up of bounding surface truncating cross-laminations at the Williams outcrop. Image credit: NASA/JPL-Caltech/MSSS.

The Ledger target (Fig. 6D) is an unaltered section of the Stimson formation, which was brushed by the Dust Removal Tool (DRT) before MAHLI imaging was undertaken. The target is an approximately bedding-parallel section, which cuts across four cross-lamination surfaces. Grain-size measurement of 259 grains confirmed a normal grain-size distribution, with a dominant peak at 250 to 355 μm ($\phi 1.5$ to $\phi 2.0$) (medium-fine grained) and a coarse skew. The mean grain size for this sample was 398 μm , with a minimum grain size of 132 μm and maximum recorded as 1604 μm (see Data S4C). Cementation of the sandstone at Ledger appears to be different from that at the other two targets, in that the grains appear less pronounced. The larger very coarse grains are highly spherical and very well-rounded, and have extremely smooth surfaces, with little or no pitting observed. Within the very coarse fraction of grains, several examples of tan, light grey and dark grey-coloured grains were observed, suggesting variable grain mineralogy.

Interpretation

The bimodal grain-size distribution observed is characteristic of wind-blown sediments (Sharp, 1963; Greeley & Iversen, 1985; Jerolmack *et al.*, 2006), in which saltating particles can facilitate transport of grains too large to saltate by surface creep. The high degree of grain rounding observed in the MAHLI targets is characteristic of grains transported by aeolian processes (Folk, 1980; Garzanti *et al.*, 2015; Garzanti, 2017). Such a high degree of rounding is typically not achieved by sub-aqueous transport, which is relatively ineffective at rounding sand grains (Pettijohn, 1957).

Characteristics of Stimson sedimentary rocks

To aid interpretation of Stimson strata in terms of depositional processes, four sedimentary facies were identified, each characterized by a unique lithology and sedimentary structures. Here these facies are described and interpreted in terms of their process of formation.

Facies 1 – Metre-scale planar and trough cross-bedding

Description. The Stimson formation is dominated by metre-scale cross-bedded sandstone facies. This facies consists predominantly of medium-grained sandstones; however, in some locations the sandstones contain up to 5%

coarse to very coarse sand grains with diameters up to 2 mm. At a distance, this facies is composed of cross-stratified sandstones with cross-sets arranged as repetitively stacked sets typically ranging between 0.3 m and 1.0 m in thickness. Stacked sets which share a common cross-lamination dip azimuth are defined as cosets and have thicknesses ranging from 0.5 m thick to greater than 1.5 m in thickness. The sets are bounded by sub-horizontal bounding surfaces, which are described below. Cross-strata within sets comprise inclined parallel laminations, and typically show an arcuate, concave-up profile.

A close-range mosaic illustrates the main features of cross-stratification within the Stimson (Fig. 7). The set is composed of repetitively arranged, sub-parallel, relatively uniform thickness millimetre-scale laminations that can be traced across the entire cross-set. The thickness of laminations ranges from 2.8 to 8.5 mm, with an average of 4.1 mm \pm 1.9 mm (measurements are provided in Data S5). These laminasets are characterized by nearly uniform thickness, exhibiting only sub-millimetre variations in thickness along much of their length (Fig. 7C and D). It was not possible to determine grain-size variations within laminae or laminasets; at the closest proximity to the Williams outcrop (6.5 m), resolution was 0.5 mm/pixel, which would only allow identification of grains >1.0 to 1.5 mm in diameter. Despite these limitations, a millimetre-scale rough surface texture was observed on the surfaces of laminations, even though individual grains cannot be identified. Cross-lamination lengths range from tens of centimetres to 2 m.

Within the set, laminations are planar in the upper part but when traced to the base of the set they show an asymptotic relationship with the lower bounding surface. Analysis of dips from a digital outcrop model (DOM) indicate a maximum average dip of 22° in Set 2, with a maximum recorded dip of 27° and *ca* 15° in the centre of the set (Fig. 7).

Within cross-sets, there is no clear evidence for the preservation of grainflow strata, wedge-shaped sediment packages that thin and terminate down-dip towards the set base and are formed by lee-slope avalanching. Where viewed in planform section, laminasets are parallel, and largely straight with uniform thicknesses over distances of up to 3 m. Beyond 3 m distance, lengths are difficult to trace due to the presence of regolith, fractures or cross-cutting bounding

surfaces. Where laminasets are exposed in plan-view, they can appear straight or slightly curved with a concave curvature in the direction of lamination dip. Where set-bounding surfaces truncate underlying sets, the underlying cross-laminations show a toplap relationship with the bounding surface, and exhibit an angular discordance typically between 15° and 20° (Fig. 7). Where viewed in sections perpendicular to sediment transport direction, sets of cross-strata form scallop-shape or cylindrical-scour troughs (similar to those described by Collinson *et al.*, 2006), with observed widths in excess of 6 m in the plateau between Marias Pass and Williams outcrop.

Interpretation. Metre-scale planar cross-bedding is interpreted to represent the preserved lower lee slopes of migrating aeolian dunes (the dune plinth). Where sediment supply into the depositional environment is in surplus, the spacing between dunes migrating across a depositional surface (*sensu* Kocurek & Havholm, 1994) decreases until the interdune area is limited to scour pits between dunes. As scour pits migrate across the stoss slope of the down wind dune, the stoss slope and upper part of the lee slope are eroded, with the remaining lower portion of the lee slope being subsequently buried by advance of the following dune. The erosion surface formed by migration of the scour pit is referred to as a set bounding surface (Brookfield, 1977; Rubin & Hunter, 1982; Kocurek, 1991). Where these sets are associated with horizontal and laterally extensive scour surfaces, they most probably represent the migration of simple main dunes within the dune field. The cross-lamination dip direction represents the azimuth of net sediment transport

at the time of deposition. Troughs present in sections perpendicular to sediment transport direction are diagnostic of the migration of 3D or sinuous-crested bedforms.

The repetitive, uniform thickness cross-laminations that make up the cross-sets are interpreted as pinstripe laminations formed by wind ripples. Migration of wind ripples across dune lee slopes generates translantent ripple-strata and reworks previously deposited sediments (Hunter, 1977a; Fryberger & Schenk, 1988; Eastwood *et al.*, 2012; Ewing *et al.*, 2017).

Facies 2 – Decimetre-scale trough cross-bedding

Description. This facies comprises cross-bedded sandstones that consist of sets typically between 0.05 m and 0.2 m thick, but occasionally up to 0.4 m thick, with cosets that are typically less than 1 m thick (Fig. 8). Individual sets comprise cross-laminations that are similar in appearance to those in metre-scale cross-beds. These cross-laminations can be traced laterally within the set for a few tens of centimetres, and typically no more than 0.6 m. Cross-laminations terminate at the base of the set with either an asymptotic, or a tangential profile. Lower set boundaries associated with this facies can be traced laterally for no more than 1 to 2 m before they are truncated by a successive set, or are obscured by regolith.

Interpretation. The thin cross-bed sets that characterize this facies are interpreted to result from: (i) a small preserved section of a large-scale aeolian bedform, for example the edge of a trough; (ii) the preserved expression of small sinuous-crested aeolian dunes migrating in the lee of larger bedforms, where the local wind-

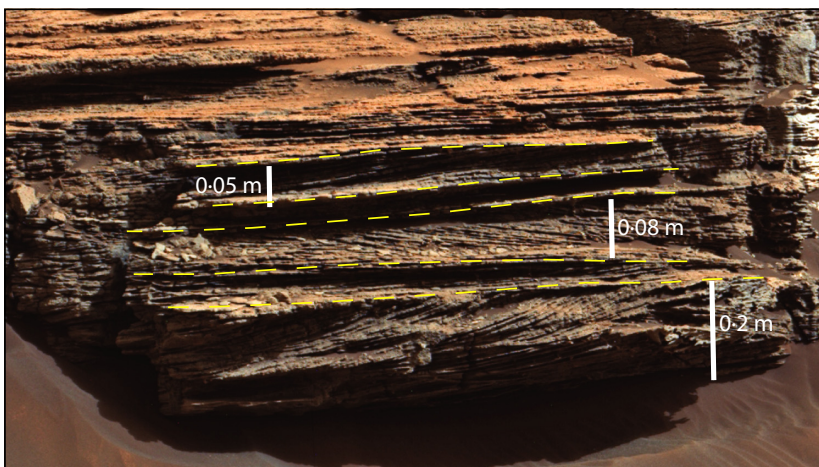
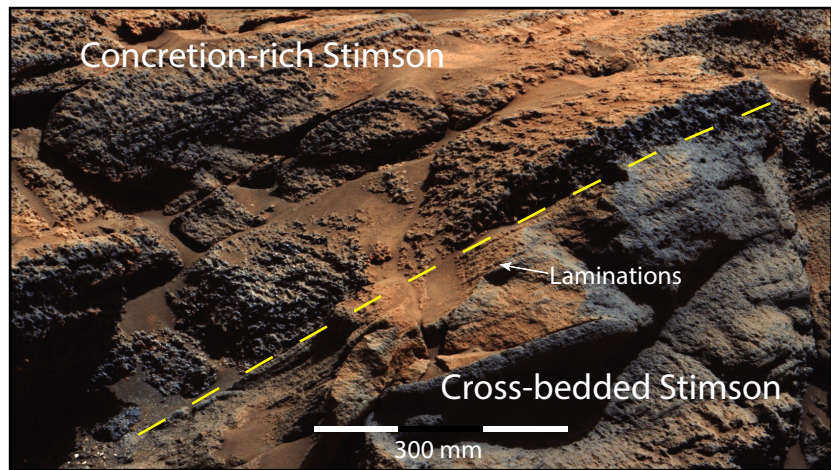


Fig. 8. Facies 2 – Decimetre-scale trough cross-bedding, observed at Apikuni Mountain, Marias Pass (mcam04395). Yellow dashed lines indicate bounding surfaces between sets, which are demarcated by erosive truncation of underlying laminations and asymptotic onlap by overlying laminations. Note that decimetre-scale sets are significantly thinner than sets observed in facies 1. Mastcam-100 mosaic mcam04395 was taken on Sol 993, from the end-of-Sol 992 drive position. Image credit: NASA/JPL-Caltech/MSSS.

Fig. 9. Facies 3 – Concretion-rich sandstone facies observed in Marias Pass. Amalgamated concretions are observed to overprint cross-bedded sandstones in the upper part of the mosaic, with the lower part of the outcrop appearing to be largely devoid of concretions. The origin of this sharp boundary is uncertain, but may represent a difference in permeability. Mastcam-100 mosaic mcam04719 was taken on Sol 1073 at the end-of-Sol 1067 drive position. Image credit: NASA/JPL-Caltech/MSSS.



field is influenced by larger bedforms (Rubin, 1987; Langford & Chan, 1993); or (iii) the preserved expression of large ripples or wind-drag ripples (Lapotre *et al.*, 2016, 2017; Ewing *et al.*, 2017). The latter represent an intermediate class of bedform identified only on Mars that fall between impact ripples and dunes in size. These may be preserved either by ripple climbing processes or may be preserved when they are buried by larger migrating dune-scale bedforms.

Facies 3 – Concretion-rich sandstone facies

Description. Facies 3 comprises sandstones of the metre-scale and decimetre-scale cross-bedded facies but with abundant spheroidal concretions (Fig. 9). From a distance, these protrusions give the Stimson a characteristic ‘knobbly’ surface texture. Although not ubiquitous across the Stimson, Facies 3 is typically distributed in Stimson sandstones immediately overlying the basal unconformity, and extends upward from the unconformity into the Stimson by up to a few metres. Concretions are typically between 20 mm and 40 mm in diameter, and have sub-spherical to oblate shapes. Sand-sized grains are observed within concretions, and laminations are seen to pass from the surrounding sandstone through them with no evidence of deformation of laminae. Concretions occur either sporadically distributed through the facies, or densely packed with concretions becoming locally amalgamated and overprinting primary sedimentary structures.

Interpretation. Facies 3 is interpreted to be the product of post-depositional diagenesis, in

which preferential cementation of the sandstone generated concretions which, when exposed at the surface, better resist erosion than the surrounding sandstone. Evidence that these protrusive features represent concretions rather than nodules comes from the identification of grains and laminations within them and the absence of deformation of laminations and beds surrounding the concretion, which would be typical of incipient nodule growth. On Earth, preferential cementation of sandstone concretions occurs by pervasive growth of a crystal through the pore space surrounding sand grains, from a single nucleating centre point (Clarke & Stoker, 2011), where the cement will probably grow by precipitation of elements from chemically saturated pore fluids. The exact mineralogy of the cement generating these concretions is presently unknown; however Alpha Particle X-ray Spectrometer (APXS) analysis of concretions indicates that the bulk chemistry is similar to the bulk of the Stimson formation (Siebach *et al.*, 2017). The dominant control on the density of concretions formed at any location is uncertain and probably involved a number of factors, including the presence of minerals which can act as a nucleus for cement precipitation, pore water chemistry providing ions to sustain concretion growth, and a source of ions, potentially derived from the host rock, ground water movement or infiltrating meteoric waters (Clarke & Stoker, 2011; Arribas *et al.*, 2012).

Facies 4 – Sandstones with Murray formation mudstone clasts

Description. This facies consists of medium to coarse-grained sandstone containing matrix-

supported clasts that are up to 3.5 mm in diameter. Where visible, sand grains are polymict, well-rounded and commonly show a polished surface, although some examples show surface pitting. Intraclasts are rounded, oblate to sub-spherical in shape, and exhibit a similar colour to the underlying Murray formation. Some examples of these clasts exhibit a weathering-inward profile, where the centre of the clast weathered inward relative to the rim of the clast, suggesting that the clast was made of a relatively soft material. The sandstone is crudely planar laminated, with laminations being 3 to 5 mm thick. The facies only occurs as a 0.5 m wide and 30 mm thick lens in the lowermost few centimetres of Stimson strata in the Missoula area of Marias Pass (Newsom *et al.*, 2016). The lens onlaps and pinches out onto an inclined section of the unconformity, which shows local relief of 20 cm.

Interpretation. The mudstone clasts observed in this facies are interpreted to have been derived from the Murray formation, because of their similar visual expression. They were probably eroded from the underlying Murray formation mudstones and incorporated into the base of the Stimson formation by aeolian processes, and the lens probably formed contemporaneously with erosion occurring on the unconformity. Clasts are interpreted to have formed by exfoliation and abrasion in an interdune area and were incorporated into the base of a migrating dune. This facies is restricted to the immediate vicinity of the unconformity, because after a period of dune accumulation, the unconformity – the source of the clasts – became buried, preventing further supply of mudstone clasts. However, the absence of additional evidence for deposits clearly formed by sub-aqueous processes favours aeolian incorporation.

Bounding surfaces

Within facies 1 and 2, three commonly occurring types of bounding surfaces were observed within the Stimson formation. The common characteristics of the surfaces are described here.

Dune migration surfaces

Description. Cross-bed sets are bounded by truncation surfaces which are ubiquitous within the Stimson formation and are an easily distinguishable feature in outcrops across the traverse.

An example of such a bounding surface is illustrated in Fig. 7 which shows cross-laminations terminating onto the lower bounding surface, and the truncation of cross-laminations in the upper part of the set by an upper bounding surface. Throughout the Stimson, these surfaces are expressed at a gross scale as largely sub-horizontal, sub-parallel surfaces that can be traced laterally across outcrops for distances of up to 30 m in the best exposed outcrops. Locally, they are observed to undulate by a few tens of centimetres along their length, causing variations in set thickness where they downcut into the underlying set. In some cases, these surfaces downcut sufficiently to truncate underlying sets, resulting in the pinch-out of cross-bed sets.

Interpretation. The geometry of these bounding surfaces and their relation with laminasets leads to the interpretation that they represent the erosional passage of a scour pit preceding the advance of an aeolian dune. These surfaces are similar to first-order bounding surfaces (Brookfield, 1977; Kocurek, 1981b) or interdune surfaces (Mountney & Thompson, 2002). The migration vector of the depression and ensuing angle of climb of the dune is controlled by the rate of sediment accumulation, with net sediment accumulation causing a positive angle of climb and sediment preservation, and net sediment entrainment causing a negative angle of dune climb and scouring of previously accumulated sediment. The angle of climb, while not measured here, is typically measured as a few tenths of a degree to a couple of degrees in ancient aeolian systems on Earth (Rubin & Hunter, 1982; Mountney *et al.*, 1999; Mountney, 2006; Rodríguez-López *et al.*, 2014). Where bounding surfaces downcut, this potentially represents autocyclic processes within the dune field, where fluctuating wind strength and direction causes the dune to change shape, height or depth of scour, or an allogenic control where a deficit in sediment supply results in re-entrainment of sediment into the flow (Paola & Borgman, 1991; Ganti *et al.*, 2013; Brothers *et al.*, 2017). Where the dune-bounding surface climbs, this may represent fluctuations in wind strength favourable to sediment deposition or a net increase in sediment flux to allow sediment accumulation.

Superposition surfaces

Description. These surfaces are identified within cosets containing decimetre-scale cross-sets, where the coset bounding surfaces are

defined as dune migration (first-order) surfaces. Decimetre-scale cross-sets within these cosets will share a common foreset dip azimuth, whereas adjacent cosets typically demonstrate a different dip azimuth common to the sets within it. These superposition surfaces can be traced laterally for several metres, but do not have the same lateral extent as the dune bounding surfaces. These superposition surfaces are frequently observed to have a scalloped, or arcuate geometry, with a convex down geometry. Sets bound by superposition surfaces are typically on the order of a few tens of centimetres thick, whereas the cosets containing them have thicknesses similar to that of a metre-scale cross-set.

Interpretation. Superposition surfaces, described as second-order surfaces, represent the migration of smaller bedforms across a larger main dune, giving rise to the observed compound cross-strata (Brookfield, 1977; Kocurek, 1991). Compound dunes, with small dunes migrating across larger dunes are common in Earth-based aeolian systems (Breed & Grow, 1979; Lancaster, 1988) and frequently have crestlines oblique to that of the main dune crestline on which they are superimposed. As these superimposed bedforms migrate across the lee slope of the main dune, scour pits preceding their advance will scour the main dune lee slope generating the superposition surface, with the cross-laminations within the decimetre-scale cross-sets representing the lee slope advance on the superimposed bedform. The associated first-order bounding surfaces represent scouring in advance of the main dune.

Reactivation surfaces

Description. Within cross-bed sets, arcuate and inclined bounding surfaces, originally described as intraset surfaces, can be observed. These commonly truncate cross-laminations obliquely, are discordant to underlying cross-laminations and are overlain by cross-laminations concordant to the bounding surface. Within the cross-set, these bounding surfaces downlap asymptotically to the lower set-bounding surface, and are truncated by the upper set-bounding surface.

Interpretation. Reactivation surfaces, referred to as third-order surfaces (Brookfield, 1977; Schenk *et al.*, 1993), form by fluctuations in air flow. These surfaces have been demonstrated to arise by changes to the height and shape of bedforms, or speed and direction of dune migration, where the bedform generating the cross-strata could

not fully respond (Brookfield, 1977; Kocurek, 1991). Causes of these changes are interpreted to arise from wind reversal or seasonal variations in wind direction and velocity (Mountney, 2006), or by modification of the local wind field caused by migration of adjacent dunes (Brookfield, 1977).

SEDIMENTARY AND STRATIGRAPHIC ARCHITECTURE

To reconstruct the palaeomorphology and stratigraphic evolution of the Stimson depositional system, the following key features were analysed: (i) the outcrop-scale architecture and the geometric relations of the facies; and (ii) the relationship of these outcrops to the underlying sub-Stimson unconformity. Here the study focuses on the section traversed by the rover between Logan's Run and East Glacier. The stratigraphic architecture provides a record of the style of deposition and sediment accumulation, the dominant transport direction, and the relationship between the Stimson formation and the underlying Murray formation.

The architecture of the Stimson observed on the traverse can be synthesized into four generic architectural elements, which contain facies in predictable vertical and lateral arrangements with distinctive geometric properties. These relationships are summarized in Fig. 10. To aid the reader with understanding the complex relationships, a description of the sedimentology at key locations along the traverse is provided in the following section. The map positions of mosaics used in this section are documented in Data S6, along with additional online materials in Data S7.

Sub-Stimson unconformity and palaeotopography: Mount Stimson and Logan's Run

Description

Evidence for a stratigraphic unit overlying the Murray formation was first observed after leaving the Pahrump Hills area (Sol 957, Figs 2 and 11, for mosaic context see Data S4); however, neither the exact nature of this unit nor the relationship with the underlying Murray formation were established until the rover entered the Logan's Run area after Sol 964. At Mount Stimson (Figs 2A and 12A), a sharp

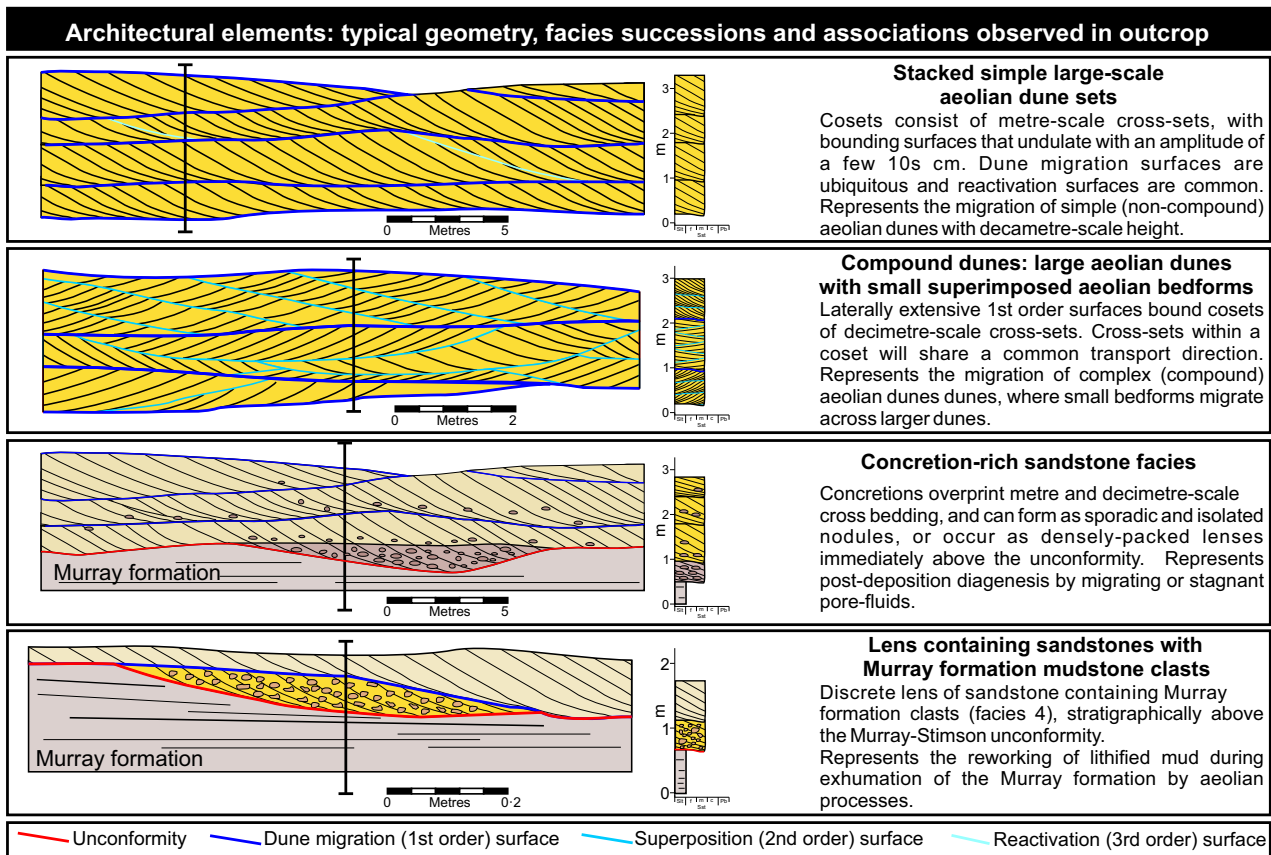


Fig. 10. Representative architectural elements, depicting idealized geometries and internal facies composition of the principal architectural elements of the Stimson formation.

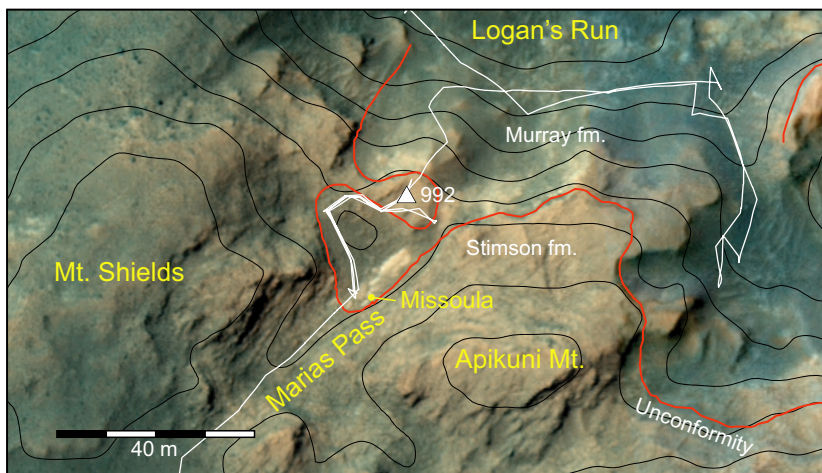


Fig. 11. Overview map of Marias Pass area depicting the locations of Logan's Run, Mount Shields, Apikuni Mountain and the Missoula area. The position of the rover relative to these locations is demarcated by a white triangle. The red line indicates the outcrop of the Murray–Stimson unconformity. Contours (black lines) represent 2 m increases in vertical elevation. Image credits: NASA/JPL/University of Arizona.

contact was observed to separate dark-toned, bedded and blocky *ca* 6 m thick sandstones from the underlying relatively light-toned, apparently homogeneous and smooth-surfaced Murray formation. The Stimson formation was

named after this peak where the contact was first clearly recorded.

At Logan's Run, a north-facing ramp composed of Murray formation mudstone is observed, with outcrops of Stimson sandstone

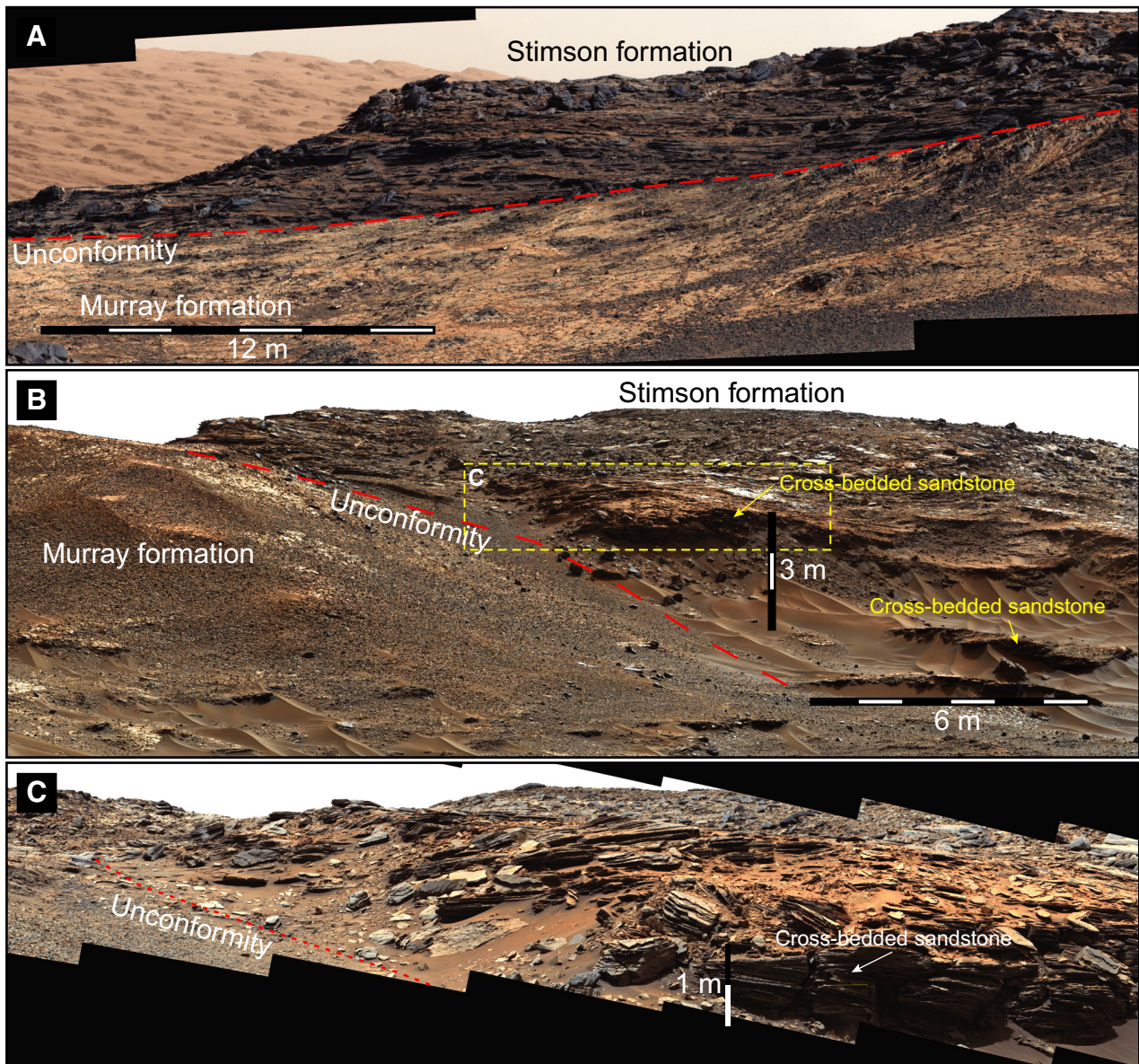


Fig. 12. Mount Stimson and Logan's Run A context image giving an overview of the area can be found here: <https://mars.nasa.gov/resources/7180/>. (A) Mosaic showing the unconformity observed at Mount Stimson – the first location where the sub-Stimson unconformity was clearly identified Mastcam-100 mosaic mcam04330 was captured on Sol 980 from the sub-Sol 978 end-of-drive position. (B) Mosaic shows the Stimson formation onlapping onto the Murray formation, the elevation difference between the base and top of the slope is *ca* 8 m. At this location, over 10 m of vertical exposure of Stimson is observed. Mastcam-34 mosaic 04273 was captured on Sol 964 from Sol 963 end-of-drive position. (C) Close-up of Stimson formation on west side of ramp at Logan's Run. Cross-bedded sandstones are clearly visible above the unconformity. Mastcam-100 mosaic mcam04380 was captured on Sol 911 from the end-of-drive location on Sol 990. Image credits: NASA/JPL-Caltech/MSSS.

overlying it across the height of the slope (Fig. 12B). The slope shows *ca* 7 m of vertical relief over 26 m distance, with the observed stratigraphic thickness of the Stimson overlying it measuring *ca* 10 m thick from the base to the lower part of Mount Shields. The thickness of

Stimson here is likely to be slightly higher as the top of Mount Shields is occluded in the mosaics. The Stimson formation exposed on the slope is blocky, with cross-set troughs present in most parts of the outcrop (Fig. 12B and C). Bounding surfaces can be identified, with a

mixture of sub-horizontal and inclined surfaces. The sub-horizontal bounding surfaces appear to truncate against the sub-Stimson unconformity when traced to the south (Fig. 12C). Sub-horizontal bed sets of Stimson strata terminate against the unconformity, suggesting an onlap relationship.

Interpretation

The boundary between the Stimson and Murray formations observed at Logan's Run and Mount Stimson is a sharp contact and exhibits marked vertical relief over a short distance. The geometries of bounding surfaces in the Stimson suggest that the Stimson has not been tilted or deformed since deposition, and that it was probably formed by deposition of the sandstone

directly against the inclined surface. The contact is interpreted to represent an unconformity along which the Murray formation experienced substantial erosion before deposition of the Stimson (Watkins *et al.*, 2016). The observation of onlap of Stimson formation sandstones onto an inclined unconformity surface indicates that the unconformity here is characterized by local vertical palaeo-relief on the order of several metres.

Geometry of the unconformity and architecture of compound dunes at Marias Pass

Description

The Stimson formation was first studied in detail at Marias Pass, a col that separates two

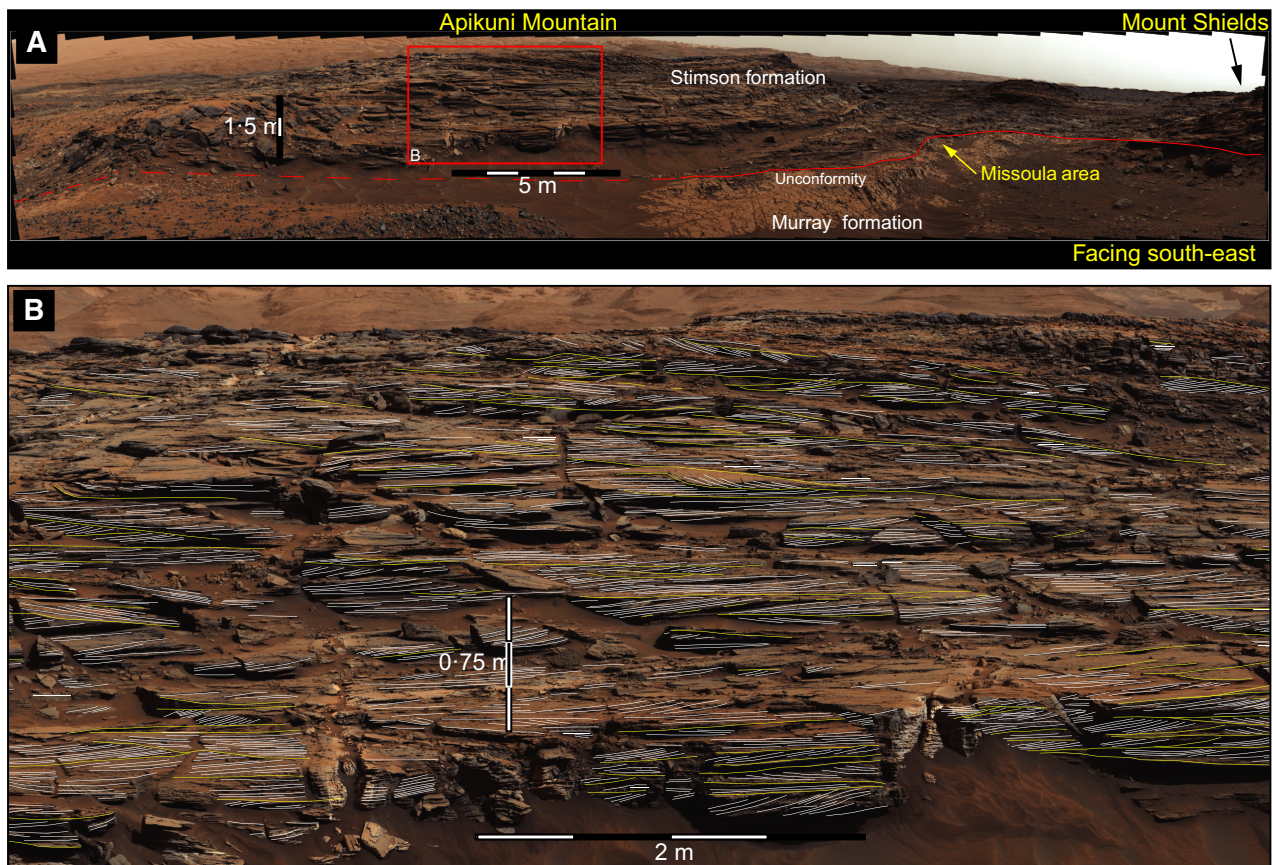


Fig. 13. Marias Pass area. A context Navcam mosaic is available at <https://mars.nasa.gov/resources/7600/>. (A) Mastcam-100 mosaic of Marias Pass area, covering a field of view between 090° and 240°, showing the location of Apikuni Mountain, Mount Shields and Missoula area (mcam04395). The unconformity is observed to run along the base of Apikuni Mountain, through the Missoula area and back around to the base of Mount Shields (see map, Fig. 10). (B) Mastcam-100 close-up image of Apikuni Mountain, with interpretation of stratigraphic architecture preserved. Cross-laminations are interpreted in white, and bounding surfaces are highlighted as yellow surfaces. Mcam04395 was taken from end-of-Sol 992 drive position, on Sol 993. Image credit: NASA/JPL-Caltech/MSSS.

outcrops of Stimson sandstone – Mount Shields and Apikuni Mountain (Figs 11 and 13A; for mosaic context see Data S4). The Murray formation is well-exposed in topographic lows in the central and eastern areas of the pass (Fig. 13). The sub-Stimson unconformity is clearly visible on both sides of the pass (Fig. 13); it is exposed at the base of Mount Shields and can be traced across the pass to the base of Apikuni Mountain. From the base of Apikuni Mountain, in the Missoula area, the unconformity was traced around to the north side of the outcrop, and towards Mount Stimson (as viewed from

Logan's Pass; Fig. 12). The unconformity at Marias Pass undulates with local palaeo-relief of up to 0.6 m vertically. The elevation of the unconformity at the base of Apikuni Mountain is approximately –4446 m. The Murray formation exposed at the base of Marias Pass is a mudstone, exhibiting a smooth surface texture, tan colour and millimetre-scale planar laminations.

Missoula area

At the south-western end of the Apikuni Mountain outcrop, the sub-Stimson unconformity is

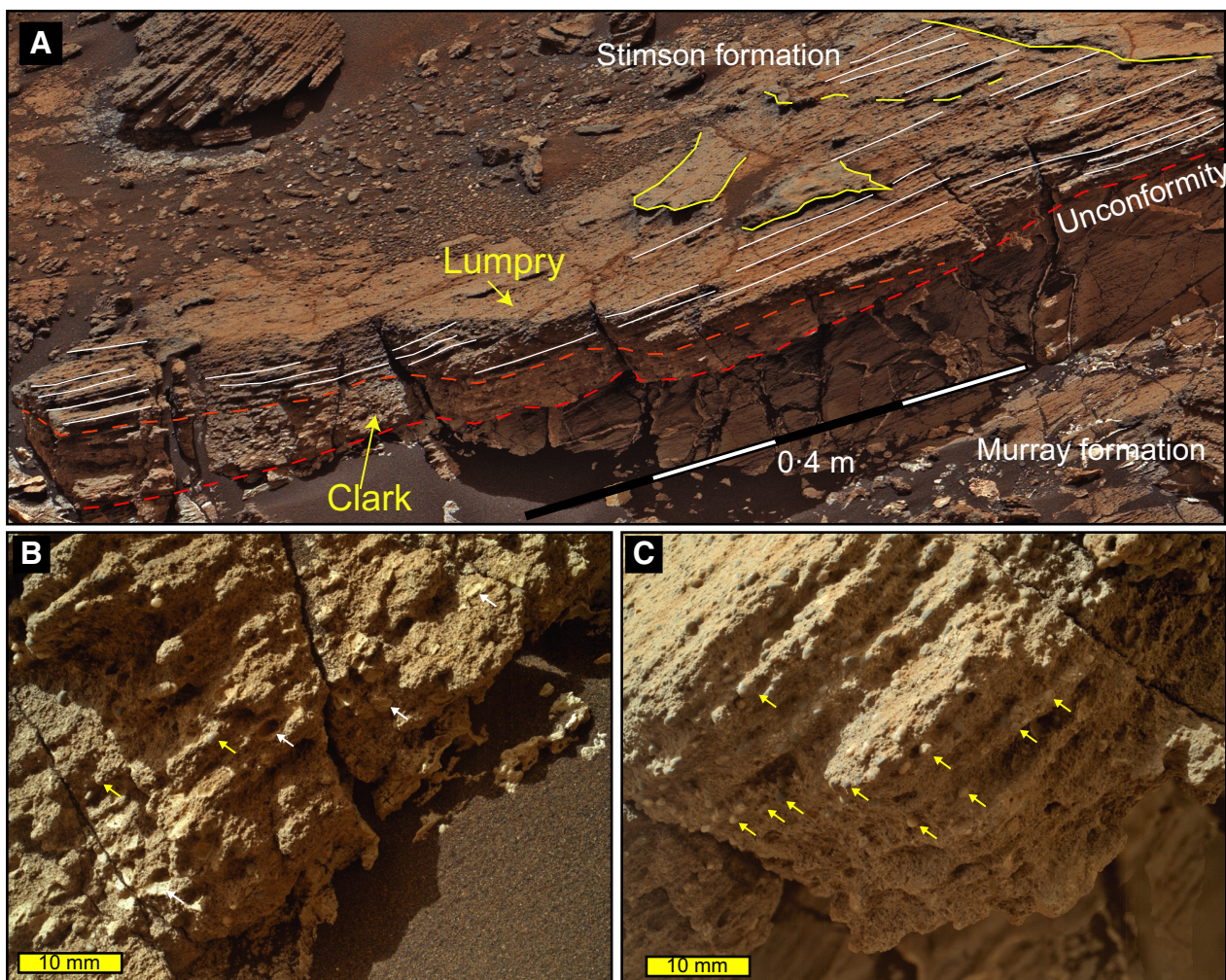


Fig. 14. Missoula area, Marias Pass. A context Mastcam mosaic of the target area is available at <https://mars.nasa.gov/resources/7312/>. (A) Mastcam overview of Missoula area, which straddles the unconformity. Mastcam-100 mosaic mcam04406, Taken Sol 997, at end-of-Sol 995 drive position. (B) MAHLI image of Clarke target, which consists of Sandstones of Murray formation mudstone clasts (Facies 4). White arrows denote mudclasts, yellow arrows denote sand grains. (C) MAHLI image of Lumpry target, which consists of cross-bedded Stimson facies. Yellow arrows highlight millimetre-scale sand grains. See Supporting Information for table of MAHLI images used. Image credit: NASA/JPL-Caltech/MSSS.

exposed in a 0.3 m thick vertical section at the target Missoula (Fig. 14). Here, the basal part of the Stimson weathers proud forming an overhang, whereas the underlying Murray formation forms a recess. The unconformity shows *ca* 0.2 m of relief over *ca* 0.7 m lateral distance, with an apparent dip towards the north-west. The Murray formation at this location is a mudstone. A polygonal fracture network infilled by calcium sulphate veins cross-cuts the laminations in the Murray. Directly above the unconformity, a lens of sandstone, 0.5 m wide, and 30 mm thick, is present that contains clasts of Murray mudstone (Facies 4) (Fig. 14B). MAHLI images (Fig. 14C) show that the lens consists of poorly sorted, medium to coarse-grained sandstone, with grains up to 2 mm in diameter, with cross-laminations that are 2 to 4 mm in thickness. The lens is overlain by a cross-bedded sandstone outcrop, which forms the basal part of the Apikuni Mountain outcrop.

Apikuni Mountain

The north-west-facing slope of Apikuni Mountain forms an outcrop (trending 60 to 240°) *ca* 30 m long and exposes a vertical section of Stimson *ca* 5.5 m thick above the sub-Stimson unconformity (Fig. 13A). The outcrop slopes towards the centre of the pass with an average angle of 14°. The Stimson at Apikuni Mountain is largely composed of decimetre-scale cross-bedded sandstones (Facies 2). At the base of Apikuni Mountain (Fig. 13B) a 0.7 m high step exposes decimetre-scale cross-sets, with set thickness ranging between 0.05 m and 0.2 m, and cross-laminations exhibiting an apparent uniform thickness. Cross-sets at the base of the succession exhibit variable dip directions, with apparent dips to the north-east and south-west of the outcrop. In some cases, troughs are discernible, with their axes aligned north-west/south-east. Above the basal step, the outcrop is sloped and contains larger cross-sets, with thicknesses of up to 0.3 m and lamination lengths of up to 2.5 m. Bounding surfaces in the upper section of the outcrop can be traced for distances of more than 3.5 m before occlusion by superficial material. Cross-lamination dip directions are less variable than the lower section, and a dominant transport direction towards the north-east was recorded. The outcrop is cross-cut by sub-vertical fractures with spacings of >5 m and characterized by distinct light grey alteration halos a few tens of centimetres wide to either side of the fracture. Similar fracture-associated

halos in the Stimson are described in more detail by Yen *et al.* (2017) and Frydenvang *et al.* (2017).

Mount Shields

At the Mount Shields outcrop, on the western side of Marias Pass, the north-east (trending 160°) and south-east (trending 260°) faces of the outcrop are exposed (Figs 11 and 15). The sub-Stimson unconformity is located towards the base of the outcrop; however it is mostly occluded by regolith. The south-east facing outcrop has a stepped profile and exposes a 3.6 m thick succession of cross-bedded sandstones (Fig. 15). Sets show a similar range of thicknesses to those observed at Apikuni Mountain, with sets typically ranging between 0.1 m and 0.40 m in thickness. Set thickness increases from the base of the outcrop, where sets are typically 0.1 to 0.2 m thick, to *ca* 0.4 m thick near the top of the outcrop. The largest set measured was 47 cm thick. Cross-bed foresets in this outcrop exhibit variable dip directions, with a slight bias to sets dipping towards the north-east, suggesting that the outcrop surface is oblique to the axis of sediment transport.

The north-east face of Mount Shields exposes a 3.3 m thick section of Stimson formation (Fig. 15A). The outcrop consists of 0.1 to 0.3 m thick cross-sets, some of which have characteristic trough shapes, bounded by dune migration surfaces which can be traced for distances of *ca* 1 to 2 m. Analysis of the bounding surfaces reveals that some surfaces are more laterally extensive, and can be traced across the outcrop. These surfaces bound groups of sets, forming cosets between 0.5 m and 0.8 m thick. Within these cosets, sets dip predominantly in a common direction (Fig. 15A): Coset A dips predominantly towards the east; Coset B dips predominantly north and east; Coset C dips towards the north and west; and Coset D shows a general apparent dip towards the west. Coset bounding surfaces can be traced from the north-east side of the outcrop, onto the south-east side of Mount Shields, where they are otherwise indistinct from set-bounding surfaces (Fig. 15B).

Marias Pass interpretation

Mudstone clasts within the basal sandstone lens probably represent products of erosion from the underlying Murray formation, reworked into the base of migrating aeolian dunes as dune-field

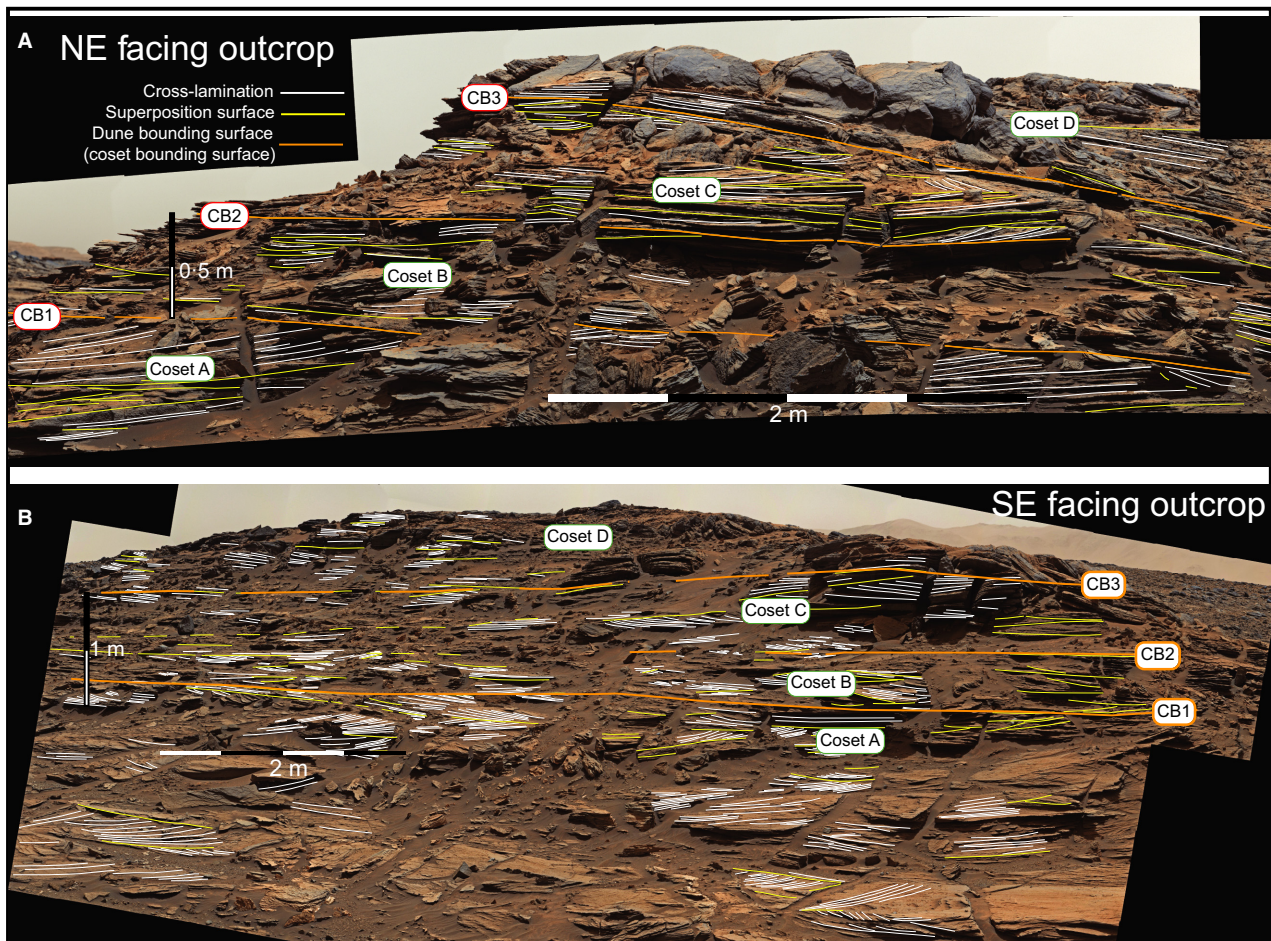


Fig. 15. Mount Shields, Marias Pass. (A) North-east face of Mount Shields. This face of Mount Shields is perpendicular to the dominant transport direction, and exposes trough-shaped cross-sets. Cross-set bounding surfaces can be identified (yellow), and groups of cross-sets (cosets) can be observed to dip in similar directions. Coset bounding surfaces represent major bounding surfaces indicating variation in palaeotransport direction. Four major cosets, separated by three coset bounding surfaces are identified. The general transport direction is towards the observer (north-east). Mastcam-100 mosaic mcam04617 was taken on Sol 1049 from end-of-drive position for Sol 1042. (B) South-east face of Mount Shields. Dune migration surfaces are readily identifiable; however because the dip azimuth of cross-laminations are all in a similar direction, coset bounding surfaces are difficult to distinguish. In this example, coset bounding surfaces have been traced from the north-east facing slope, and inferred along the length of horizontal bounding surfaces at the same elevation. Cross-laminations dip towards the right of the outcrop – towards the north-east. Mastcam-100 mosaic mcam04521 was taken on Sol 1033 from Sol 1030 end-of-drive position. Image credit: NASA/JPL-Caltech/MSSS.

construction ensued. Later, after the dune field was established, the supply of Murray mudstone clasts was eliminated as the sub-Stimson palaeosurface became buried.

The Stimson formation at both Apikuni Mountain and Mount Shields is characterized by small-scale (0.05 to 0.4 m thick) trough cross-sets, which are interpreted to have formed by the migration of small-scale sinuous-crested aeolian dune forms, with smaller sets interpreted to potentially represent large

sinuous-crested ripples. At Mount Shields, bounding surfaces defining decimetre-scale cross-sets are interpreted to be superposition surfaces, while the laterally extensive coset bounding surfaces are interpreted to be interdune surfaces (Brookfield, 1977). Interdune (coset) surfaces correspond to scour pits migrating in advance of a lee slope of a migrating compound dune, with lower-order (superposition) surfaces within the cosets corresponding to scour pits generated by

migration of smaller-scale superimposed bedforms. Cosets at this outcrop show thicknesses similar to large-scale cross-set thicknesses at Williams outcrop, Bridger Basin and East Glacier, later in the traverse, where set thickness corresponds to dune-scale bedform migration. It is uncertain as to whether the small-scale cross-sets represent small-scale dunes (tens of metres wavelengths) or large ripples (metre-scale wavelengths). Within coset C, decimetre-scale cross-sets have maximum thicknesses of *ca* 0.1 m, which would represent the preservation of about one-third of a typical large ripple observed within the present-day Bagnold dune field (Ewing *et al.*, 2017); whether this

proportion of preservation is feasible is uncertain.

Sedimentary architecture of simple dunes preserved at Williams outcrop

Description

The preserved geometry of dune cross-bedding in the Stimson formation is best illustrated at the Williams outcrop (Figs 2 and 16, and context map in Data S4) where relatively close-range M100 imaging of sedimentary structures permitted excellent characterization of the sedimentology in a vertical section. The Williams outcrop is located along a 100 m long, *ca* 5 m high, north-

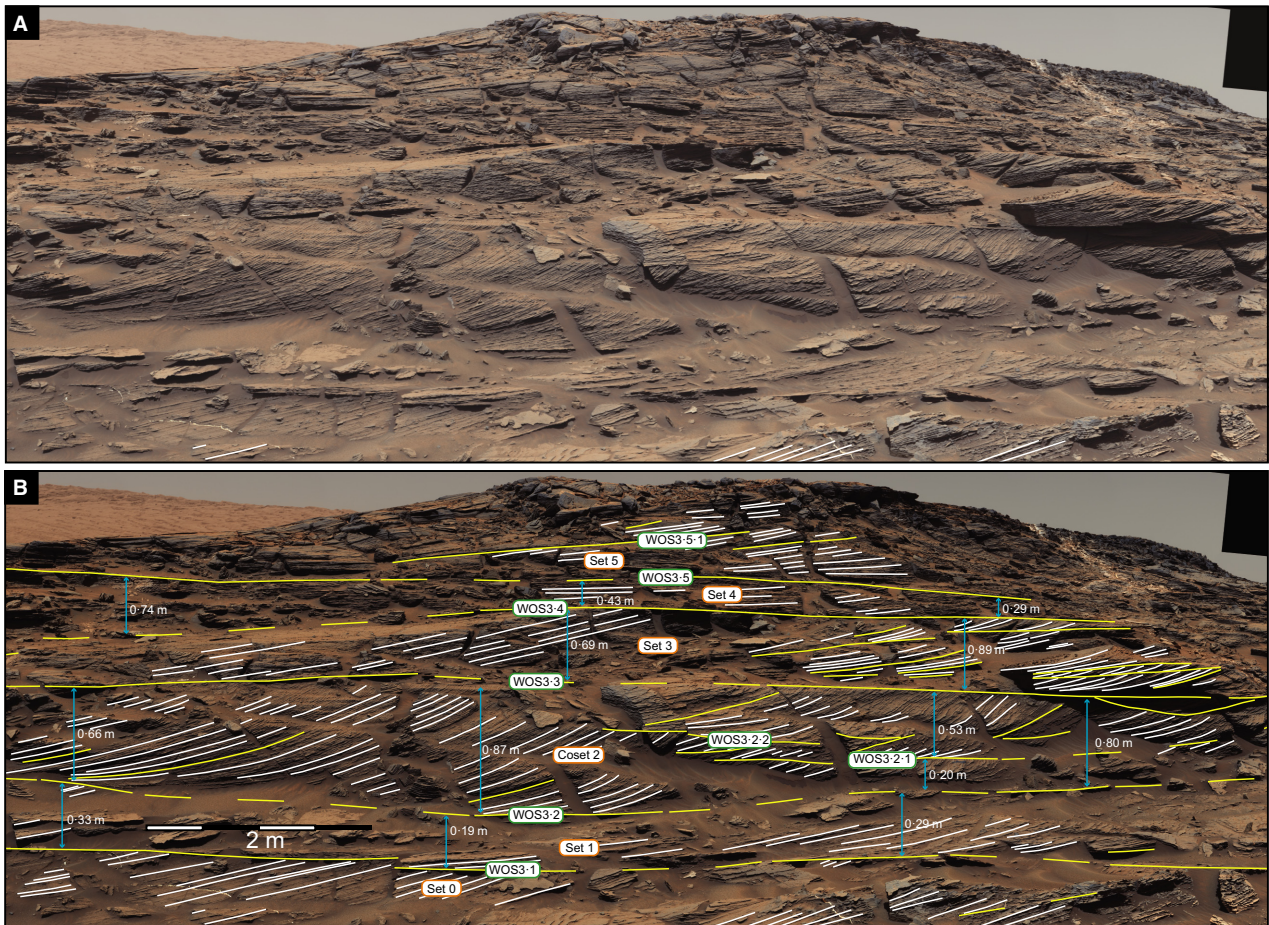


Fig. 16. Williams outcrop, at the south end of the Emerson plateau. A full-size version of this mosaic is available at <https://mars.nasa.gov/resources/7468/>. (A) An uninterpreted view of Williams outcrop. Height of outcrop is 5 m, and slopes towards the point of observation with an average angle of 15°. (B) Interpretation of Williams outcrop mosaic. Cross-laminations are interpreted in white and dune migration surfaces are yellow. Set thicknesses are indicated in blue. Cross-laminations dip towards the left of the outcrop which is towards the north-east. Mastcam-100 mosaic mcam04777, was taken on Sol 1087, at the Sol 1085 end-of-drive position. Image credit: NASA/JPL-Caltech/MSSS.

east/south-west trending ridge named the Bob Marshall Ridge. The main outcrop investigated (Fig. 16) is at the northern end of this ridge and slopes towards the north-west at *ca* 15°. The basal contact between the Stimson and Murray formation is not exposed at this location, but is inferred to subcrop at a relatively shallow depth beneath the plateau (Watkins *et al.*, 2016).

The main Williams outcrop exhibits six cross-bed sets with maximum thicknesses varying between 0.2 m and 0.9 m (Fig. 16). Cross-laminations within these sets dip on average to the north-east. At the base of the outcrop, the lowermost set (Set 0) (Fig. 16) consists of millimetre-scale repetitive cross-laminations that are truncated at their apex by a sub-horizontal bounding surface WOS3.1 that can be traced across the outcrop. Set 0 is overlain by Set 1 which is characterized by sweeping asymptotic laminations that downlap onto surface 3.1. The set shows marked variation in thickness (0.19 to 0.33 m), which is attributed to undulations of the overlying dune migration surface bounding the set. Within the set, cross-laminations have an apparent low angle inclination, when compared with other sets.

Coset 2 is a composite set consisting of one main set (left side of coset) and several smaller discontinuous sets (on the right of the outcrop). These small discontinuous sets may represent the preserved edge of adjacent troughs which cut into the main set. The base of the main set is visible across the outcrop, and is defined by the asymptotic downlap of cross-laminations onto surface 3.2. Surface 3.2 can be traced across the outcrop, with a measured length exceeding 10 m. The upper surface of the coset is defined by the laterally continuous surface 3.3, which can also be traced across the outcrop. Cross-laminations in this set have measured lengths in excess of 2 m in the centre of the set, and on closer inspection have a uniform thickness across their length, with no measurable variation in thickness (Fig. 7). Slight variations in cementation between laminations are discernible, which causes alternating prominent and recessed laminations. Numerous intraset surfaces are present within this set, with maximum dips of *ca* 10°. The overall thickness of Coset 2 ranges between 0.8 m and 0.87 m, with the overall thickness increasing towards the left of the outcrop, to the north-east. Internally, bounding surfaces 3.2.1 and 3.2.2 can be traced laterally for 2.5 m and 1.7 m, respectively. These surfaces appear to cut in and out of the exposed

section of the outcrop, giving them a discontinuous appearance.

The base of Set 3 is occluded by regolith across part of the outcrop; however, surface 3.3 can be delineated by the angular discordance of cross-laminations above and below it. The upper surface of Set 3 is defined by the angular discordance between cross-laminations in Set 3 and Set 4 which defines surface 3.4. The thickness of this set ranges between 0.9 m on the right of the outcrop and 0.7 m on the left, indicating that the set thins by 0.2 m over a distance of 4.7 m. Within this set, there are *ca* 10 inclined intraset surfaces, showing arcuate geometries similar to cross-laminations.

Set 4 is defined at its base by a scour surface 3.4. Laminations within this set are distinct in that they are largely sub-horizontal, with little curvature to the laminations. Laminations have measured distances of up to 2.5 m within this set. Set thickness increases to the left of the outcrop, from 0.27 to 0.74 m, indicating a thickness increase of *ca* 0.5 m over a 10 m distance. The upper surface is defined by a subtle angular discordance caused by an apparent change in lamination orientation in the set above.

The highest defined set in the outcrop, Set 5, is characterized by a discontinuous upper bounding surface, where the outcrop had degraded. Surface 3.5.1, which demarcates the upper left side of the set dips towards the north-east, in the same direction that the laminations dip. The maximum thickness in this set is 0.55 m, where the upper bounding surface is visible.

Using a DOM, dip azimuths from 347 measurements at this location show a dominant palaeotransport direction between 040° and 050° ('All cross-laminations', Fig. 17). The dip and strike measurements were divided into sets described above to ascertain variability up the section. Set 0 shows dip values from 27° at the top of the set to 6° at the bottom of the set and a dominant palaeotransport direction of 070° to 080°. Dip values in Set 1 vary from 20° to 3°, with a dip direction towards 110° to 120°. The majority of palaeotransport readings were taken in Coset 2 (*n* = 141), and the asymptotic geometry was reflected in dip values of up to 30° (purple disks in Fig. 17) at the top of the set, and decreasing to 10° to 12° in the middle, with minimum values of 4° at the base (Fig. 17A). The dip azimuths agreed with the overall values measured, dominantly towards

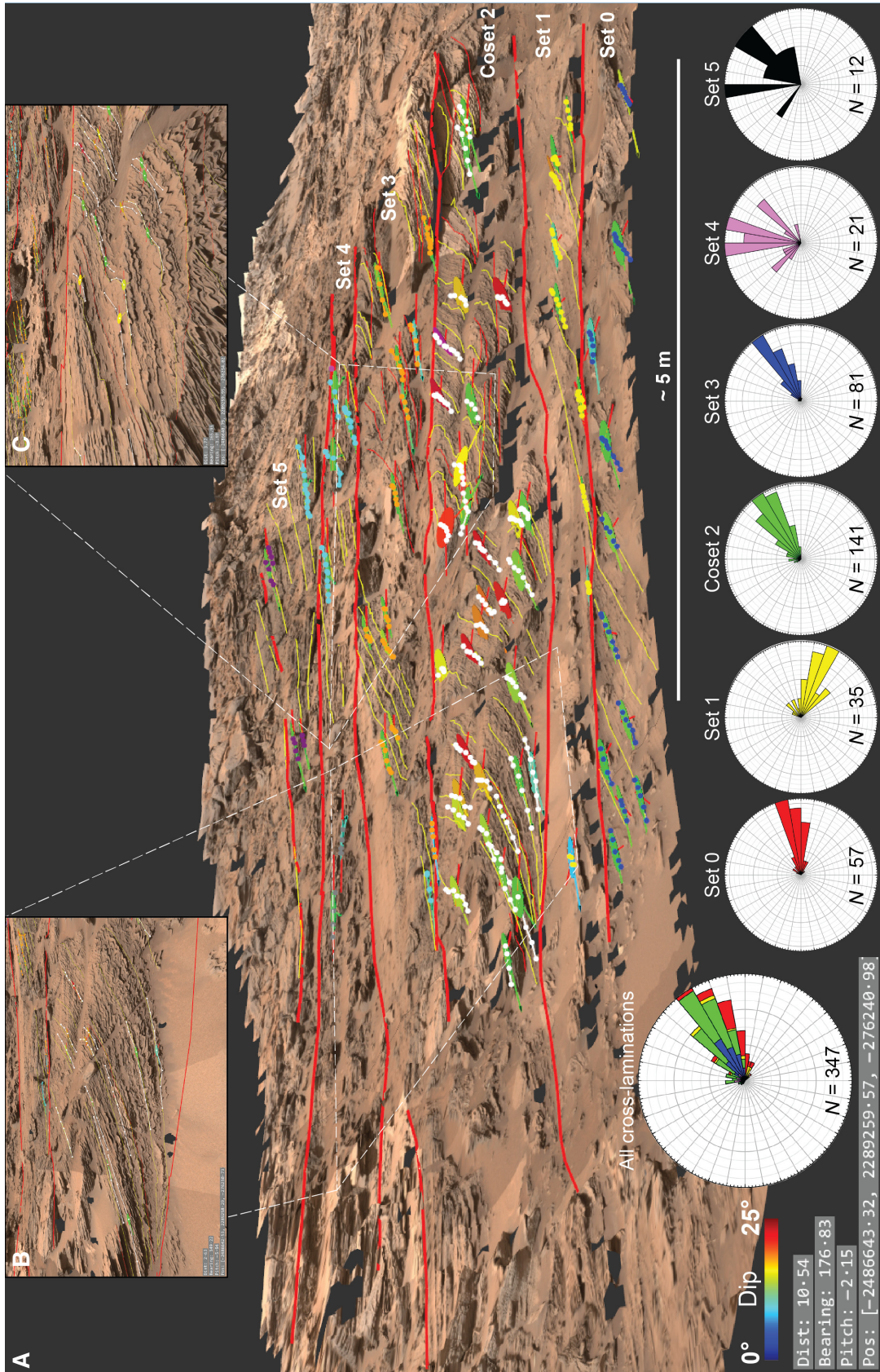


Fig. 17. Interpretation of Williams outcrop using Pro3D software. (A) Williams outcrop rendered and interpreted in 3D. Bounding surfaces and sets mirror those interpreted in Fig. 14. Bounding surfaces are interpreted in white, with laminations interpreted in yellow. Red discs represent plane of best-fit interpolated on cross-laminations, which give dip-azimuth and palaeotransport direction. (B) Close-up view of cross-set. For details, see Fig. 6. (C) Detailed view of bounding surface, and the difference in dip azimuth of cross-laminations above and below the bounding surface. Rose diagrams: The general trend of cross-lamination dip azimuths follow the regional trend towards the north-east. When grouped by set, dip azimuths show a significant divergence from the regional trend.

050° to 060°. A small amount of northerly dipping laminations were recorded in the discontinuous sets in the western part of the outcrop (Fig. 17C). Set 3 also showed a dominant palaeotransport to 050° to 060°, with less scatter apparent (Set 3 in Figs 16 or 17). The DOM quality deteriorates above Set 3, so fewer dip and strike values were taken from Sets 4 and 5 (21 and 12, respectively, Fig. 17). Comparable dominant palaeotransport directions were recorded in Sets 4 and 5, with Set 4 showing a dominance to the north, between 350° and 020°, and minor peaks towards 310° and 050°. Set 5 showed peaks towards the north (350° to 000°) and north-east (040° to 060°). Both sets also had lower maximum dips of laminations (14°). Bed set boundaries dip between 2° and 14° striking towards 062° ($n = 15$). Measurements made using the DOM can be found in Data S8.

Interpretation

Cross-sets and their underlying bounding surfaces are interpreted to represent the preserved basal section of migrating aeolian dunes, which were truncated and buried by successive migrating aeolian dunes during episodes of net sediment accumulation. Coset 2, which is cross-cut by an adjacent set out of the plane of the outcrop can be interpreted as a cross-bed trough, and is interpreted to have formed as a result of the migration of a sinuous-crested out of phase transverse dune. Some dune migration surfaces downcut in the same direction as foreset dip (i.e. WOS 3.4), which may represent fluctuations in scour depth arising from a change in dune shape or an episode where the wind became undersaturated with sediment, resulting in entrainment of previously accumulated sediment. Intra-set surfaces observed within cross-sets at this outcrop correspond to reactivation (third-order) surfaces.

Cross-bed dip data derived from the DOM show that the dominant transport direction of the Williams outcrop was similar to the regional transport direction, towards the north-east. Where dip-azimuth measurements are grouped by set, variability of these vector means are spread across an arc of *ca* 95°; however the two largest sets show a dominant transport direction broadly towards the regional transport direction. These variations could have arisen from autogenic processes, where dune migration direction was altered by turbulent flow around adjacent bedforms (see (Kocurek & Ewing, 2017) or

changes in sediment availability (Courrech du Pont *et al.*, 2014), or by allogenic processes during which the regional wind regime shifts as a result of seasonal or longer-term climate cycles (Hunter & Rubin, 1983; Mountney, 2006).

Large-scale depositional patterns: Bridger Basin

Description

The large-scale sedimentary architecture of the Stimson formation is best exposed at the Bridger Basin outcrop, a natural amphitheatre located on the south-west side of the Bob Marshall Ridge (Figs 2 and 18, and context map in Data S4). Here, the inter-relation of bounding surfaces and set geometries is exposed in a *ca* 4 m high, south-east-facing escarpment that demarcates the north-western side of the basin. The outcrop extends for 90 m, and trends 060° to 240° with an average slope 14° towards the south-east. The outcrop and the adjacent basin floor are composed of cross-bedded Stimson sandstones; however a small inlier of Murray formation occurs at the open end of the amphitheatre at its south-western edge. The exact contact between the Stimson and the Murray is occluded by regolith at this location; however the contact appears to be undulatory because the Stimson is inferred to onlap onto the contact beneath this cover.

The unconformity was observed in the west of Bridger Basin, and can be traced from the western edge of the outcrop south towards the East Glacier outcrop (Fig. 2). The elevation of the unconformity at the west edge of the Bridger Basin outcrop is -4438 m. At the tallest part of the escarpment (Fig. 18), the Stimson section comprises *ca* 12 cosets of sub-metre-scale planar cross-bedding, in which the cross-laminations dip towards the north-east. Planar sets are defined by bounding surfaces that are largely sub-parallel and sub-horizontal to one another, and can be traced across the outcrop for distances in excess of 30 m. Locally, they show relief of several tens of centimetres resulting in variable set thicknesses along the outcrop. Maximum set thicknesses are typically between 0.3 m and 0.7 m. Some bounding surfaces are truncated by overlying downcutting bounding surfaces.

Sets at Bridger Basin vary in thickness greatly across the outcrop, in some places exhibiting complex relationships (Fig. 18B). The lowermost sets, 1 and 2, show a pinching out relationship, where Set 1 increases in thickness in the direction of foreset dip to a maximum thickness of

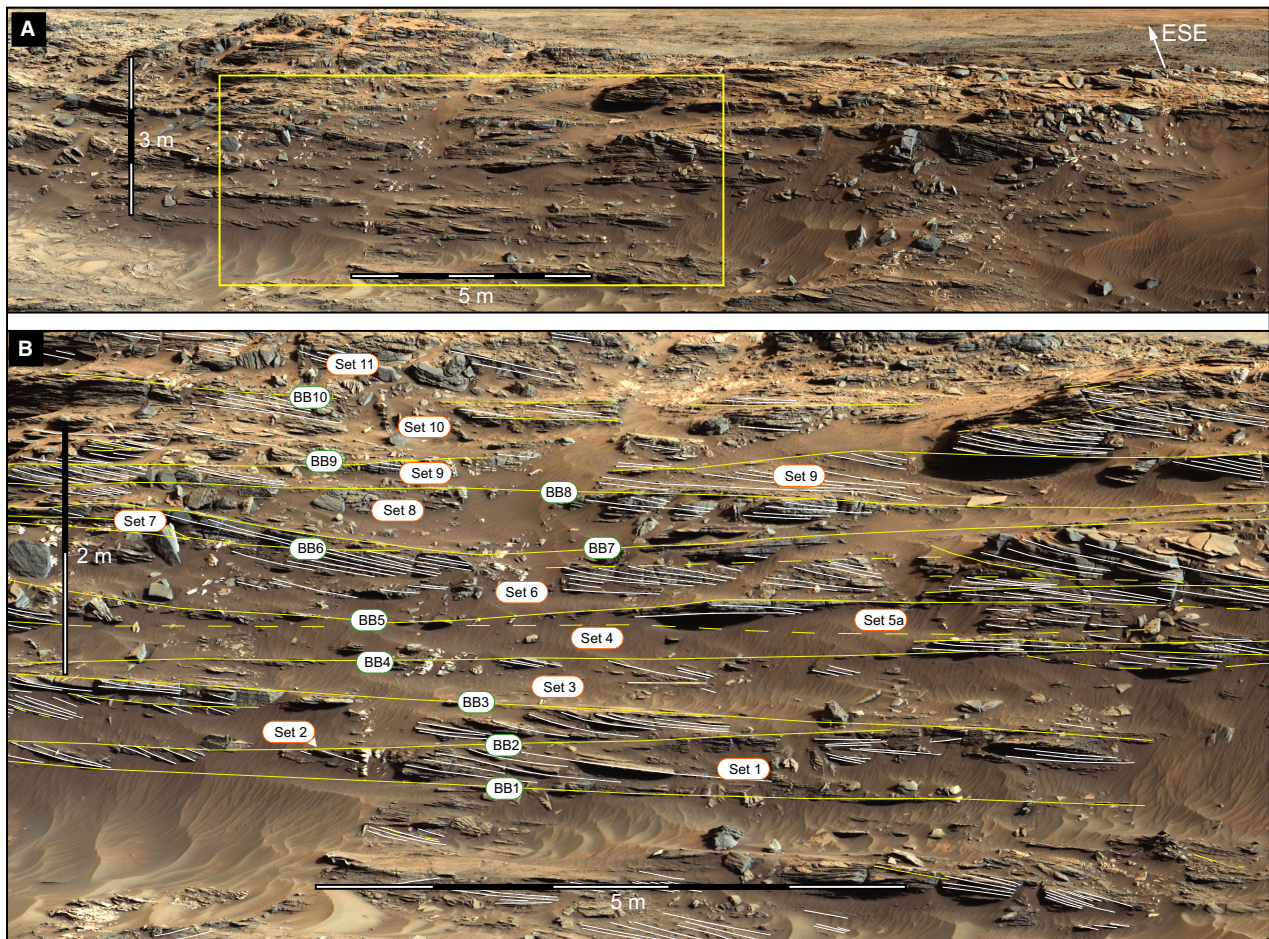


Fig. 18. Bridger Basin area. (A) Uninterpreted overview of Bridger Basin outcrop, situated on the south side of the ridge where the Williams outcrop is located. The outcrop is *ca* 4 m high, and the wall is *ca* 90 m long. (B) Interpreted close-up of Bridger Basin architecture. Large-scale architecture is exposed across the outcrop, and dune migration surfaces were traced for more than 30 m, where they are not truncated by overlying surfaces. Cross-laminations dip predominantly towards the right of the outcrop, towards the north-east. Mastcam-100 mosaic mcam04872 was taken on Sol 1100 from the Sol 1099 end-of-drive position. Image credit: NASA/JPL-Caltech/MSSS.

0.4 m, having been partially truncated by surface BB2 and overlain by Set 2. Set 2 also pinches out in the direction of foreset dip, where it is truncated by surface BB3, which is the lower bounding surface for Sets 3 and 4. A similar pinching out relationship was observed in Sets 3 and 4. Bounding surface BB5 also shows relief, and downcuts the entire thickness of Set 5 by *ca* 0.4 m, scouring into the top of Set 4 over a distance of 4 m. The surface then rises to the north-west, bounding the top of Set 5a. Set 6 thickens gradually from left to right of the outcrop, from a thickness of 0.3 to 0.64 m. Surfaces BB5 and BB6 which bound Set 6 are relatively parallel, but diverge towards the north-east over a distance of 20 m. Surface BB7 completely cuts out Set 7, truncating surface BB6 and the top of Set 6, and

downcutting *ca* 20 to 30 cm. This scour is infilled by Set 8, which exhibits a lens shape, thickening to 0.4 m in the centre of the depression, then thinning in the direction of foreset dip. Set 9 has a uniform thickness of <0.2 m for 7 m laterally, before thickening towards the right of the outcrop, to a maximum thickness of 0.3 m. The upper surface of Set 10 is poorly defined, and has limited stereo coverage, preventing accurate measurements of thickness. Across the outcrop, several intraset surfaces were identified with prominent examples in Set 6.

Interpretation

The outcrop is composed of stacked cross-bed sets and is interpreted to record accumulation of sediment by migration of aeolian dunes along the

axis of dominant sediment transport. Set thickness in this outcrop is variable, particularly within a single set. Dune migration surfaces undulate along their length where they can pinch-out or downcut into certain sets (surfaces BB5 and BB7) or climb, resulting in a downwind increase of set thickness (BB2 and Set 1, BB5 and Set 5a, BB7 and Set 6). These variations in set thickness may have been caused by autogenic processes related to internal processes within the dune field, by allogenic controls representing a regional change in processes affecting the dune field, or a combination of both factors. One cause of these thickness variations could arise internally to the dune field from the complex interrelation of migrating scour pits and spurs in sinuous-crested transverse dunes. As scour pits migrate

along their dominant transport vector, they can shift laterally, resulting in spatial variations of scouring, causing these variations of set thickness. Alternatively, this may have been controlled by variations in sediment flux, where the wind temporarily became sediment undersaturated, allowing entrainment of previously accumulated sediment, resulting in temporary downcutting of the dune migration surface. The horizontal bounding surfaces identified are unlikely to represent water-table controlled deflation surfaces, as described by Kocurek & Day (2017) or supersurfaces (Rodriguez-Lopez *et al.*, 2013), because the surfaces undulate by several tens of centimetres over a distance a few decametres and microtopography associated with cohesion on that surface has not been observed. It is more likely that these

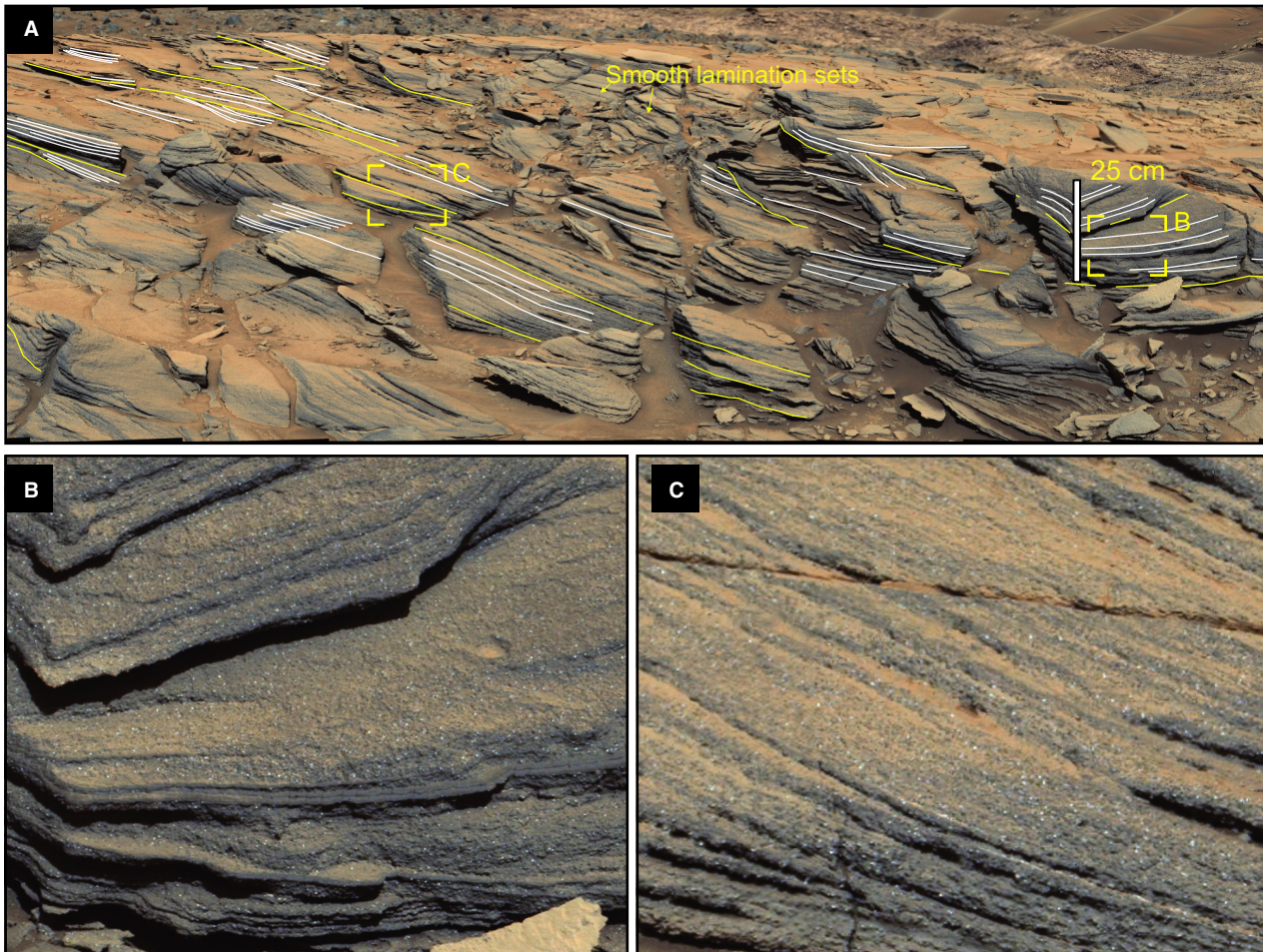


Fig. 19. McLeod outcrop (A) Overview of McLeod outcrop, which is composed of a single cross-bed set. Yellow lines denote inclined intraset surfaces within the set. (B) Close-up of smooth laminations interstratified with 'rough laminations'. (C) Close-up of laminations within the set. Note that 2 mm diameter grains are resolvable. Mastcam-100 mosaic mcam05194 of McLeod outcrop was taken on Sol 1148, from Sol 1144 end-of-drive position. Image credit: NASA/JPL-Caltech/MSSS.

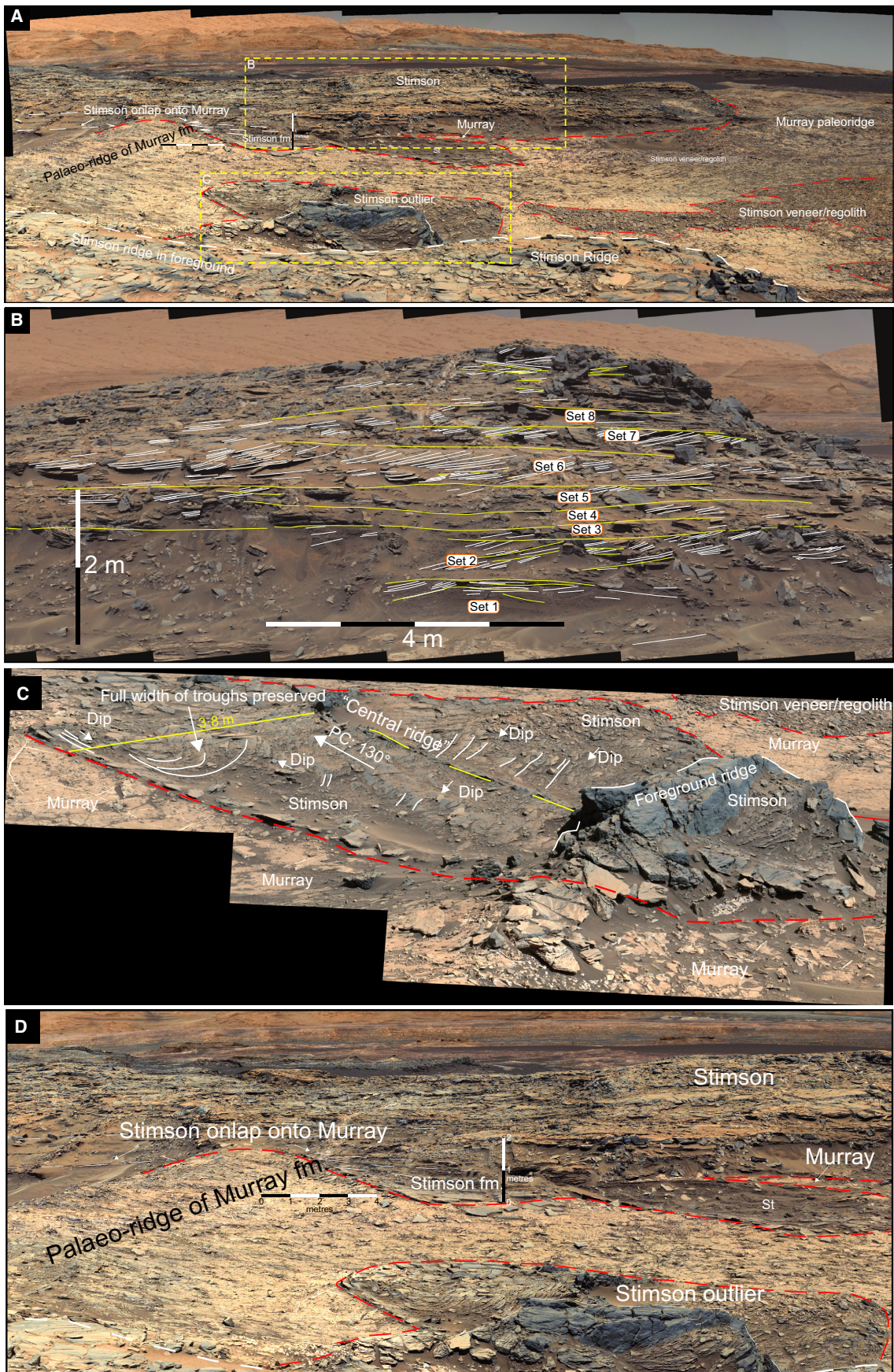


Fig. 20. East Glacier area and key stratigraphic observations at this location. (A) Mastcam mosaic showing overview of East Glacier area and demonstrating the relationship of key locations at the outcrop. Mastcam-34 mcam05216. (B) East Glacier main outcrop. Architecture at this location is representative of the Stimson formation, with dune migration surfaces (first-order surfaces) clearly identifiable (yellow) Cross-laminations dip predominantly towards the left of the outcrop, which is towards the north-east. Mastcam-100 mcam05219. (C) East Glacier outlier. Outcrop consists of two trough cross-bed sets exposed in plan-view, surrounded by Murray formation. Palaeotransport direction is towards the south-east, which is at a tangent to the regional transport direction. Mastcam-100 mcam05214. (D) Detailed view of the Stimson formation onlapping onto a palaeotopographic surface expressed in the upper surface of the Murray formation. Mastcam-34 mcam05216. Image credit: NASA/JPL-Caltech/MSSS.

surface undulations are associated with autogenic processes within the dune field, such as variations of sediment supply within the dune field, or interaction between dunes.

Detailed internal geometry of a Stimson cross-bed set: McLeod outcrop

Description

The McLeod outcrop allowed for close-range imaging of Stimson sandstone with Mastcam, capturing subtle facies variations normally only seen in MAHLI images. The outcrop (Figs 2 and 19) is a cross-bedded sandstone which forms a small, 1 m high ridge. The close proximity (<6 m) of the rover to the outcrop resulted in images with sub-millimetre resolution, capturing grain-scale texture preserved within the outcrop. The McLeod outcrop is a single *ca* 1 m thick set of metre-scale cross-bedded sandstone. It exhibits a rough speckled surface texture, caused by the presence of white, 1 to 2 mm diameter grains that represent 2 to 5% of grains present (Fig 19B and C). The remainder of the sandstone consists of grey coloured grains expressed as a rough surface texture; although grain boundaries cannot be resolved due to a lack of contrast between grains. Cross-laminations in the outcrop are largely planar, lack curvature and exhibit uniform thicknesses of a few millimetres (3 to 7 mm; Fig. 19B and C). Laminations dip to the south-east and have lengths of up to 1 m. Horizontal bounding surfaces have not been identified at this outcrop. Intrasets bounding surfaces which truncate cross-laminations at a shallow angle are common, and typically dip in a similar direction to the cross-laminations. Dip directions above and below these intrasets demonstrate discordances of a few degrees. A single partially preserved *ca* 2 m wide trough cross-set is observed to cut obliquely across the underlying set at the top of the outcrop, and is

composed of laminations that dip approximately north (Fig. 19). Locally several interstratified bed sets characterized by a smooth surface texture and lacking resolvable grains were observed.

Interpretation

The McLeod outcrop exhibits a similar texture to that observed at the MAHLI target Lumprey (Fig. 7) at the Missoula outcrop at Marias Pass. In both locations, cross-bedded sandstones contained very coarse to granule size grains interspersed in an apparent fine to medium-grained sandstone matrix. The origin of the larger white grains is uncertain, but they are likely to have been moved by aeolian surface creep, caused by grain collisions. The abundance of intra-set surfaces within this set suggests either the superimposition of smaller bedforms migrating across the lee slope of a larger dune, variations in wind direction and strength, or the merger of two dunes. The oblique trough at the top of the outcrop suggests either a brief episode during which sediment transport was discordant to the main transport direction, or that the trough was created by a subordinate bedform migrating across the lee of a larger bedform. Laminations with smooth surface textures are interpreted as possible grainfall strata, in which finer grains capable of saltation were segregated and concentrated away from coarser particles moved by creep.

Depositional patterns related to complex palaeotopography: East Glacier outcrop

Description

To further understand the relationship of the Stimson formation to the underlying Murray formation, these stratigraphic relationships were observed in detail at the East Glacier outcrop located 100 m south of Bridger basin (Figs 2 and 20, and the context map in Data S4). Here, excellent exposures of the

Stimson and underlying Murray formation, together with the unconformity separating the two, enable investigation of the stratigraphic relationship between the two formations at a decimetre-scale and reconstruction of the palaeotopography at the unconformity. The East Glacier area forms a *ca* 30 m wide alcove oriented approximately east–west that exposes Murray formation mudstones at its core. Stimson formation sandstones form the topographic boundaries of the depression.

Sub-Stimson unconformity

At the base of the amphitheatre, the upper modern surface of bedrock of the Murray formation forms a series of ridges 0.6 to 1.3 m high, that trend north-east/south-west, and are spaced *ca* 15 m apart. These ridges can be traced to the southern side of the amphitheatre where they are unconformably overlain by a 6.5 m thick section of Stimson formation. On the south side of the amphitheatre (Fig. 20), Stimson sandstones onlap onto both sides of a small 1.3 m high ridge formed of Murray formation mudstones. Sub-horizontal bounding surfaces within the Stimson truncate against the ridge on both sides. Sets defined by these bounding surfaces appear to thin as they onlap onto the unconformity. This ridge is completely overlapped and buried by Stimson sandstone. Two smaller ridges west of this ridge (Fig. 20) show similar relationships with the overlying Stimson. These ridges have heights of *ca* 0.6 m, and the Stimson infills the lows between these ridges and onlaps and thins onto their flanks. The undulatory character of the unconformity surface and the onlap of Stimson sandstones onto this surface indicates that the unconformity shows metre-scale palaeotopography. The palaeotopographic ridges have a relief of *ca* 1 m in amplitude, with a wavelength of *ca* 15 m between the individual ridges (Fig. 20D). The axes of the palaeo-ridges are aligned approximately NNW–SSE and can be traced for *ca* 30 m along their axis before they are occluded by regolith or the overlying Stimson formation. Within the palaeotopographic lows, cross-bed troughs show axes aligned parallel to the ridge crests. Above the crest of the ridges, cross-bed sets dip towards the north-east. Stimson sandstones in the lows between the Murray ridges contain abundant concretions, showing a rough bulbous surface texture. Here, the Stimson is densely packed with concretions to the point where they are commonly amalgamated. The concentration of concretions

decreases with increasing stratigraphic height above the tops of the palaeo-highs, becoming more isolated and sporadic in their distribution towards the top of the outcrop.

Stimson outlier

At the northern edge of the amphitheatre, an outlier of Stimson eroded into Murray formation bedrock is present in a topographic low (Fig. 20C). Within the outlier, two trough cross-sets in planform section were observed, with the eastern set truncating the western set. These sets are eroded into Murray formation bedrock. The eastern set has a width of 3.5 m, while the partially truncated western set has a width of 4.2 m. In both sets, uniform millimetre-thick laminations define inclined troughs that dip towards the south-east. The fully preserved eastern trough allowed complete measurement of the foreset dip direction, which is towards 130°.

East Glacier main outcrop architecture

Above the unconformity, the Stimson at this location comprises repeated sets of sub-metre-scale cross-bedded sandstones, with eight sets observed at the tallest part of the outcrop (Fig. 20B). Individual sets are broadly uniform in thickness along their length, however Sets 5, 6 and 7 pinch out towards the north-east. The thickest set (Set 6) is *ca* 0.7 m thick, while other sets are thinner, with some measuring *ca* 0.5 m in thickness. Within sets, cross-laminations dip predominantly to the north-east above the level of unconformity relief. Horizontal bounding surfaces separating the sets are largely sub-parallel and sub-horizontal, and undulate by a few centimetres, leading to little variation in set thickness. Intra-set surfaces are common in Sets 2 to 8, mirroring the dips of the cross-laminations, but typically with shallower dip angles.

East Glacier area interpretation

Onlap relationships along the undulating sub-Stimson unconformity at this location indicate that the unconformity represents a relict palaeotopographic surface. The origin of the palaeo-ridges at the unconformity is uncertain, but could have been a consequence of aeolian deflation of Murray bedrock before deposition of the Stimson. The absence of gravel lags or fluvial deposits above the unconformity suggests that fluvial processes did not create this palaeotopography. The Stimson formation at this location shows comparable set sizes and set characteristics (cross-lamination thickness, uniformity and

geometry) to the outcrops at Williams, Bridger Basin and McLeod, suggesting deposition by migrating dunes. The concretions that are concentrated near the base of the outcrop, particularly in palaeotopographic lows, are interpreted to be post-depositional diagenetic features. The mechanism to explain their origin and distribution is uncertain; one possibility is that their formation represents the presence of a perched aquifer at the base of the Stimson, or an increased concentration of minerals which acted as a nucleus for concretion growth (Berner, 1968).

Observations show that palaeotopography exerted a control on the transport direction of the aeolian dunes recorded by the Stimson formation. Below the uppermost level of the unconformity, cross-sets are aligned broadly parallel to the palaeo-ridges at the unconformity – towards the south-east – whereas above this level cross-sets are aligned with the regional transport direction – towards the north-east. This suggests that palaeotopography influenced local transport direction by modification of the wind regime. Once sufficient Stimson accumulated to bury the palaeotopography, it no longer modified the local wind regime and dune migration reverted to that of the dominant regional transport trend.

Pattern of dune migration and palaeowind flow

Observations

Aeolian dune cross-strata provide the most direct record of patterns of dune migration and the palaeowind regime. The orientation of cross-strata as measured by their dip and plunge-azimuth provide information about the local and regional pattern of dune migration direction, and have been used to infer the wind regime at time of deposition. The average dip direction of cross-strata within a set indicates the overall dune migration direction. Palaeotransport direction was determined using a visual estimation method on outcrops of the Stimson formation across the study area (Fig. 4), and in more detail at specific outcrops where high-quality stereo image data permitted construction of DOMs from which cross-bed dip azimuths could be accurately measured. The visually estimated palaeocurrent measurements are provided as a shapefile and as a high-resolution map in Data S2 and S9.

Visual estimation of 117 cross-strata dip azimuths across the study area showed a dominantly unimodal dip azimuth, and hence general dune migration direction, towards the

north-east in present-day geographic coordinates (Fig. 21). Trigonometric calculation of vector mean and vector magnitude from these results indicates a vector mean of 052° , with a vector magnitude of 0.65 (using the method described by Lindholm, 1987). Although the dominant transport direction was towards the north-east, cross-sets commonly show deviation from this general transport direction at a local level. At Marias Pass, cross-set dip azimuths at the base of Apikuni Mountain (Fig. 21A) show deviation of up to 70° from the dominant transport direction, with small decimetre-scale sets dipping towards the south-east. On the plateau between Marias Pass and Williams outcrop, cross-bed dip azimuths show a general trend towards the north-east, although a broad range of dip azimuths with a spread of almost 180° were observed (Fig. 21B), with three examples of decimetre-scale cross-sets showing dip azimuths either to the south-east or north-west. If these sets are excluded from the dataset, the range of dip azimuths are spread across a 70° arc. Visual estimation of palaeocurrents at Williams is in agreement with DOM-derived data, with the general transport direction towards the north-east (stereo derived vector mean: 067° ; Fig. 16). Observations at the Bridger Basin outcrop were limited due to the distance from which the outcrop was observed; however measurements of sets show a north-easterly dip azimuth, with a spread of *ca* 20° (Fig. 21C).

The outcrop at East Glacier shows broad variation in cross-bed dip directions within the study area. In the lowermost parts of the succession, both within the Stimson outlier and the lower parts of the main outcrop, foreset dips are aligned along palaeotopographic lows at the sub-Stimson unconformity (Figs 20C and 21C) and show dips towards the south-east. Slightly higher up in the stratigraphy exposed at the main outcrop (Fig. 20B), several cross-sets show dip azimuths towards the south-west – the opposite direction to the north-east dominant transport direction.

Interpretation

Palaeotransport analysis based on measurements of dip azimuths from sets of cross-strata using a visual estimation method, together with analysis of cross-strata in selected stereo-reconstructed outcrops indicate that the general direction of dune migration was towards the north-east. The average dip direction of cross-strata however does not necessarily reflect the average wind

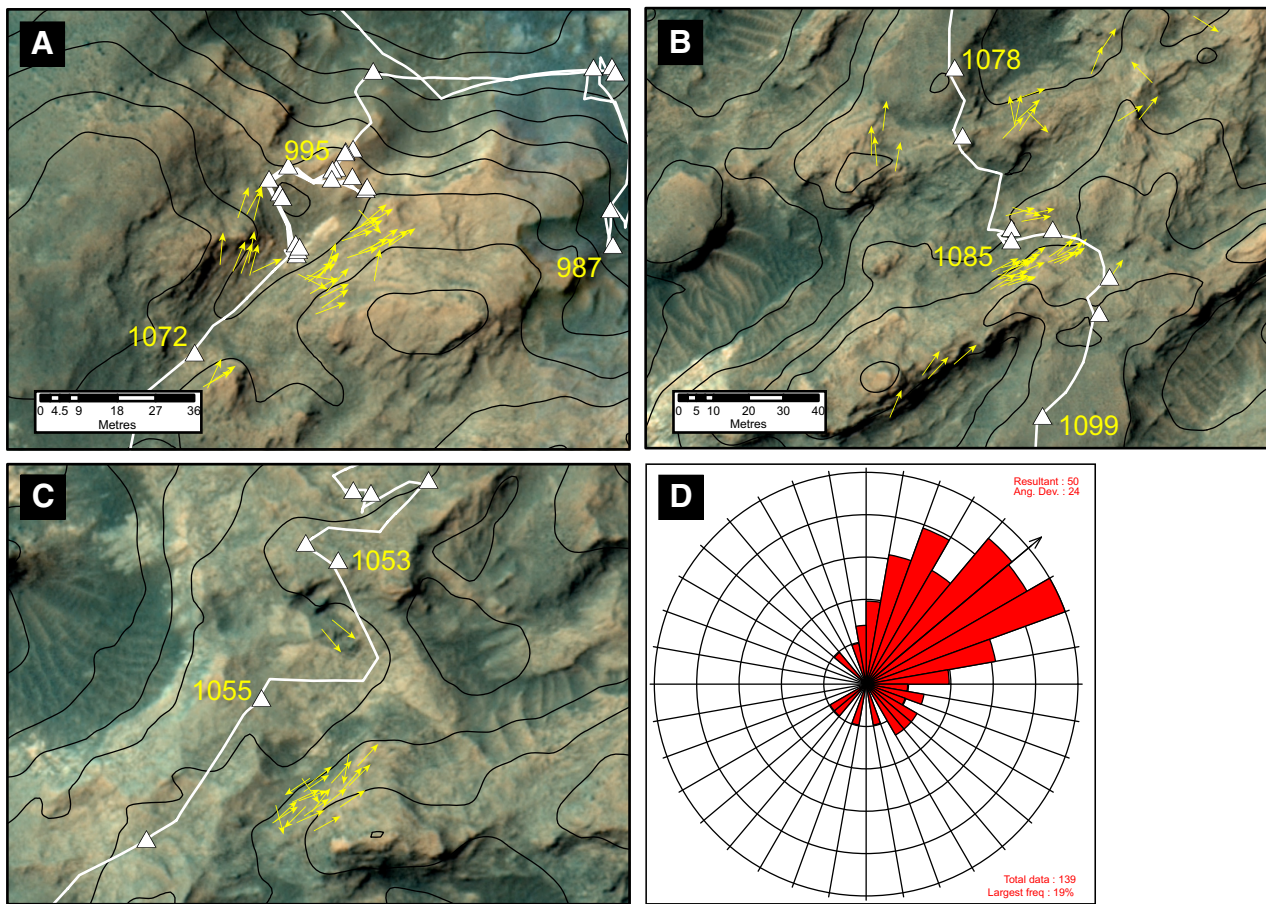


Fig. 21. Maps showing cross-strata dip directions as determined by visual inspection of cross-stratified units in Navcam and Mastcam mosaics. Foreset dip azimuths indicate general sediment transport direction within the Stimson formation. (A) Palaeotransport directions observed in the Marias Pass area. (B) Palaeotransport directions observed at Williams and Bridger Basin. (C) Palaeotransport directions observed at East Glacier. (D) Rose diagram depicting dominant transport direction within the Stimson formation, across the study area ($n = 139$). The vector mean is towards 052° , with a vector magnitude of 0.65. Image credit: NASA/JPL/University of Arizona.

direction. Wind direction can only be loosely inferred, because bimodal or polymodal wind regimes can generate bedforms with crests oblique to both the prevailing wind direction, and the resultant transport direction (Rubin & Hunter, 1987; Rubin & Ikeda, 1990; Eastwood *et al.*, 2012). Thus dunes could be migrating obliquely in response to two different wind directions. Although *Curiosity's* traverse provided only a limited view of the entire Stimson sand body, the presence of more than one wind acting on the dunes is supported by the abundance of wind-ripple stratification and reactivation surfaces. These occur where the angle between the instantaneous wind direction and the local crestline orientation is oblique to longitudinal (Sweet & Kocurek, 1990; Eastwood *et al.*, 2012). Additionally, the absence of grainflow

stratification in Stimson cross-sets indicates that, at least in the areas of the Stimson surveyed, crestline transverse flows were not frequent. Although the wind regime at the time of Stimson deposition remains difficult to reconstruct, it can be inferred that the wind regime drove dune migration, and hence net sediment transport, from the south-west to the north-east. The absence of any evidence for large-scale horizontal and vertical deformation of the Stimson formation outcrops (except for fractures) indicates that the dip directions have not been altered by post-depositional displacement of the outcrops.

Secondary wind currents are the inferred cause of strata with dip directions deviating significantly from the general transport direction. Spurs and defects are crestline elements that deviate from dominant crestline trend and may

be nearly orthogonal to the dominant crestline trend (Kocurek *et al.*, 2010; Swanson *et al.*, 2018). Migration of these elements can produce cross-stratification that deviates from the overall trend (Brothers *et al.*, 2017). The presence of pre-existing large bedforms can modify the local wind field, creating eddy currents that generate subordinate bedforms travelling obliquely to the general transport direction (Rubin & Hunter, 1982; Kocurek, 1991; Rubin & Carter, 2006). Cross-sets in palaeotopographic lows on the sub-Stimson unconformity were observed with cross-lamination dip azimuths oblique to the general transport direction. This divergence is inferred to arise as a result of interaction between the wind and the palaeotopography, which modifies the local wind field, and the resulting bedform migration direction.

DISCUSSION

Evidence for aeolian deposition of the Stimson sandstone

Taken together, the grain-scale texture, sedimentary structures and facies presented by the Stimson formation sandstone lead to its interpretation as an ancient aeolian sand deposit. This section focuses on the sedimentary texture and the facies as the primary evidence for this aeolian interpretation.

Grain-scale texture observed in MAHLI images indicates that the Stimson sandstone has a bimodal grain-size distribution and well-rounded grains (Fig. 6; Data S4). These are common attributes of wind-sorted sediments on Earth (Sharp, 1963; Ellwood *et al.*, 1975; Yizhaq & Katra, 2015). This study demonstrates that the geometric mean grain size for the Stimson formation is 406 μm (long-axis measurements). This is compared to grain sizes measured in the Bagnold dune field which were 120 μm (modal) (Ehlmann *et al.*, 2017), ca 112 μm (modal) (Sullivan & Kok, 2017) and 113 μm (intermediate axis) or 135 μm (long axis) (Ewing *et al.*, 2017). As a comparison, the grain size of aeolian systems on Earth typically range between 150 μm and 300 μm (Bagnold, 1941), with example mean grain sizes of: 156 μm for White Sands National Monument; 243 μm for the Page Sandstone, Arizona; 285 μm for Great Sand Dunes New Mexico, USA; and in extreme cases, 660 μm observed on seif dunes in the Sabha Desert, Libya (Ahlbrandt, 1979). The major modal peak observed for

combined Stimson grain measurements is 285 μm , which probably represents the fraction of grains transported by saltation, with the minor modal peak at ca 850 μm representing grains that were moved predominantly by surface creep. Elsewhere in the Stimson, larger grains of up to 2 mm diameter are relatively common and are visually estimated to comprise 2 to 5% of the sandstone in some locations. Such granule-grade grains are considered too large to have moved by saltation and were probably moved by surface creep. While the major mode of Stimson grains falls within the range of grain sizes typical of saltating particles on Earth, this peak is still approximately twice as coarse as the average grain size of the Bagnold dune field. It is uncertain as to why the Stimson sandstone is much coarser-grained than the modern Bagnold dune sands. One possible reason is that atmospheric conditions during deposition of the Stimson were sufficiently different to allow transport of much coarser grains, although this needs further investigation.

Texturally, larger grains observed in MAHLI images are very well-rounded and have a smooth, sometimes pitted, surface. This is characteristic of repeated grain collisions which cause grain rounding by surface abrasion (Collinson *et al.*, 2006). Fluvial transport of sand grains, even over hundreds to thousands of kilometres, does not cause such grain rounding owing to the difference in transport mechanism (Garzanti *et al.*, 2015; Garzanti, 2017). Aeolian processes are much more effective at rounding particles owing to the greater differential density between grains and air, allowing harder grain–grain impacts, and because sub-aqueous transport provides a cushioning effect owing to adsorbed water films on grain surfaces (Folk, 1980). Moreover, sedimentary textures within the Stimson are very different from those in fluvial deposits identified elsewhere in Gale crater, which are characterized by poorly to moderately sorted sandstones comprised of sub-angular to sub-rounded sand grains (Anderson *et al.*, 2015; Edgar *et al.*, 2017).

The second key feature which leads to an aeolian interpretation for the Stimson formation is the ubiquitous presence of uniform thickness pinstripe laminations which form the cross-laminations in cross-beds. This wind-ripple stratification is generated by the migration of impact ripples, and is a common process observed on Earth (Eastwood *et al.*, 2012) and modern Martian dunes (Bridges *et al.*, 2017; Ewing *et al.*, 2017). Wind ripples form because

grains in airflow have a propensity to be transported by saltation, rather than traction (such as in sub-aqueous flows). Saltating grains falling on the lee slope of a ripple tend to accumulate in the pocket of still air, causing the ripple crest-lines to migrate downwind. As these ripples advance, they bury the stoss slope of the preceding ripple preserving the entire thickness of the ripple and, because of the absence of traction, the stoss side of the ripple is not eroded as happens when sub-aqueous climbing-ripple strata forms. Over time, the advance of a series of ripples will generate translational wind-ripple strata, which are characterized by laminations of uniform thickness (Fryberger & Schenk, 1988). This results in the generation of distinctive pinstripe laminations which are ubiquitous in aeolian strata on Earth, and were observed throughout the Stimson formation.

The Stimson is characterized by cross-bed sets up to a metre in thickness. Generation of sets of such a thickness by fluvial processes implies substantial river channel depths (Leclair & Bridge, 2001). Stimson sets are greater than the typically <10 cm thick cross-sets observed in the fluvial Shaler outcrop, for example (Edgar *et al.*, 2017). Moreover, no palaeochannel-forms marked by down-cutting erosional surfaces, as might be expected in a fluvial succession, have been observed. Instead, sub-horizontal bounding surfaces which show strong similarities to dune migration surfaces observed in aeolian deposits on Earth are present (Brookfield, 1977; Kocurek, 1984, 1991).

Bed sets in the Stimson formation are separated by surfaces identical to those seen in dry aeolian systems on Earth. First, second and third-order surfaces, relating to migration of main dunes, superimposed dunes and reactivation, respectively, have been identified, and are similar to those characteristic of major ancient aeolian deposits on Earth, such as in the Permian Cedar Mesa (Mountney, 2006), the Jurassic Navajo (Hunter & Rubin, 1983), Entrada (Kocurek, 1981a) and Aztec sandstones (Porter, 1987) on the Colorado Plateau. This further supports an aeolian interpretation for the Stimson sandstone.

Reconstructing Stimson sedimentary processes

The dominance of cross-stratified bed sets in the Stimson formation indicates that deposition by migration of aeolian dunes was the primary mode of sedimentation (Hunter, 1977a; Kocurek & Dott, 1981; Rubin & Hunter, 1982; Kocurek,

1991). Analysis of these cross-stratified units permits understanding of sedimentary processes operating on these ancient dunes, in particular through comparison with observations from the modern Bagnold dune field in Gale crater.

The Bagnold dune field is located at the base of the northern flank of Aeolis Mons and was investigated by the MSL science team in the region of the outcrop of the Stimson formation. This modern dune field extends from the north-east to the south-west and comprises barchan and linear dunes as the dominant dune types (Hobbs *et al.*, 2010; Silvestro *et al.*, 2013; Day & Kocurek, 2016; Lapotre *et al.*, 2016, 2017; Ewing *et al.*, 2017). The Namib dune, within the Bagnold dune field, was visited between Sols 1194 and 1247 of the traverse and provided an opportunity to study sedimentary processes on an active barchan dune (Ewing *et al.*, 2017). The results of this study aid understanding of what processes may have occurred on ancient dunes. Observations of the primary lee slope of Namib dune (Fig. 22) identified deposits caused by processes typically observed in terrestrial dunes including: grainflow deposits, grainfall deposits and impact ripples, together with large ripples which have not been observed on dunes on Earth (Lapotre *et al.*, 2016; Ewing *et al.*, 2017). Grainflow deposits indicate accretion on the lee face of dunes during their migration and are a key diagnostic feature of aeolian dunes (Hunter, 1977b; Kocurek & Dott, 1981). On the Namib dune lee face, grainflow deposits are common; however, all but the most recent show various degrees of reworking by impact ripples and large two-dimensional ripples. Grainflow deposits form lobes with an hourglass shape widening and thickening to the base of the lee slope. Some parts of the dune lee face exhibit no evidence of grainflow deposits, suggesting that reworking by ripple migration has completely eradicated their expression. Both impact and large ripples are aligned perpendicular to the crest line of the dune, which suggests that they formed by wind blowing parallel to the lee slope and reworked grainflow and grainfall deposits as they migrated. With this high degree of lee-slope reworking on modern dunes, it is hypothesized that preserved grainflow deposits in the stratigraphic record would be rare.

Foresets in Stimson cross-strata provide important information on dune lee-slope depositional processes and their preservation in the Martian sedimentary record. Cross-laminations are characterized by repeated typically thin (*ca* 4 mm thick) layers, of uniform thickness along

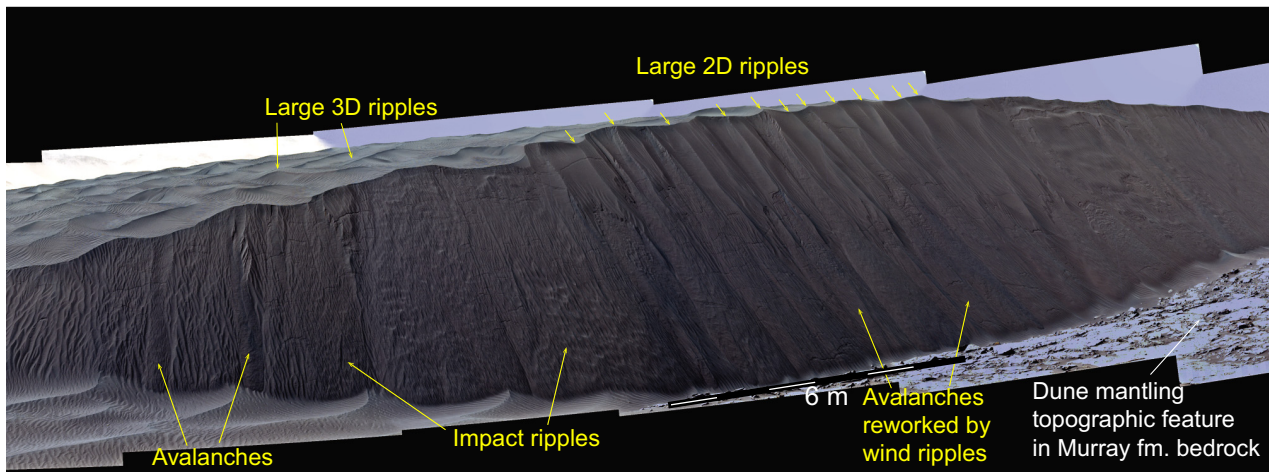


Fig. 22. Namib dune, Bagnold dune field, as an example of processes occurring on a modern dune on Mars. Three orders of bedform can be identified here – impact ripples (centimetre wavelength bedforms), Large 2D and 3D ripples (metre wavelength bedforms), and dune-scale bedforms (hundreds of metre wavelengths). Two-dimensional large ripples are confined to the dune lee slope, whereas 3D ripples are found on the dune stoss-slope, and on interdune sand flats. Impact ripples can be observed on the lee slope of the dune, migrating perpendicular to the lee slope dip azimuth, in the same orientation as the large ripples. Grain avalanches can be observed, demonstrating varying degrees of reworking. Most recent avalanche deposits have little or no reworking by wind-ripple strata, whereas the oldest discernible avalanche deposits are completely overprinted by wind-ripple strata, or are eradicated by migrating ripples. Mastcam-34 mosaic mcam05450 was taken on Sol 1196, from Sol 1194 end-of-drive position. A 360 mosaic taken at the dune is available at <https://mars.nasa.gov/resources/7627/>. Additional material for the dune field is listed in the Supporting Information. Image credit: NASA/JPL-Caltech/MSSS.

the length of the cross-laminae, which are generally parallel to adjacent laminations throughout a given set. Downward pinching wedges comprising grainflow beds that delineate avalanche strata (Hunter, 1977a; Kocurek & Dott, 1981) are notably absent or have not been identified along the traverse.

Three possible explanations could account for this absence. Firstly, the distinctive uniform thickness cross-laminations may represent pin-stripe laminations formed by reworking of the lee slope by wind ripples migrating across the lee slope, producing wind-ripple strata (Hunter, 1977a; Fryberger & Schenk, 1988; Kocurek, 1991; Eastwood *et al.*, 2012). These wind-ripple strata become buried by subsequent avalanche or grainfall deposits as the dune migrates in the dominant wind direction, which in turn become reworked by wind ripples migrating obliquely across the lee face. This is similar to observations on the Namib dune lee slope, or modern terrestrial dunes at White Sands dune field, where impact ripples migrate across dune lee slopes (Eastwood *et al.*, 2012). Aeolian strata on Earth also commonly show reworking of avalanche strata by wind ripples (Kocurek & Dott, 1981) or show a high proportion of wind-ripple strata compared

to grainflow or grainfall strata. The Permian Auk Formation (Central North Sea), for example, contains up to 85% wind-ripple strata in discrete stratigraphic intervals (Romain, 2014), indicating that reworking of dune lee slopes by wind-ripple strata is pervasive.

The second possibility is that the dominant transport direction is at a high incidence angle to the dune crests. Where this is the case, wind-ripple strata are limited to the lower parts of the lee slope, while grainfall and grainflow strata dominate the upper slope (*sensu* Eastwood *et al.*, 2012). The sedimentary architecture of the Stimson formation demonstrates that dunes were climbing at a sub-critical angle, with only the basal section of the dunes being preserved. If avalanche strata were restricted to the upper part of the dune, as described by Eastwood *et al.* (2012), their presence would largely be lost to scour during dune migration.

A third explanation comes from the identification of a new intermediate class of bedforms on Mars that are not observed on Earth (Lapotre *et al.*, 2016; Ewing *et al.*, 2017). These studies showed the presence of large ripples with 2D crests superimposed on the Namib dune lee face. In addition to impact ripples, these large ripples are progressively reworking recent grainflow and

avalanche deposits. One possible interpretation for the uniform thickness cross-laminations present in Stimson cross-sets is that they were formed by reworking of the lee face by migration of 2D large ripples. The key to whether the uniform thickness laminations were generated by impact ripples or large wind-drag ripples may lie in their thickness and continuity: individual laminations are typically *ca* 4 mm thick and can typically be traced from the toe to the apex of sets. The thickness of individual wind-ripple laminations observed on Earth range between a few grains thickness to a few millimetres in thickness (Fryberger & Schenk, 1988), which does not preclude wind ripples generating these laminations in the Stimson formation. It is likely that if large wind-drag ripples developed a slight amount of crestline sinuosity, scour pits would develop that would erode underlying laminations, creating truncations of laminations preserved in the Stimson. No such bounding surfaces have been identified within Stimson cross-sets, which would create marked variations in lamination thicknesses, both between laminations and along their length. Two-dimensional large ripples on the Namib dune show a degree of sinuosity, which is likely to be sufficient to generate scour pits and truncate laminations as the bedform migrated across the lee slope; however, observation of laminations generated by these bedforms for comparison was not possible.

Migration of wind ripples across the lee-slopes of Stimson dunes to produce the uniform thickness repetitive laminations suggests a complicated local wind regime caused by turbulent airflow around the dune, or field wide variations in the wind-field, possibly caused by diurnal variations in wind direction.

The absence of well-defined grainflow strata in cross-bed sets of the Stimson may suggest that the rate of lee face reworking or accretion by wind ripples was much higher than the rate of lee face accretion by grain avalanching. Grain avalanching may have been the main mechanism for building up sediment on the lee slope in the dune migration process, however evidence of this process has simply been eradicated from the stratigraphic record by reworking of the lee slope. The pervasive reworking of avalanche deposits (if they ever formed on Stimson dune lee faces) by impact and/or large 2D ripples might suggest that rates of dune migration by lee face accretion from avalanching were relatively low compared to reworking by winds blowing oblique to the lee face. This difference between bedform migration

speeds and ensuing rates of reworking is due to the size differences between the dunes and the large ripples plus the short wavelength between large ripple crests. Smaller bedforms typically migrate at a much higher rate than larger bedforms which, combined with the close spacing of ripples, ensures complete reworking of the dune lee slope in a relatively short period of time, removing evidence of avalanches.

Preservation of large ripple stratification

The presence of large ripples in the present-day Bagnold dune field raises the question of whether or not they are expressed within the stratigraphic record. In the Bagnold dune field, three-dimensional crested large-ripples are seen migrating up the stoss slopes of many of the large dunes and across secondary lee slopes; however they were not observed migrating down the primary slip-faces (*sensu* Brookfield, 1977) parallel to the dominant wind direction (Ewing *et al.*, 2017). There is little chance of preserving evidence of large ripples on the stoss slope, because this is typically scoured during dune advance, however large ripples may be preserved at the base of a primary or secondary lee slope. If they occurred within the Stimson, large ripples migrating down a primary lee slope would be expressed as superposition (second-order) surfaces, which are not evident at outcrops such as Williams, Bridger Basin or East Glacier. At Mount Shields and Apikuni Mountain, trough cross-sets 0.05 to 0.1 m thick were observed throughout the stratigraphy. Large ripples in the Bagnold dune field have measured heights between 0.12 m and 0.28 m (Ewing *et al.*, 2017), which could potentially generate cross-sets of a similar thickness. It is feasible that the outcrop at Mount Shields and Apikuni Mountain could represent the preserved expression of large ripples migrating across a slope oblique to the dominant wind direction, for example, a secondary lee slope (for example, Namib dune), a spur on a transverse dune or barchan dune, or along longitudinal bedforms (Ewing *et al.*, 2017). Alternatively, these cross-sets may represent smaller superimposed dunes, migrating over a compound dune, rather than large ripples.

Environmental conditions recorded by the Stimson formation

In aeolian environments on Earth, the presence or absence of water can play an important role in the accumulation of aeolian strata and generation

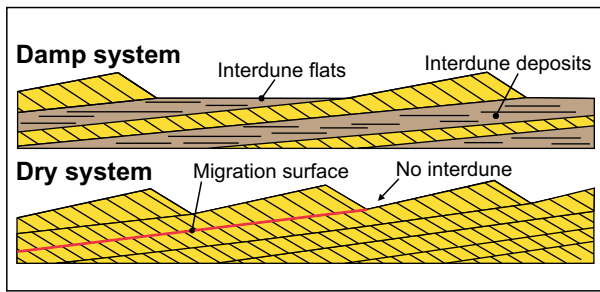


Fig. 23. Schematic diagram depicting key differences between aeolian strata which accumulate under damp or dry conditions. Damp systems are characterized by bipartite stratigraphy consisting of fine-grained interdune deposits and sandy dune facies. Dry systems are characterized exclusively by sandy facies (after Kocurek & Havholm, 1994).

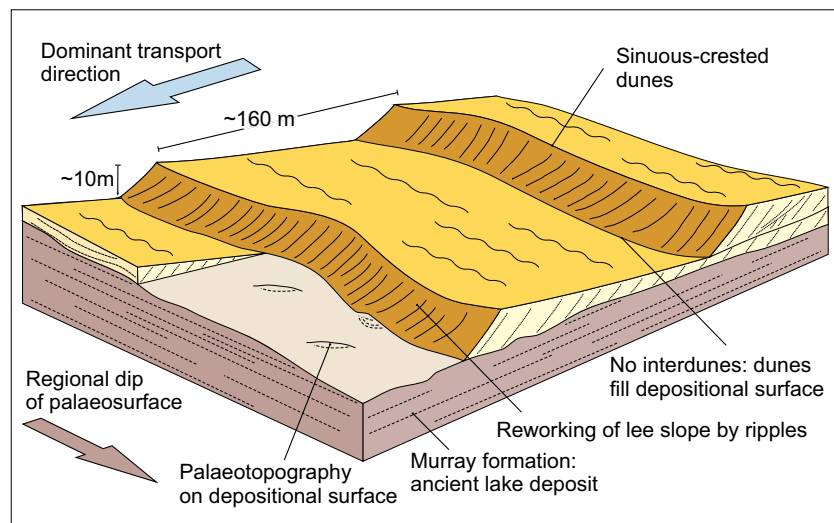
of stratigraphic architecture (Fig. 23) (Kocurek, 1991; Kocurek & Havholm, 1994; Mountney, 2012). In dry systems, where water is absent or the water table is well below the depositional surface, sediment must accumulate aerodynamically, with a spatial decrease in sediment transport from a sediment saturated wind, such that sediment influx into the system is greater than sediment outflux. In this case, sediment can only accumulate when there is sufficient sediment supply to allow dunes to grow and occupy the whole depositional surface. In this situation, laterally extensive interdune flat areas would not develop (Wilson, 1971). Once dunes occupy the entire depositional surface, migrating dunes begin climbing over the stoss side of the down wind dune resulting in sediment accumulation (Rubin & Hunter, 1982). As this occurs, continuous dune

migration surfaces are formed. The absence of moisture to act as an adhesive inhibits accumulation of fine-grained material in these systems.

In damp or wet aeolian systems, where groundwater or the capillary fringe intersects the depositional surface (*sensu* Crabaugh & Kocurek, 1993; Kocurek & Havholm, 1994), moisture can act as a binding agent allowing accumulation of aeolian strata from sediment undersaturated wind, and can trap otherwise wind-winnowed sediments on interdune surfaces (Fig. 24). Here sediment accumulation is controlled hydrodynamically by the relative position of the water table or the capillary fringe to the depositional surface (Kocurek, 1981b; Crabaugh & Kocurek, 1993; Mountney, 2006). Critically, this allows accumulation of sediment from a sediment-undersaturated wind and for accumulation of fine-grained sediment on the interdune by adhesion of particles to the substrate. This results in the accumulation of a distinct bipartite stratigraphy (e.g. Crabaugh & Kocurek, 1993; Mountney & Thompson, 2002) characterized by sandy dune elements separated by horizontally laminated interdune deposits.

Determining how wet or dry the conditions were in which Martian aeolian strata accumulated is important to characterizing palaeoclimate contexts for Martian deposits. There is no evidence of features associated with a water-table control on strata accumulation and preservation in the Stimson; these would include fine-grained interdune deposits, microtopography caused by scouring of damp sediment (Cooper, 1958; Sharp, 1966; Kocurek, 1981b), adhesion structures (Kocurek & Fielder, 1982), wavy laminations, or deformation of damp sediment by migrating dunes (Mountney & Thompson, 2002;

Fig. 24. Reconstruction of dune-scale bedforms which are inferred from preserved stratigraphy. Dunes are interpreted to be sinuous crested crescentic bedforms, ca 10 m high with wavelengths of ca 160 m. Dunes migrated towards the north-east, obliquely across a north-west dipping palaeosurface represented by the unconformity between the Murray and the Stimson formations.



Mountney, 2006). Instead, a succession composed predominantly of sand grade particles (as wind-winning is interpreted to have removed dust-size particles), with repeated cross-bed sets separated by relatively continuous (up to 40 m in length) sub-horizontal and sub-parallel dune migration surfaces is observed. No fine-grained interdune deposits were observed, due to an interpreted lack of a trapping mechanism for finer particles.

This leads to the interpretation that the depositional environment of the Stimson was a dry aeolian system where sediment accumulated aerodynamically and that water played no significant part in the accumulation of sediment. This suggests that the Stimson depositional environment at this location within Gale crater was devoid of water at or near the surface.

Morphology and dimensions of the Stimson dunes and dune field

By understanding the processes and mechanisms responsible for the accumulation and preservation of the Stimson formation, the stratigraphic architecture can be used to reconstruct the morphology of the Stimson dune field, and make estimates of the size, morphology and spacing of palaeo-dunes within the field. The preserved set thickness and their internal facies assemblages can be used to estimate the dune height, dune morphology and processes occurring on the dune at time of deposition. Across the traverse, typical cross-set thicknesses range between 0.4 m and 0.8 m. These are interpreted to represent the migration of medium-scale bedforms. The height of these bedforms (H) can be estimated using the dune height equation defined by Rubin & Hunter (1982, eq. 17):

$$H \simeq \left(\frac{TD}{I} \right)^{\frac{1}{2}}$$

where H is bedform height; T is cross-set thickness; D is downwind extent of dune field and I is bedform index (the average ratio of dune height and wavelength (Wilson, 1972).

Measured set thickness (T) typically ranges between 0.4 m and 0.8 m, with smaller cross-sets potentially representing preserved large ripples (Lapotre *et al.*, 2016; Ewing *et al.*, 2017). The downwind extent of the dune field (D) is not directly quantifiable; however the preserved extent of the Stimson along the transport axis (towards the

north-east) gives a minimum dune-field extent of *ca* 2500 m. A bedform index (I) of 15 was applied. This gives an estimated minimum dune height (H) of *ca* 8 to 12 m for the primary dunes within the Stimson dune field. For comparison, the height of the Namib dune in the Bagnold dune field is *ca* 5 m. A caveat for this estimation is that cross-sets are assumed to represent the migration of transverse main dunes, rather than smaller bedforms migrating across a larger dune, or migration of longitudinal dunes. Additional caveats are that the lateral extent of the preserved Stimson formation outcrop has been heavily denuded, and potentially under-represents the downwind extent of the original Stimson dune field, and that dune size varies depending on location within the dune field. As a result, it is uncertain whether the palaeo-dunes reconstructed from stratigraphy on the traverse represent dunes in the core or fringe of the palaeo-dune field. Using a higher downwind-extent (D) can bracket the maximum probable height of dunes in the Stimson dune field. A value of 20 km was used, which corresponds to the longest continuous section of the Bagnold dune field and approximates to the predicted maximum extent of the Stimson dune field (see later section for calculation). Using this higher down wind extent, dunes with a height of *ca* 33 m are predicted, which may be limited in extent to the centre of the dune field.

Crestline geometry and dune migration style can be inferred from bedform cross-bed geometry. In cases where cross-sets were observed parallel to the axis of sediment transport, trough cross-bedding was common. These preserved cross-set geometries are characteristic of migrating transverse dunes with out of phase sinuous crestlines (Rubin & Carter, 2006). An impression of dune spacing for the Stimson dune field can be gained from observations of dune fields on Earth formed by transverse dunes. Dune fields along the Skeleton Coast of Namibia, which consist of simple transverse and barchanoid dunes, show a strong correlation between dune spacing (λ) and dune height (H) (Lancaster, 1982, fig. 5):

$$\lambda = 53.41 + 9.88 \times H (R^2 = 0.90)$$

Applying the relations observed on the Skeleton coast to the Stimson dune field gives dune spacings which range between 145 m and 180 m for dunes that are predicted to be 8 to 12 m high. These observations and inferred relationships are used to construct a local-scale depositional model, which shows the relation between the bedforms predicted to have existed in the

Stimson dune field and the sedimentary architecture (Fig. 24).

Relationship of the Stimson to the sub-Stimson unconformity

The sub-Stimson unconformity is interpreted to be a deflation surface where wind scour removed a significant thickness of strata of the Mount Sharp group from the moat surrounding Aeolis Mons (Watkins *et al.*, 2016). The Murray formation, upon which the Stimson accumulated, consists largely of mudstone (Grotzinger *et al.*, 2015), so the erosional products of this would probably be lost from Gale crater as dust in suspension; however sand derived from erosion of fluvial intervals within the Murray formation could potentially have been reworked into the Stimson. At a local scale, the Stimson infills palaeotopographic lows and onlaps onto palaeotopographic highs with several tens of centimetres of palaeo-relief (Watkins *et al.*, 2016). Deviation in foreset azimuths of cross-bed sets sometimes by several tens of degrees, from the dominant transport direction towards the north-east is interpreted to be the result of bed-form interaction with palaeotopography. Once the topography was buried as the dune field became established, dip-azimuth orientations

increasingly reflect that of the dominant transport direction, as the influence of the palaeotopography diminished.

At a gross-scale, it is difficult to determine the exact stratigraphic relationships between the Murray and the Stimson. Establishing these relationships is difficult, in part because of a lack of intra-Stimson marker horizons. The predominant north-eastward dune migration direction exhibited by the Stimson palaeo-dunes, a direction that is oblique to the dip of the unconformity on which it accumulated, provides additional evidence of the aeolian origin of the Stimson. By contrast, fluvial systems are sensitive to changes in gradient and drainage networks align with the dip of the slope (Leeder & Gawthorpe, 1987). No evidence for reorientation of dune migration direction to that of the direction of surface slope has been observed in any of the preserved Stimson succession, further indicating that a fluvial origin is implausible.

Extent of the Stimson depositional system

Although the present outcrops of the Stimson formation are erosional remnants, their extent gives a sense of the spatial distribution and scale of the dune field responsible for the deposition of Stimson strata. Geological mapping using orbital

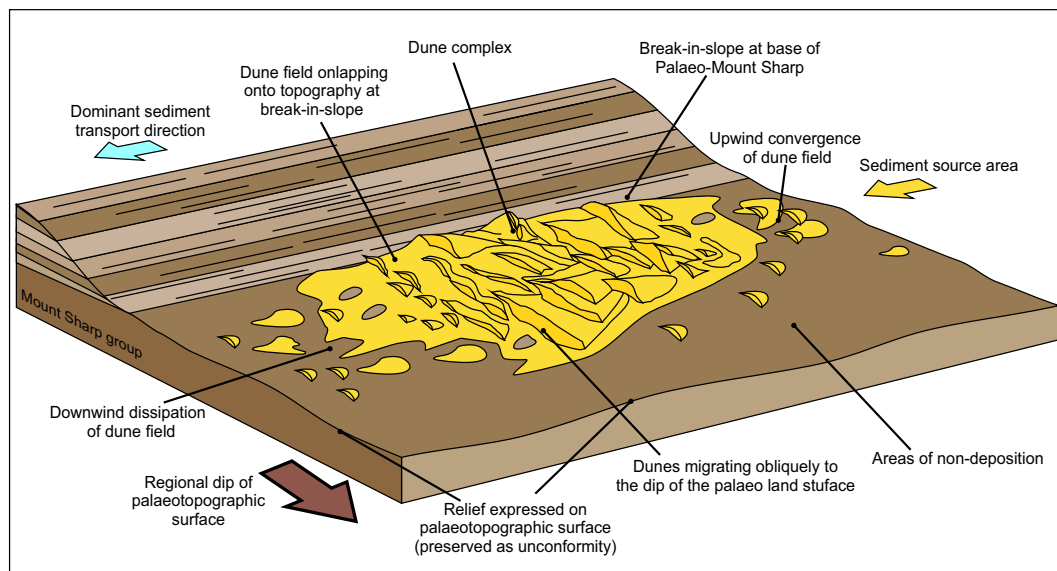


Fig. 25. Regional-scale depositional model for the Stimson formation depicting the relationship of the dune field and the lower slope of Aeolis Mons. The Stimson dune field is interpreted to be geographically limited in size to a few tens of km², and is banked up on the flank of Aeolis Mons. In the dune centre, larger more complex dunes are interpreted to have been present, with simple dunes occupying the fringes of the dune field.

images of the study area indicates that the Stimson [originally referred to as the Washboard unit (Rubin *et al.*, 2014)] is largely confined to an area at the base of Aeolis Mons between the -4460 m and -4290 m contours, with outcrops occurring in a narrow north-east trending strip. The limited spatial distribution over which the Stimson is preserved can be explained in two ways. The first is a preservation bias, where the Stimson was originally deposited over a much wider area (potentially across Aeolis Palus), and has since been eroded to the present restricted elevation range at the base of Aeolis Mons. The second explanation is a depositional bias, where the prevailing wind regime favoured construction of the Stimson dune field along the break in slope at the foot of Aeolis Mons, similar to that of the modern Bagnold dune field, resulting in the restricted distribution Stimson strata (Fig. 25).

The distribution and alignment of the outcrops favours the second explanation; no outlying outcrops have thus far been identified above or below the narrow elevation range using rover or orbiter observation, and the outcrops trend along the axis of sediment transport which would have accumulated as the dune field migrated downwind. Estimates can be made of the size of the active dune field at the time of deposition from the dune spacing (λ), which follow a power-law relationship determined from Earth-based dune fields (Ewing & Kocurek, 2010):

$$\text{Area (km}^2\text{)} = 0.0073 \times \lambda^{16699}, (R^2 = 0.80)$$

Dune spacing of 145 to 180 m predicted for the Stimson would translate to an active dune field of *ca* 30 to 45 km² in size. As a comparison, White Sands dune field occupies an area of *ca* 400 km² (Ewing & Kocurek, 2010), Coral Pink sand dunes occupies 14 km² (Ford *et al.*, 2010) and the Bagnold dune field has sand coverage of 18 km² across a discontinuous area of *ca* 50 km². Although this estimate obviously has significant uncertainty, and probably represents the lower bound on the dune field size: it suggests that the active Stimson dune field may have covered a relatively small area, or at least only a small area of the dune field was preserved (*sensu* Kocurek & Day, 2017), further supporting a depositional bias to the distribution of the Stimson strata. Of course, it is plausible that the aeolian facies that comprise the Stimson in the study area may have passed laterally into other, non-dune field facies to the north in Aeolis Palus if coeval sedimentation had extended there.

Cementation and preservation of the Stimson

At present, the mechanisms responsible for the cementation and preservation of the Stimson formation are not fully understood. Despite sediment accumulating by aerodynamic mechanisms, groundwater would have been required to cement the Stimson. This groundwater could have been present at time of deposition without affecting the aerodynamic mechanism of sediment accumulation, providing that the water table or capillary fringe did not interact with the depositional surface. The origin of this groundwater is also uncertain, but could have originated from fractures in an already cemented Murray formation, or groundwater movement across the top of impermeable units (such as phyllosilicate units) within the Murray formation (*sensu* Fraeman *et al.*, 2016). Groundwater migrating along the upper surfaces of impermeable units would percolate into the Stimson at restricted elevation ranges and could be another reason why the Stimson is only preserved across a narrow elevation range in Gale crater, providing that the elevation of the preserved Stimson formation coincides with a spring line originating at this interface. Several different cements have been proposed, including calcium sulphate (Newsom *et al.*, 2017), and a mixture of iron, calcium, magnesium and silicon oxides (Siebach *et al.*, 2017). Siebach *et al.*, 2017 notes that the Stimson must have been well-cemented prior to the formation of the fracture halos, because the diagenetic fluids associated with these fractures are limited to a narrow annulus around the fracture. This suggests that the invading fluid was only able to penetrate a short distance into an already well-cemented Stimson sandstone.

Sequence stratigraphy of the Stimson formation

A question of interest is whether the cross-bedded sandstones separated by dune migration surfaces observed in the Stimson are the result of accumulation of a single aeolian dune field over time or the summed accumulation of several dune fields separated by episodes of sediment bypass or deflation. In ancient aeolian systems on Earth, the presence of supersurfaces – major sub-regional surfaces indicative of episodes of aeolian deflation – has been used to delineate temporally distinct episodes of aeolian accumulation (Kocurek, 1988; Havholm & Kocurek, 1994; Kocurek & Havholm, 1994;

Mountney, 2012). Identification of such surfaces in the deposits of dry aeolian systems is not easy (Scherer, 2000), especially in the context of Mars rover exploration where it is not possible to 'walk out' all available outcrop sections. However, the absence of distinct sub-horizontal surfaces that cross-cut both cross-bedded units and dune bounding surfaces, and which can be traced laterally or observed at outcrops over a broad area across the rover traverse suggests that supersurfaces are not present. This indicates that the Stimson deposits represent a single period of aeolian accumulation. The consistency of the dune migration direction indicated by cross-bed orientations throughout the succession provides some support for this interpretation.

Significance of the Stimson formation for reconstructing the geological and palaeoclimate evolution of Gale crater

The Stimson sandstone provides important constraints on the landscape and palaeoclimate evolution of Gale crater. Below, the authors present a provisional discussion, although it should be noted that this paper only presents data from between the Logan Pass and East Glacier outcrops; outcrops of the Stimson further along the rover traverse from the Naukluft Plateau to the Murray Buttes are not described here.

The sub-Stimson unconformity juxtaposes aeolian sandstones above lacustrine mudstones. Analysis of this surface indicates that this is not a facies transition. Below the contact, there is no evidence of a transition from deeper water lake deposits to shallower water facies, nor any evidence (as yet provided by surface or orbital observations) of sub-aerial exposure within the mudstone facies. Along the transect, Murray-like mudstones have not been observed to be interstratified within Stimson-like sandstone facies; Murray mudstones always underlie Stimson sandstones, clearly indicating the absence of evidence for facies transition between the mudstones and the cross-stratified sandstones. Moreover, the observation that the Stimson–Murray contact rises in elevation traced southward towards Aeolis Mons with basal Stimson rocks occurring at progressively higher elevations and overlying younger Murray formation strata provides strong evidence that the sub-Stimson contact is indeed a major time gap that encompasses burial, lithification, fracture formation and subsequent exhumation of Murray strata prior to

Stimson deposition (Watkins *et al.*, 2016). The absence of evidence for palaeovalleys or palaeogullies incised into the unconformity surface suggests that erosion of the unconformity was a dry process by aeolian erosion. Moreover, the absence of any visual or geochemical evidence for a palaeosol at the unconformity surface suggests that the deposition of the Stimson sandstone occurred relatively shortly after final erosion of the surface (Newsom *et al.*, 2016).

This abrupt stratigraphic boundary thus records an apparent change from environmental conditions on Mars capable of supporting a standing body of water to one characterized by deposition in a dry aeolian dune system. However, because the boundary between the two formations is an unconformity, it does not record a direct temporal change. Large-scale stratigraphic relationships suggest that the Stimson was laid down after deposition, lithification and erosion of Mount Sharp group rocks (to which the Murray formation belongs). Thus the unconformity probably represents a significant time gap. The contact thus does not record a *transition* from a 'wet' Mars to a 'dry' Mars *sensu stricto*. Rather the stratigraphic and sedimentary relationships indicate that at the geographic locality traversed by the rover, the palaeoenvironment during Murray formation times was characterized by deposition of fine-grained sediments within a lake under humid conditions able to sustain a standing body of water within the crater (Grotzinger *et al.*, 2015) representing a relatively 'warm and wet' palaeoclimate. Later after some unknown amount of time and exhumation of Mount Sharp group rocks, the surface at this locality in Gale crater became characterized by dry, arid conditions where water was all but absent from the depositional surface, or near surface.

It is noted however that the fact that the Stimson is well-lithified and cross-cut by fractures indicative of post-lithification fluid flow (Frydenvang *et al.*, 2017; Yen *et al.*, 2017), and that the dry surface conditions indicated by Stimson deposition do not preclude later groundwater flow through Stimson strata.

A topic of some debate to which analysis of the Stimson can contribute is how the sedimentary mound in Gale crater, Aeolis Mons, came to be formed. It is widely considered that the mound morphology has resulted from wind erosion of a previously filled crater (Bennett & Bell 2016; Day *et al.*, 2016). Evidence for a deflationary surface at the sub-Stimson unconformity provides ground-based support for a wind-erosion

mechanism for mound formation. Moreover, given that the Stimson crops out on the lower slopes of Aeolis Mons, the observations suggest that erosion of the north-west slope of the mound had occurred prior to Stimson deposition. Although the timing of Stimson deposition is not constrained, the fact that the unit is lithified and fractured indicates that Stimson deposition, and as a result mound erosion, is unlikely to be a recent phenomenon. Recent studies have explored the physical processes potentially contributing to mound formation (Day *et al.*, 2016; Anderson & Day, 2017; Steele *et al.*, 2018).

Although beyond the scope of this study, the results provide useful constraints to future studies exploring crater mound formation. One key point relates to the preserved palaeo-transport direction in the Stimson dune field compared with the present-day Bagnold dune field. The Bagnold dune field shows overall migration to the south-west (Anderson & Bell, 2010; Hobbs *et al.*, 2010; Silvestro *et al.*, 2013; Bridges *et al.*, 2017; Ewing *et al.*, 2017), whereas the Stimson records a north-eastward transport direction. This indicates a reversal in the dominant transport direction of the wind responsible for dune field migration at the location of deposition of the Stimson formation within Gale crater. An explanation for this reversal is not discussed here but such changes in dominant transport direction need to be considered in models exploring patterns of erosion of the crater mound in Gale.

CONCLUSIONS

Exploration of the lower northern flank of Aeolis Mons by the Mars Science Laboratory *Curiosity* rover has led to the discovery of a distinctive sandstone stratal unit that has been named the Stimson formation. The Stimson represents the preserved remnants of a dry aeolian dune system which accumulated on an undulating deflationary unconformity. From textural and grain-size analysis, it is concluded that the sand grains composing the Stimson formation were transported by aeolian processes. Grains observed by the Mars Hand Lens Imager (MAHLI) show high roundness and sphericity, which are characteristic of aeolian processes and are difficult to achieve by fluvial transport, even over significant distances. In addition, the succession is devoid of silt-size and mud-size particles which are easily wind-winnowed in aeolian environments.

The Stimson consists almost entirely of cross-bedded sandstone. These cross-beds are composed of uniform thickness cross-laminations interpreted as wind-ripple strata. No clearly distinguishable grainflow beds have yet been identified along this section of the traverse, either due to absence or because they cannot be resolved in Mastcam mosaics. Cross-sets bounded by dune migration surfaces are the dominant architectural feature within the Stimson. These surfaces show a few tens of centimetres of relief over a few metres distance; no erosional features characteristic of scour by fluvial channels have been identified. Sedimentary features characteristic of damp or wet aeolian sediment accumulation, such as fine-grained interdune deposits microtopography, adhesion structures and soft-sediment deformation, are notable for their absence. Sediment within the Stimson accumulated purely by aerodynamic mechanisms in a dry aeolian system. The Stimson formation accumulated on a palaeotopographic surface which formed by deflation of lacustrine mudstones of the Murray formation and undulates at a local scale, while dipping towards the north regionally. The base of the Stimson formation rises in elevation traced southward up the flank of Aeolis Mons. Analysis of cross-strata indicates that the general dune migration direction, and hence net sediment transport, was towards the north-east, which is oblique to the dip of the unconformity surface.

From the assembled stratigraphy and by using modern and ancient terrestrial analogues, and modern Martian analogues, the dunes responsible for depositing the Stimson dune field were reconstructed and the size of the dune field was estimated. The dune field was composed largely of simple sinuous crescentic dunes with a height of 8 to 12 m, and wavelengths of 140 to 185 m (based on terrestrial analogues), although the presence of complex dunes is inferred in some locations. Interdune areas were largely absent, because they were eliminated during phases of dune growth before sediment accumulation occurred. The size of the dune field is estimated to have covered an area *ca* 30 to 45 km², an area comparable to the modern Bagnold dune field, although this is likely to be a lower bound.

The juxtaposition of the dry aeolian system represented by the Stimson formation unconformably above the lacustrine Murray formation represents dramatically contrasting environmental and palaeoclimatic conditions. Although stratigraphic relations are not completely

resolved, it seems likely that the Stimson was not deposited until after Murray formation mudstones, and stratigraphically higher Mount Sharp group rocks had been buried, lithified and subsequently eroded probably by aeolian erosion (Day *et al.*, 2016). Thus, the Stimson is likely to be much younger than the Murray formation. Sedimentological evidence suggests that deposition of the Stimson occurred in a dry arid environment devoid of water at or near the surface.

ACKNOWLEDGEMENTS

The authors wish to acknowledge the enormous efforts made by the NASA MSL Mission project's engineering, science and management teams in making this work possible. They are also grateful to the many MSL team members who participated in tactical and strategic operations during the Stimson campaign. Special thanks go to the Malin Space Science Systems operations team for their hard work in acquiring the extensive image data that made this research possible. Sanjeev Gupta, Steven Banham and Robert Barnes acknowledge funding from the UK Space Agency (UKSA) (Grants: ST/J005169/1, ST/P002064/1 and ST/N000579/1). Data presented in this paper are archived in the Planetary Data System (pds.nasa.gov). Joanneum Research are thanked for use of PROViP software for processing of 3D Mastcam data, and to VRVis for use of the PRO3D visualization software tool for analysis of the 3D Mastcam data. Finally, the authors wish to thank Gary Kocurek and Juan Pedro Rodriguez-Lopez for their constructive reviews.

REFERENCES

Ahlbrandt, T.S. (1979) Textural parameters of eolian deposits. In: *A Study of Global Sand Seas. United States Geological Survey Professional Paper 1052* (Ed. E.D. McKee), pp. 21–51, US Government Printing Office, Washington, DC.

Alexander, D.A., Deen, R.G., Andres, P.M., Zamani, P., Mortensen, H.B., Chen, A.C., Cayanan, M.K., Hall, J.R., Klochko, V.S., Pariser, O., Stanley, C.L., Thompson, C.K. and Yagi, G.M. (2006) Processing of Mars Exploration Rover imagery for science and operations planning. *J. Geophys. Res. Planets*, **111**, E02S02.

Anderson, R.B. and Bell, J.F., III (2010) Geologic mapping and characterization of Gale crater and implications for its potential as a Mars Science Laboratory landing site. *Mars J.*, **5**, 76–128.

Anderson, W. and Day, M. (2017) Turbulent flow over craters on Mars: Vorticity dynamics reveal aeolian excavation mechanism. *Phys. Rev. E*, **96**, 043110.

Anderson, R., Bridges, J.C., Williams, A., Edgar, L., Ollila, A., Williams, J., Nachon, M., Mangold, N., Fisk, M., Schieber, J., Gupta, S., Dromart, G., Wiens, R., Le Mouelic, S., Forni, O., Lanza, N., Mezzacappa, A., Sautter, V., Blaney, D., Clark, B., Clegg, S., Gasnault, O., Lasue, J., Leveille, R., Lewin, E., Lewis, K.W., Maurice, S., Newsom, H., Schwenzer, S.P. and Vaniman, D. (2015) ChemCam results from the Shaler outcrop in Gale crater, Mars. *Icarus*, **249**, 2–21.

Arribas, M.E., Rodríguez-López, J.P., Meléndez, N., Soria, A.R. and de Boer, P.L. (2012) Giant calcite concretions in aeolian dune sandstones; sedimentological and architectural controls on diagenetic heterogeneity, mid-Cretaceous Iberian Desert System, Spain. *Sed. Geol.*, **243–244**, 130–147.

Bagnold, R.A. (1941) *The Physics of Wind Blown Sand and Desert Dunes*, p. 265. Methuen, London.

Barnes, R., Gupta, S., Giordano, M., Morley, J.G., Muller, J.P., Tao, Y., Sprinks, J., Traxler, C., Hesina, G., Ortner, T., Sander, K., Nauschnegg, B., Paar, G., Willner, K. and Pajdla, T. (2015) Geological interpretation and analysis of surface based, spatially referenced planetary image data using PROGIS 2.0 and Pro3D. European Planetary Science Congress 2015, held 27 September - 2 October, 2015 in Nantes, France, Online at <http://meetingorganizer.copernicus.org/EPSC2015/EPSC2015>, id.EPSC2015-375.

Bell, J.F., III, Godber, A., McNair, S., Caplinger, M.A., Maki, J.N., Lemmon, M.T., Van Beek, J., Malin, M.C., Wellington, D., Kinch, K.M., Madsen, M.B., Hardgrove, C., Ravine, M.A., Jensen, E.H., Harker, D., Anderson, R.B., Herkenhoff, K.E., Morris, R.V., Cisneros, E. and Deen, R.G. (2017) The Mars Science Laboratory Curiosity Rover Mast Camera (Mastcam) Instruments: Pre-Flight and In-Flight Calibration, Validation, and Data Archiving. *Earth and Space Sci.*, **4**, 396–452.

Bennett, K. A. and Bell, J. F., III (2016) A global survey of Martian central mounds: Central mounds as remnants of previously more extensive large-scale sedimentary deposits. *Icarus*, **264**, 331–341.

Berner, R.A. (1968) Rate of concretion growth. *Geochim. Cosmochim. Acta*, **32**, 477–483.

Blott, S.J. and Pye, K. (2001) GRADISTAT: a grain size distribution and statistics package for the analysis of unconsolidated sediments. *Earth Surf. Proc. Land.*, **26**, 1237–1248.

Bourke, M.C., Edgett, K.S. and Cantor, B.A. (2008) Recent aeolian dune change on Mars. *Geomorphology*, **94**, 247–255.

Breed, C.S. and Grow, T. (1979) Morphology and distribution of dunes in sand seas observed by remote sensing. In: *A Study of Global Sand Seas. US Geological Survey Professional Paper 1052* (Ed. E.D. McKee), pp. 253–304, United States Government Printing Office, Washington, DC.

Bridges, N.T., Sullivan, R., Newman, C.E., Navarro, S., Van Beek, J., Ewing, R.C., Ayoub, F., Silvestro, S., Gasnault, O., Le Mouelic, S., Lapotre, M.G.A. and Rapin, W. (2017) Martian Aeolian Activity at the Bagnold Dunes, Gale Crater: the View from the Surface and Orbit. *J. Geophys. Res. Planets*, **122**, 2077–2110.

Brookfield, M.E. (1977) Origin of bounding surfaces in ancient aeolian sandstones. *Sedimentology*, **24**, 303–332.

Brothers, S.C., Kocurek, G., Brothers, T.C. and Buynevich, I.V. (2017) Stratigraphic architecture resulting from dune

- interactions: white Sands Dune Field, New Mexico. *Sedimentology*, **64**, 686–713.
- Calef, F.J., III and Parker, T.** (2016) *MSL Gale Merged Orthophoto Mosaic*. PDS Annex, U.S. Geological Survey, Flagstaff, AZ.
- Calef, F.J.I., Dietrich, W.E., Edgar, L., Farmer, J., Fraeman, A., Grotzinger, J., Palucis, M.C., Parker, T., Rice, M., Rowland, S., Stack, K.M., Sumner, D., Williams, J. and Team, M.S.L.** (2013) Geologic mapping of the Mars science laboratory landing ellipse. In: *Lunar and Planetary Science Conference*, **44**, Houston.
- Clarke, J.D.A. and Stoker, C.R.** (2011) Concretions in exhumed and inverted channels near Hanksville Utah: implications for Mars. *Int. J. Astrobiol.*, **10**, 161–175.
- Collinson, J.D., Mounthey, N.P. and Thompson, D.B.** (2006) *Sedimentary Structures*. Terra Publishing, Harpenden, 292 p.
- Cooper, W.S.** (1958) *Coastal Sand Dunes of Oregon and Washington*. Geological Society of America, Boulder, CO, 162 pp.
- Courrech du Pont, S., Narteau, C. and Gao, X.** (2014) Two modes for dune orientation. *Geology*, **42**, 743–746.
- Crabaugh, M. and Kocurek, G.** (1993) Entrada Sandstone – an example of a wet aeolian system. In: *Dynamics and Environmental Context of Aeolian Sedimentary Systems* (Ed. K. Pye), *Geological Society Special Publication*, **72**, 103–126.
- Day, M. and Kocurek, G.** (2016) Observations of an aeolian landscape: from surface to orbit in Gale Crater. *Icarus*, **280**, 37–71.
- Day, M., Anderson, W., Kocurek, G. and Mohrig, D.** (2016) Carving intracrater layered deposits with wind on Mars. *Geophys. Res. Lett.*, **43**, 2473–2479.
- Eastwood, E.N., Kocurek, G., Mohrig, D. and Swanson, T.** (2012) Methodology for reconstructing wind direction, wind speed and duration of wind events from aeolian cross-strata. *J. Geophys. Res. Earth Surf.*, **117**, F002368.
- Edgar, L.A., Grotzinger, J.P., Hayes, A.G., Rubin, D.M., Squyres, S.W., Bell III, J.F. and Herkenhoff, K.E.** (2012) Stratigraphic architecture of bedrock reference section, Victoria crater, Meridiani Planum, Mars. In: *Sedimentary Geology of Mars* (Eds J.P. Grotzinger and R.E. Milliken), *Society for Sedimentary Geology Special Publication*, **102**, 195–209.
- Edgar, L.A., Gupta, S., Rubin, D.M., Lewis, K.W., Kocurek, G.A., Anderson, R.B., Bell, J.F., III, Dromart, G., Edgett, K.S., Grotzinger, J.P., Hardgrove, C., Kah, L.C., Leveille, R., Malin, M.C., Mangold, N., Milliken, R.E., Minitti, M., Palucis, M., Rice, M., Rowland, S.K., Schieber, J., Stack, K.M., Sumner, D.Y., Wiens, R.C., Williams, R.M.E. and Williams, A.J.** (2017) Shaler: *in situ* analysis of a fluvial sedimentary deposit on Mars. *Sedimentology*, **65**, 96–122.
- Edgett, K.S., Yingst, R.A., Ravine, M.A., Caplinger, M.A., Maki, J.N., Ghaemi, F.T., Schaffner, J., Bell, J.F., Edwards, L.J., Herkenhoff, K.E., Heydari, E., Kah, L.C., Lemmon, M.T., Minitti, M.E., Olson, T.S., Parker, T.J., Rowland, S.K., Schieber, J., Sullivan, R.J., Sumner, D.Y., Thomas, P.C., Jensen, E.H., Simmonds, J.J., Sengstacken, A.J., Willson, R.G. and Goetz, W.** (2012) Curiosity's Mars Hand Lens Imager (MAHLI) Investigation. *Space Sci. Rev.*, **170**, 259–317.
- Edgett, K.S., Caplinger, M.A., Maki, J.N., Ravine, M.A., Ghaemi, F.T., McNair, S., Herkenhoff, K.E., Duston, B.M., Willson, R.G., Yingst, R.A., Kennedy, M.R., Minitti, M.E., Sengstacken, A.J., Supulver, K.D., Lipkaman, L.J., Krezoski, G.M., McBride, M.J., Jones, T.L., Nixon, B.E., Van Beek, J.K., Krysak, D.J. and Kirk, R.L.** (2015) Curiosity's robotic arm-mounted Mars Hand Lens Imager (MAHLI): Characterization and calibration status. 0001, Malin Space Science Systems.
- Ehlmann, B.L., Edgett, K.S., Sutter, B., Achilles, C.N., Litvak, M.L., Lapotre, M.G.A., Sullivan, R., Fraeman, A.A., Arvidson, R.E., Blake, D.F., Bridges, N.T., Conrad, P.G., Cousin, A., Downs, R.T., Gabriel, T.S.J., Gellert, R., Hamilton, V.E., Hardgrove, C., Johnson, J.R., Kuhn, S., Mahaffy, P.R., Maurice, S., McHenry, M., Meslin, P.Y., Ming, D.W., Minitti, M.E., Morookian, J.M., Morris, R.V., O'Connell-Cooper, C.D., Pinet, P.C., Rowland, S.K., Schröder, S., Siebach, K.L., Stein, N.T., Thompson, L.M., Vaniman, D.T., Vasavada, A.R., Wellington, D.F., Wiens, R.C. and Yen, A.S.** (2017) Chemistry, Mineralogy, and Grain Properties at Namib and High Dunes, Bagnold Dune Field, Gale Crater, Mars: a Synthesis of Curiosity Rover Observations. *J. Geophys. Res. Planets*, **122**, 2510–2543. <https://doi.org/10.1002/2017JE005267>
- Ellwood, J.M., Evans, P.D. and Wilson, I.G.** (1975) Small-scale aeolian bedforms. *J. Sed. Petrol.*, **45**, 554–561.
- Ewing, R.C. and Kocurek, G.A.** (2010) Aeolian dune interactions and dune-field pattern formation: white Sands Dune Field, New Mexico. *Sedimentology*, **57**, 1199–1219.
- Ewing, R.C., Lapotre, M.G.A., Lewis, K.W., Day, M., Stein, N., Rubin, D.M., Sullivan, R., Banham, S., Lamb, M.P., Bridges, N.T., Gupta, S. and Fischer, W.W.** (2017) Sedimentary processes of the Bagnold Dunes: implications for the eolian rock record of Mars. *Journal of Geophysical Research -Planets*, **122**, 2544–2573. <https://doi.org/10.1002/2017JE005324>
- Folk, R.L.** (1980) *Petrology of Sedimentary Rocks*. Hemphill Publ. Co., Austin, TX, 185 p.
- Ford, R.L., Gillman, S.L., Wilkins, D.E., Clement, W.P. and Nicoll, K.** (2010) Geology and Geomorphology of Coral Pink Sand Dunes State Park, Utah. *Geol. Utah's Parks and Monuments, Utah Geol. Assoc.*, **28**, 371–398.
- Fraeman, A.A., Ehlmann, B.L., Arvidson, R.E., Edwards, C.S., Grotzinger, J.P., Milliken, R.E., Quinn, D.P. and Rice, M.S.** (2016) The stratigraphy and evolution of lower Mount Sharp from spectral, morphological, and thermophysical orbital data sets. *J. Geophys. Res. Planets*, **121**, 1713–1736.
- Fryberger, S.G. and Schenk, C.J.** (1988) Pin stripe lamination – a distinctive feature of modern and ancient eolian sediments. *Sed. Geol.*, **55**, 1–15.
- Frydenvang, J., Gasda, P.J., Hurowitz, J.A., Grotzinger, J.P., Wiens, R.C., Newsom, H.E., Edgett, K.S., Watkins, J., Bridges, J.C., Maurice, S., Fisk, M.R., Johnson, J.R., Rapin, W., Stein, N.T., Clegg, S.M., Schwenzner, S.P., Bedford, C.C., Edwards, P., Mangold, N., Cousin, A., Anderson, R.B., Payré, V., Vaniman, D., Blake, D.F., Lanza, N.L., Gupta, S., Van Beek, J., Sautter, V., Meslin, P.Y., Rice, M., Milliken, R., Gellert, R., Thompson, L., Clark, B.C., Sumner, D.Y., Fraeman, A.A., Kinch, K.M., Madsen, M.B., Mitrofanov, I.G., Jun, I., Calef, F. and Vasavada, A.R.** (2017) Diagenetic silica enrichment and late-stage groundwater activity in Gale crater, Mars. *Geophys. Res. Lett.*, **44**, 4716–4724.
- Ganti, V., Paola, C. and Fofoula-Georgiou, E.** (2013) Kinematic controls on the geometry of the preserved cross sets. *J. Geophys. Res. Earth Surf.*, **118**, 1296–1307.
- Garzanti, E.** (2017) The Maturity Myth In Sedimentology and Provenance Analysis. *J. Sed. Res.*, **87**, 353–365.

- Garzanti, E., Resentini, A., Ando, S., Vezzoli, G., Pereira, A. and Vermeesch, P. (2015) Physical controls on sand composition and relative durability of detrital minerals during ultra-long distance littoral and aeolian transport (Namibia and southern Angola). *Sedimentology*, **62**, 971–996.
- Grant, J.A., Wilson, S.A., Mangold, N., Calef, F., III and Grotzinger, J.P. (2014) The timing of alluvial activity in Gale crater, Mars. *Geophys. Res. Lett.*, **41**, 1142–1148.
- Greeley, R. and Iversen, R.D. (1985) *Wind as a Geological Process*. Cambridge University Press, New York, NY, 333 p.
- Greeley, R., Arvidson, R.E., Elachi, C., Geringer, M.A., Plaut, J.J., Saunders, R.S., Schubert, G., Stofan, E.R., Thouvenot, E.J.P., Wall, S.D. and Weitz, C.M. (1992) Aeolian features on Venus – preliminary Magellan results. *J. Geophys. Res. Planets*, **97**, 13319–13345.
- Grotzinger, J.P., Arvidson, R.E., Bell, J.F., Calvin, W., Clark, B.C., Fike, D.A., Golombek, M., Greeley, R., Haldemann, A., Herkenhoff, K.E., Jolliff, B.L., Knoll, A.H., Malin, M., McLennan, S.M., Parker, T., Soderblom, L., Sohl-Dickstein, J.N., Squyres, S.W., Tosca, N.J. and Watters, W.A. (2005) Stratigraphy and sedimentology of a dry to wet eolian depositional system, Burns formation, Meridiani Planum, Mars. *Earth Planet. Sci. Lett.*, **240**, 11–72.
- Grotzinger, J.P., Sumner, D.Y., Kah, L.C., Stack, K., Gupta, S., Edgar, L., Rubin, D., Lewis, K., Schieber, J., Mangold, N., Milliken, R., Conrad, P.G., DesMarais, D., Farmer, J., Siebach, K., Calef, F., Hurowitz, J., McLennan, S.M., Ming, D., Vaniman, D., Crisp, J., Vasavada, A., Edgett, K.S., Malin, M., Blake, D., Gellert, R., Mahaffy, P., Wiens, R.C., Maurice, S., Grant, J.A., Wilson, S., Anderson, R.C., Beegle, L., Arvidson, R., Hallet, B., Sletten, R.S., Rice, M., Bell, J., Griffes, J., Ehlmann, B., Anderson, R.B., Bristow, T.F., Dietrich, W.E., Dromart, G., Eigenbrode, J., Fraeman, A., Hardgrove, C., Herkenhoff, K., Jandura, L., Kocurek, G., Lee, S., Leshin, L.A., Leveille, R., Limonadi, D., Maki, J., McCloskey, S., Meyer, M., Minitti, M., Newsom, H., Oehler, D., Okon, A., Palucis, M., Parker, T., Rowland, S., Schmidt, M., Squyres, S., Steele, A., Stolper, E., Summons, R., Treiman, A., Williams, R., Yingst, A. and Team, M.S.L.S. (2014) A Habitable Fluvio-Lacustrine Environment at Yellowknife Bay, Gale Crater, Mars. *Science*, **343**, 1242777.
- Grotzinger, J.P., Gupta, S., Malin, M.C., Rubin, D.M., Schieber, J., Siebach, K., Sumner, D.Y., Stack, K.M., Vasavada, A.R., Arvidson, R.E., Calef, F., Edgar, L., Fischer, W.F., Grant, J.A., Griffes, J., Kah, L.C., Lamb, M.P., Lewis, K.W., Mangold, N., Minitti, M.E., Palucis, M., Rice, M., Williams, R.M.E., Yingst, R.A., Blake, D., Blaney, D., Conrad, P., Crisp, J., Dietrich, W.E., Dromart, G., Edgett, K.S., Ewing, R.C., Gellert, R., Hurowitz, J.A., Kocurek, G., Mahaffy, P., McBride, M.J., McLennan, S.M., Mischna, M., Ming, D., Milliken, R., Newsom, H., Oehler, D., Parker, T.J., Vaniman, D., Wiens, R.C. and Wilson, S.A. (2015) Deposition, exhumation, and paleoclimate of an ancient lake deposit, Gale crater, Mars. *Science*, **350**, 177–191.
- Havholm, K.G. and Kocurek, G. (1994) Factors controlling aeolian sequence stratigraphy – clues from super bounding surface-features in the middle Jurassic Page Sandstone. *Sedimentology*, **41**, 913–934.
- Hayes, A.G., Grotzinger, J.P., Edgar, L.A., Squyres, S.W., Watters, W.A. and Sohl-Dickstein, J. (2011) Reconstruction of eolian bed forms and paleocurrents from cross-bedded strata at Victoria Crater, Meridiani Planum, Mars. *J. Geophys. Res. Planets*, **116**, E003688.
- Hobbs, S.W., Paull, D.J. and Bourke, M.C. (2010) Aeolian processes and dune morphology in Gale Crater. *Icarus*, **210**, 102–115.
- Hunter, R.E. (1977a) Basic types of stratification in small eolian dunes. *Sedimentology*, **24**, 361–387.
- Hunter, R.E. (1977b) Terminology of cross-stratified sedimentary layers and climbing-ripple structures. *J. Sed. Petrol.*, **47**, 697–706.
- Hunter, R.E. and Rubin, D.M. (1983) Interpreting cyclic cross-bedding, with an example from the Navajo Sandstone. In: *Developments in Sedimentology. Eolian Sediments and Processes* (Eds M.E. Brookfield and T.S. Ahlbrandt), **38**, pp. 429–454. Elsevier, Amsterdam.
- Hurowitz, J.A., Grotzinger, J.P., Fischer, W.W., McLennan, S.M., Milliken, R.E., Stein, N., Vasavada, A.R., Blake, D.F., Dehouck, E., Eigenbrode, J.L., Fairén, A.G., Frydenvang, J., Gellert, R., Grant, J.A., Gupta, S., Herkenhoff, K.E., Ming, D.W., Rampe, E.B., Schmidt, M.E., Siebach, K.L., Stack-Morgan, K., Sumner, D.Y. and Wiens, R.C. (2017) Redox stratification of an ancient lake in Gale crater, Mars. *Science*, **356**, eaah6849.
- Jerolmack, D.J., Mohrig, D., Grotzinger, J.P., Fike, D.A. and Watters, W.A. (2006) Spatial grain size sorting in eolian ripples and estimation of wind conditions on planetary surfaces: application to Meridiani Planum, Mars. *J. Geophys. Res. Planets*, **111**, E002544.
- Jia, P., Andreotti, B. and Claudin, P. (2017) Giant ripples on comet 67P/Churyumov-Gerasimenko sculpted by sunset thermal wind. *Proc. Natl Acad. Sci. USA*, **114**, 2509–2514.
- Kocurek, G. (1981a) Erg reconstruction – the Entrada Sandstone (Jurassic) of northern Utah and Colorado. *Palaeogeogr. Palaeoclimatol. Palaeoecol.*, **36**, 125–153.
- Kocurek, G. (1981b) Significance of interdune deposits and bounding surfaces in aeolian dune sands. *Sedimentology*, **28**, 753–780.
- Kocurek, G. (1984) Origin of 1st-order bounding surfaces in aeolian sandstones – reply. *Sedimentology*, **31**, 125–127.
- Kocurek, G. (1988) 1st-order and super bounding surfaces in eolian sequences – bounding surfaces revisited. *Sed. Geol.*, **56**, 193–206.
- Kocurek, G. (1991) Interpretation of ancient eolian sand dunes. *Annu. Rev. Earth Planet. Sci.*, **19**, 43–75.
- Kocurek, G. and Day, M. (2017) What is preserved in the aeolian rock record? A Jurassic Entrada Sandstone case study at the Utah–Arizona border. *Sedimentology*, <https://doi.org/10.1111/sed.12422>
- Kocurek, G. and Dott, R.H. (1981) Distinctions and uses of stratification types in the interpretation of eolian sand. *J. Sed. Petrol.*, **51**, 579–595.
- Kocurek, G. and Ewing, R.C. (2017) Trickle-down and trickle-up boundary conditions in eolian dune-field pattern formation. In: *Autogenic Dynamics and Self-Organization in Sedimentary Systems* (Eds D.A. Budd, E.A. Hajek and S.J. Purkis), *SEPM Society for Sedimentary Geology*, **106**, pp. 5–17.
- Kocurek, G. and Fielder, G. (1982) Adhesion structures. *J. Sed. Petrol.*, **52**, 1229–1241.
- Kocurek, G. and Havholm, K. (1994) Eolian sequence stratigraphy – a conceptual framework. In: *Siliciclastic Sequence Stratigraphy* (Eds P. Weimer and H. Posamentier), *American Association of Petroleum Geologists Memoir*, **58**, pp. 393–409.

- Kocurek, G., Ewing, R.C. and Mohrig, D. (2010) How do bedform patterns arise? New views on the role of bedform interactions within a set of boundary conditions. *Earth Surf. Proc. Land.*, **35**, 51–63.
- Lancaster, N. (1982) Dunes on the Skeleton Coast, Namibia (south west Africa) – geomorphology and grain-size relationships. *Earth Surf. Proc. Land.*, **7**, 575–587.
- Lancaster, N. (1988) The development of large aeolian bedforms. *Sed. Geol.*, **55**, 69–89.
- Langford, R.P. and Chan, M.A. (1993) Downwind changes within an ancient dune sea, Permian Cedar Mesa Sandstone, southeast Utah. In: *Aeolian Sediments: Ancient and Modern* (Eds K. Pye and N. Lancaster), pp. 109–126. Blackwell Publishing Ltd., Oxford, UK.
- Lapotre, M.G.A., Ewing, R.C., Lamb, M.P., Fischer, W.W., Grotzinger, J.P., Rubin, D.M., Lewis, K.W., Ballard, M.J., Day, M., Gupta, S., Banham, S.G., Bridges, N.T., Des Marais, D.J., Fraeman, A.A., Grant, J.A., Herkenhoff, K.E., Ming, D.W., Mischna, M.A., Rice, M.S., Sumner, D.Y., Vasavada, A.R. and Yingst, R.A. (2016) Large wind ripples on Mars: A record of atmospheric evolution. *Science*, **353**, 55–58.
- Lapotre, M.G.A., Lamb, M.P. and McElroy, B. (2017) What sets the size of current ripples? *Geology*, **45**, 243–246.
- Le Deit, L., Hauber, E., Fueten, F., Pondrelli, M., Rossi, A.P. and Jaumann, R. (2013) Sequence of infilling events in Gale Crater, Mars: Results from morphology, stratigraphy, and mineralogy. *J. Geophys. Res. Planets*, **118**, 2439–2473.
- Leclair, S.F. and Bridge, J.S. (2001) Quantitative interpretation of sedimentary structures formed by river dunes. *J. Sed. Res.*, **71**, 713–716.
- Leeder, M.R. and Gawthorpe, R.L. (1987) Sedimentary models for extensional tilt-block/half-graben basins. In: *Continental Extensional Tectonics* (Eds M.P. Coward, J.F. Dewey and P.L. Hancock), *Geological Society, London, Special Publications*, **28**, pp. 139–152.
- Lindholm, R. (1987) *A Practical Approach to Sedimentology*. Allen & Unwin, London, 276 p.
- Maki, J., Thiessen, D., Pourangi, A., Kobzeff, P., Litwin, T., Scherr, L., Elliott, S., Dingizian, A. and Maimone, M. (2012) The Mars Science Laboratory Engineering Cameras. *Space Sci. Rev.*, **170**, 77–93.
- Malin, M.C. and Edgett, K.S. (2000) Sedimentary rocks of early Mars. *Science*, **290**, 1927–1937.
- Malin, M.C., Ravine, M.A., Caplinger, M.A., Ghaemi, F.T., Schaffner, J.A., Maki, J.N., Bell III, J.F., Cameron, J.F., Dietrich, W.E., Edgett, K.S., Edwards, L.J., Garvin, J.B., Hallet, B., Herkenhoff, K.E., Heydari, E., Kah, L.C., Lemmon, M.T., Minitti, M.E., Olson, T.S., Parker, T.J., Rowland, S.K., Schieber, J., R., S., Sullivan, R.J., Sumner, D.Y., Yingst, R.A., Duston, B.M., McNair, S. and E.H., J. (2017) The Mars Science Laboratory (MSL) Mast Cameras and Descent Imager: I. Investigation and instrument descriptions. *Earth and Space Sci.*, **4**, 506–539.
- McEwen, A.S., Eliason, E.M., Bergstrom, J.W., Bridges, N.T., Hansen, C.J., Delamere, W.A., Grant, J.A., Gulick, V.C., Herkenhoff, K.E., Keszthelyi, L., Kirk, R.L., Mellon, M.T., Squyres, S.W., Thomas, N. and Weitz, C.M. (2007) Mars Reconnaissance Orbiter's High Resolution Imaging Science Experiment (HiRISE). *J. Geophys. Res. Planets*, **112**, E002605.
- Metz, J.M., Grotzinger, J.P., Rubin, D.M., Lewis, K.W., Squyres, S.W. and Bell, J.F. (2009) Sulfate-rich eolian and wet interdune deposits, Erebus crater, Meridiani Planum, Mars. *J. Sed. Res.*, **79**, 247–264.
- Milliken, R.E., Ewing, R.C., Fischer, W.W. and Hurowitz, J. (2014) Wind-blown sandstones cemented by sulfate and clay minerals in Gale Crater, Mars. *Geophys. Res. Lett.*, **41**, 1149–1154.
- Mountney, N.P. (2006) Periodic accumulation and destruction of aeolian erg sequences in the Permian Cedar Mesa Sandstone, White Canyon, southern Utah, USA. *Sedimentology*, **53**, 789–823.
- Mountney, N.P. (2012) A stratigraphic model to account for complexity in aeolian dune and interdune successions. *Sedimentology*, **59**, 964–989.
- Mountney, N.P. and Thompson, D.B. (2002) Stratigraphic evolution and preservation of aeolian dune and damp/wet interdune strata: an example from the Triassic Helsby Sandstone Formation, Cheshire Basin, UK. *Sedimentology*, **49**, 805–833.
- Mountney, N., Howell, J., Flint, S. and Jerram, D. (1999) Relating eolian bounding-surface geometries to the bed forms that generated them: Etjo Formation, Cretaceous, Namibia. *Geology*, **27**, 159–162.
- Newsom, H., Belgacem, I., Jackson, R., Ha, B., Vaci, Z., Wiens, R., Frydenvang, J., Gasda, P., Lanza, N. and Clegg, S. (2016) The materials at an unconformity between the Murray and Stimson formations at Marias Pass, Gale crater, Mars. In: *Lunar and Planetary Science Conference*, **47**, pp. 2397.
- Newsom, H., Jackson, R., Wiens, R., Frydenvang, J., Gasada, P., Lanza, N., Ollila, A., Clegg, S., Gasnault, O. and Maurice, S. (2017) Increasing occurrence of sandstone cemented with calcium sulfate on Mount Shart, Gale Crater, Mars. In: *Lunar and Planetary Science Conference*, **48**, pp. 2495, Houston.
- Paar, G. and Consortium, P. (2016) PROViDE Final Report. Available at: http://www.provide-space.eu/wp-content/uploads/2015/01/PRVD-REP-JR-Final-Report_2016-04-14-Public.pdf.
- Paar, G., Huber, B., Gupta, S., Barnes, R., Traxler, C. and Ortner, T. (2017) Planetary Rover Vision Processing and Visualization: PROViP and PRO3D. In: *Proc. Global Space Exploration Conference*, GLEX-17, Beijing, China.
- Palucis, M.C., Dietrich, W.E., Hayes, A.G., Williams, R.M.E., Gupta, S., Mangold, N., Newsom, H., Hardgrove, C., Calef, F., III and Sumner, D.Y. (2014) The origin and evolution of the Peace Vallis fan system that drains to the Curiosity landing area, Gale Crater, Mars. *J. Geophys. Res. Planets*, **119**, 705–728.
- Paola, C. and Borgman, L. (1991) Reconstructing random topography from preserved stratification. *Sedimentology*, **38**, 553–565.
- Pettijohn, F.J. (1957) *Sedimentary Rocks*. Harper, New York, NY, 718 p.
- Porter, M.L. (1987) Sedimentology of an ancient erg margin – the lower Jurassic Aztec Sandstone, southern Nevada and southern California. *Sedimentology*, **34**, 661–680.
- Powers, M.C. (1953) A new roundness scale for sedimentary particles. *J. Sed. Res.*, **23**, 117–119.
- Radebaugh, J. (2013) Dunes on Saturn's moon Titan as revealed by the Cassini Mission. *Aeol. Res.*, **11**, 23–41.
- Rampe, E.B., Ming, D.W., Blake, D.F., Bristow, T.F., Chipera, S.J., Grotzinger, J.P., Morris, R.V., Morrison, S.M., Vaniman, D.T., Yen, A.S., Achilles, C.N., Craig, P.I., Des Marais, D.J., Downs, R.T., Farmer, J.D., Fendrich, K.V., Gellert, R., Hazen, R.M., Kah, L.C., Morookian, J.M., Peretyazhko, T.S., Sarrazin, P., Treiman, A.H., Berger, J.A., Eigenbrode, J., Fairén, A.G., Forni, O., Gupta, S., Hurowitz, J.A., Lanza, N.L., Schmidt, M.E., Siebach, K., Sutter, B. and Thompson, L.M. (2017) Mineralogy of an

- ancient lacustrine mudstone succession from the Murray formation, Gale crater, Mars. *Earth Planet. Sci. Lett.*, **471**, 172–185.
- Rice, M.S., Gupta, S., Treiman, A.H., Stack, K.M., Calef, F., Edgar, L.A., Grotzinger, J., Lanza, N., Le Deit, L., Lasue, J., Siebach, K.L., Vasavada, A., Wiens, R.C. and Williams, J. (2017) Geologic overview of the Mars Science Laboratory rover mission at the Kimberley, Gale crater, Mars. *J. Geophys. Res. Planets*, **122**, 2–20.
- Rodriguez-Lopez, J.P., Melendez, N., de Boer, P.L., Soria, A.R. and Liesa, C.L. (2013) Spatial variability of multi-controlled aeolian supersurfaces in central-erg and marine-erg-margin systems. *Aeol. Res.*, **11**, 141–154.
- Rodríguez-López, J.P., Clemmensen, L.B., Lancaster, N., Mounthey, N.P. and Veiga, G.D. (2014) Archean to Recent aeolian sand systems and their sedimentary record: Current understanding and future prospects. *Sedimentology*, **61**, 1487–1534.
- Romain, H.G. (2014) *Controls on Aeolian Bed-Set Architecture and Implications for Reservoir Heterogeneity*. University of Leeds, Leeds, 338 p.
- Rubin, D.M. (1987) Formation of scalloped cross-bedding without unsteady flows. *J. Sed. Petrol.*, **57**, 39–45.
- Rubin, D.M. and Carter, C.L. (2006) *Cross-Bedding, Bedforms, and Paleocurrents*. SEPM, Tulsa, Oklahoma, 195 p.
- Rubin, D.M. and Hunter, R.E. (1982) Bedform climbing in theory and nature. *Sedimentology*, **29**, 121–138.
- Rubin, D.M. and Hunter, R.E. (1987) Bedform alignment in directionally varying flows. *Science*, **237**, 276–278.
- Rubin, D.M. and Ikeda, H. (1990) Flume experiments on the alignment of transverse, oblique, and longitudinal dunes in directionally varying flows. *Sedimentology*, **37**, 673–684.
- Rubin, D., Edgar, L. and Lewis, K. (2014) Physical Sedimentology in Gale Crater, Mars. In: *Search and Discovery*, #50991. AAPG.
- Sagan, C. and Chyba, C. (1990) Triton's streaks as windblown dust. *Nature*, **346**, 546–548.
- Schenk, C.J., Gautier, D.L., Olhoeft, G.R. and Lucius, J.E. (1993) Internal structure of an aeolian dune using ground-penetrating radar. In: *Aeolian Sediments Ancient and Modern* (Eds K. Pye and N. Lancaster), *Special Publication International Association of Sedimentologists*, **16**, pp. 61–69.
- Scherer, C.M.S. (2000) Eolian dunes of the Botucatu Formation (Cretaceous) in southernmost Brazil: morphology and origin. *Sed. Geol.*, **137**, 63–84.
- Schieber, J., Bish, D., Coleman, M., Reed, M., Hausrath, E.M., Cosgrove, J., Gupta, S., Minitti, M.E., Edgett, K.S. and Malin, M. (2017) Encounters with an unearthy mudstone: Understanding the first mudstone found on Mars. *Sedimentology*, **64**, 311–358.
- Sharp, R.P. (1963) Wind ripples. *J. Geol.*, **71**, 617–636.
- Sharp, R.P. (1966) Kelso Dunes, Mojave Desert, California. *Geol. Soc. Am. Bull.*, **77**, 1045–1074.
- Siebach, K., McLennan, S. and Fedo, C. (2017) Geochemistry of the Stimson Sandstone, Gale Crater, Mars. In: *Lunar and Planetary Science Conference*, **48**, pp. 2499, Houston.
- Silvestro, S., Vaz, D.A., Ewing, R.C., Rossi, A.P., Fenton, L.K., Michaels, T.I., Flahaut, J. and Geissler, P.E. (2013) Pervasive aeolian activity along rover Curiosity's traverse in Gale Crater, Mars. *Geology*, **41**, 483–486.
- Slipiski, M. and Jakosky, B.M. (2016) Argon isotopes as tracers for martian atmospheric loss. *Icarus*, **272**, 212–227.
- Stack, K.M., Edwards, C.S., Grotzinger, J.P., Gupta, S., Sumner, D.Y., Calef, F.J., III, Edgar, L.A., Edgett, K.S., Fraeman, A.A., Jacob, S.R., Le Deit, L., Lewis, K.W., Rice, M.S., Rubin, D., Williams, R.M.E. and Williford, K.H. (2016) Comparing orbiter and rover image-based mapping of an ancient sedimentary environment, Aeolis Palus, Gale crater, Mars. *Icarus*, **280**, 3–21.
- Steele, L.J., Kite, E.S. and Michaels, T.I. (2018) Crater mound formation by wind erosion on Mars. *J. Geophys. Res. Planets*, **123**, 113–130. <https://doi.org/10.1002/2017JE005459>
- Sullivan, R. and Kok, J. (2017) Aeolian saltation on Mars at low wind speeds. *J. Geophys. Res. Planets*, **122**, 2111–2143.
- Summons, R.E., Amend, J.P., Bish, D., Buick, R., Cody, G.D., Des Marais, D.J., Dromart, G., Eigenbrode, J.L., Knoll, A.H. and Sumner, D.Y. (2011) Preservation of Martian Organic and Environmental Records: Final Report of the Mars Biosignature Working Group. *Astrobiology*, **11**, 157–181.
- Swanson, T., Mohrig, D., Kocurek, G., Perillo, M. and Venditti, J. (2018) Bedform spurs: a result of a trailing helical vortex wake. *Sedimentology*, **65**, 191–208.
- Sweet, M.L. and Kocurek, G. (1990) An empirical model of aeolian dune lee-face airflow. *Sedimentology*, **37**, 1023–1038.
- Tanaka, K.L., Skinner, J.A., Dohm, J.M., Irwin III, R.P., Kolb, E.J., Fortezzo, C.M., Platz, T., Michael, G.G. and Hare, T.M. (2014) Geologic map of Mars. 2329-132X, US Geological Survey.
- Telfer, M., Parteli, E. and Radebaugh, J. (2017) Evidence supporting aeolian depositional origin of landforms of Sputnik Planum, Pluto, from New Horizons imagery. In: *Fifth International Planetary Dunes Workshop*. Lunar & Planetary Institute, St George, Utah.
- Thomson, B.J., Bridges, N.T., Milliken, R., Baldrige, A., Hook, S.J., Crowley, J.K., Marion, G.M., de Souza, C.R., Brown, A.J. and Weitz, C.M. (2011) Constraints on the origin and evolution of the layered mound in Gale Crater, Mars using Mars Reconnaissance Orbiter data. *Icarus*, **214**, 413–432.
- Traxler, C., Ortner, T., Hesina, G., Barnes, R., Gupta, S., Paar, G., Muller, J.-P. and Tao, Y. (2018) The PROViDE Framework: Accurate 3D geological models for virtual exploration of the Martian surface from rover and orbital imagery. In: *3D Digital Geological Models: From Terrestrial Outcrops to Planetary Surfaces* (Ed. A. Bistacchi), John Wiley & Sons, Hoboken, NJ.
- Vasavada, A.R., Grotzinger, J.P., Arvidson, R.E., Calef, F.J., Crisp, J.A., Gupta, S., Hurowitz, J., Mangold, N., Maurice, S., Schmidt, M.E., Wiens, R.C., Williams, R.M.E. and Yingst, R.A. (2014) Overview of the Mars Science Laboratory mission: Bradbury Landing to Yellowknife Bay and beyond. *J. Geophys. Res. Planets*, **119**, 1134–1161.
- Warner, N., Silverman, M., Samuels, J., DeFlores, L., Sengstacken, A., Maki, J., Scodary, A., Peters, S., Litwin, T., Metz, B. and IEEE (2016) The Mars Science Laboratory Remote Sensing Mast. In: *2016 IEEE Aerospace Conference, IEEE Aerospace Conference Proceedings*, Big Sky, MT, USA.
- Watkins, J.A., Grotzinger, J., Stein, N., Banham, S.G., Gupta, S., Rubin, D., Stack, K.M. and Edgett, K.S. (2016) Paleotopography of Erosional Unconformity, Base of Stimson Formation, Gale Crater, Mars. In: *Lunar and Planetary Science Conference*, **47**, pp. 2939. LPI, Houston.
- Williams, R.M.E., Grotzinger, J.P., Dietrich, W.E., Gupta, S., Sumner, D.Y., Wiens, R.C., Mangold, N., Malin, M.C., Edgett, K.S., Maurice, S., Forni, O., Gasnault, O., Ollila, A., Newsom, H.E., Dromart, G., Palucis, M.C., Yingst,

- R.A., Anderson, R.B., Herkenhoff, K.E., Le Mouelic, S., Goetz, W., Madsen, M.B., Koefoed, A., Jensen, J.K., Bridges, J.C., Schwenzer, S.P., Lewis, K.W., Stack, K.M., Rubin, D., Kah, L.C., Bell, J.F., Farmer, J.D., Sullivan, R., Van Beek, T., Blaney, D.L., Pariser, O., Deen, R.G. and Team, M.S.L.S. (2013) Martian Fluvial Conglomerates at Gale Crater. *Science*, **340**, 1068–1072.
- Wilson, I.G. (1971) Desert sandflow basins and a model for development of ergs. *Geogr. J.*, **137**, 180–199.
- Wilson, I.G. (1972) Aeolian bedforms – their development and origins. *Sedimentology*, **19**, 173–210.
- Yen, A.S., Ming, D.W., Vaniman, D.T., Gellert, R., Blake, D.F., Morris, R.V., Morrison, S.M., Bristow, T.F., Chipera, S.J., Edgett, K.S., Treiman, A.H., Clark, B.C., Downs, R.T., Farmer, J.D., Grotzinger, J.P., Rampe, E.B., Schmidt, M.E., Sutter, B. and Thompson, L.M. (2017) Multiple stages of aqueous alteration along fractures in mudstone and sandstone strata in Gale Crater, Mars. *Earth Planet. Sci. Lett.*, **471**, 186–198.
- Yingst, R.A., Edgett, K.S., Kennedy, M.R., Krezoski, G.M., McBride, M.J., Minitti, M.E., Ravine, M.A. and Williams, R.M.E. (2016) MAHLI on Mars: lessons learned operating a geoscience camera on a landed payload robotic arm. *Geosci. Instrum. Meth. Data Systems*, **5**, 205–217.
- Yizhaq, H. and Katra, I. (2015) Longevity of aeolian megaripples. *Earth Planet. Sci. Lett.*, **422**, 28–32.

Manuscript received 28 July 2017; revision accepted 19 February 2018

Supporting Information

Additional Supporting Information may be found in the online version of this article:

- Data S0.** Slide pack of figures from this paper
- Data S1.** Images and Mosaics used
- Data S2A.** GIS data provided
- Data S2B.** File containing GIS data
- Data S3.** Digital Outcrop Model (DOM) analytical tool and methods
- Data S4A.** Raw Grain-size measurements
- Data S4B.** Histogram of all grain-size measurements
- Data S4C.** Histogram of individual grain-size measurements
- Data S5.** Lamination thickness measurements
- Data S6.** Stimson formation Mosaic footprints map
- Data S7.** Additional supporting images and URLs
- Data S8.** DOM dip azimuth measurements made
- Data S9.** Map of palaeocurrent measurements